

# GA-NIFS: high prevalence of dusty and metal-enriched outflows in massive and luminous star-forming galaxies at $z \sim 3 - 9$

B. Rodríguez Del Pino<sup>1,\*</sup>, S. Arribas<sup>1</sup>, M. Perna<sup>1</sup>, I. Lamperti<sup>2,3</sup>, A. Bunker<sup>4</sup>, S. Carniani<sup>6</sup>, S. Charlot<sup>7</sup>, F. D'Eugenio<sup>9,10</sup>, R. Maiolino<sup>9,10,11</sup>, H. Übler<sup>8</sup>, E. Bertola<sup>3</sup>, T. Böker<sup>5</sup>, G. Cresci<sup>3</sup>, G. C. Jones<sup>9,10</sup>, C. Marconcini<sup>2,3</sup>, E. Parlanti<sup>6</sup>, J. Scholtz<sup>9,10</sup>, G. Venturi<sup>6</sup>, and S. Zamora<sup>6</sup>

<sup>1</sup> Centro de Astrobiología (CAB), CSIC-INTA, Cra. de Ajalvir Km. 4, 28850 – Torrejón de Ardoz, Madrid, Spain

<sup>2</sup> Università di Firenze, Dipartimento di Fisica e Astronomia, via G. Sansone 1, 50019 Sesto F.no, Firenze, Italy

<sup>3</sup> INAF - Osservatorio Astrofisico di Arcetri, Largo E. Fermi 5, I-50125 Firenze, Italy

<sup>4</sup> Department of Physics, University of Oxford, Denys Wilkinson Building, Keble Road, Oxford OX1 3RH, UK

<sup>5</sup> European Space Agency, c/o STScI, 3700 San Martin Drive, Baltimore, MD 21218, USA

<sup>6</sup> Scuola Normale Superiore, Piazza dei Cavalieri 7, I-56126 Pisa, Italy

<sup>7</sup> Sorbonne Université, CNRS, UMR 7095, Institut d'Astrophysique de Paris, 98 bis bd Arago, 75014 Paris, France

<sup>8</sup> Max-Planck-Institut für extraterrestrische Physik (MPE), Gießenbachstraße 1, 85748 Garching, Germany

<sup>9</sup> Kavli Institute for Cosmology, University of Cambridge, Madingley Road, Cambridge, CB3 0HA, UK

<sup>10</sup> Cavendish Laboratory - Astrophysics Group, University of Cambridge, 19 JJ Thomson Avenue, Cambridge, CB3 0HE, UK

<sup>11</sup> Department of Physics and Astronomy, University College London, Gower Street, London WC1E 6BT, UK

Received ... ; accepted ...

## ABSTRACT

We present the identification and characterization of ionized outflows in 15 star-forming systems at  $z \sim 3 - 9$  with no evidence of Active Galactic Nuclei (AGN), observed with JWST/NIRSpec IFU as part of the GA-NIFS program. The targets often show satellites and complex substructure, from which we isolate 40 galaxies/regions. The sample probes the high-mass end of the galaxy population, with most sources having  $\log_{10}(M_*/M_\odot) = 9.5 - 11$ , extending previous studies on high- $z$  star formation driven outflows that mainly focused on lower-mass galaxies. Using the [OIII]5007 and H $\alpha$  emission lines, we identify broad kinematic components consistent with galactic outflows in 14 galaxies/regions. We find that the outflowing gas is more dust attenuated (by  $A_V \sim 0.59$  mag on average) and metal-enriched (0.13 dex) than the interstellar medium (ISM) of the host galaxies, but its velocities are insufficient to escape the galaxies and reach the circumgalactic medium, suggesting that outflows mainly redistribute dust and metals around their hosts. The outflows identified in this study display velocity dispersions within  $\sigma_{\text{out}} = 130 - 340$  km s $^{-1}$  and outflow velocities  $v_{\text{out}} = 170 - 600$  km s $^{-1}$ , and, when combined with less luminous and less massive star-forming galaxies from previous works, reveal a statistically significant correlation between  $v_{\text{out}}$  and star formation rate (SFR). The typically low mass-loading factors ( $\eta = \dot{M}_{\text{out}}/\text{SFR} \leq 1$ , in 9 out of 14 the outflows) indicate that these outflows do not strongly suppress star formation. Overall, our results suggest that ejective feedback via ionized outflows is inefficient in massive, luminous star-forming galaxies within the first 2 Gyr of the Universe.

**Key words.** star formation – outflows – kinematics and dynamics clusters

## 1. Introduction

Galactic outflows, triggered by intense episodes of star formation or by the accretion of material onto Active Galactic Nuclei (AGN), are widely regarded as fundamental drivers of galaxy evolution across cosmic time. They are believed to regulate and suppress both star formation and black hole growth, and are considered the principal mechanism through which dust and metals are redistributed on galactic scales or even expelled into the intergalactic medium. Due to their importance, the identification and characterization of galactic outflows is one of the most extensively studied topics in galaxy evolution, both in the local Universe and at high redshift (see reviews by [Rupke 2018](#); [Veilleux et al. 2020](#)).

Outflows are observed across multiple gas phases (ionized, neutral, and molecular), all of which should be taken into account to fully characterize their global properties and impact

on host galaxies. Nevertheless, the ionized phase is the most frequently studied, as it can be traced through strong rest-frame optical emission lines such as H $\alpha$  and [O III] $\lambda\lambda 496, 5007$ . Since these lines can be accessed by ground based observatories with spectroscopic capabilities out to  $z \leq 2.5$  (where they are shifted into the near-infrared regime), ionized outflows have been extensively studied in large samples of star forming (SF) galaxies and AGN in the local Universe (e.g., [Cicone et al. 2016](#); [Perna et al. 2017](#)) and across the last  $\sim 11$  Gyrs of cosmic time (e.g., [Newman et al. 2012](#); [Förster Schreiber et al. 2019](#); [Swinbank et al. 2019](#); [Concas et al. 2022](#)). Overall, ionized galactic outflows are frequently (70 – 100%) identified in AGN hosts both at low ([Harrison et al. 2014](#); [Villar Martín et al. 2014](#)) and high ( $z \sim 3$ ) redshifts ([Brusa et al. 2015](#); [Temple et al. 2019](#); [Kakkad et al. 2020](#); [Tozzi et al. 2024](#)). In the local Universe, the incidence in main-sequence star-forming galaxies is very low (e.g., 1%; [Rodríguez Del Pino et al. 2019](#)) but, since their incidence increases with star formation activity,

\* e-mail: brodriguez@cab.inta-csic.es

they become almost ubiquitous in galaxies with the highest star formation rates (SFRs) such as ULIRGs (Ultra Luminous Infrared Galaxies; e.g., Arribas et al. 2014). At Cosmic Noon ( $z = 2 - 3$ ), the detection rate in SF galaxies increases, probably because observations generally target brighter (thus more active and massive) systems (Genzel et al. 2011; Newman et al. 2012; Förster Schreiber et al. 2019; Freeman et al. 2019). In fact, their incidence seems to significantly decrease in low-mass systems ( $\log_{10}(M_*/M_\odot) < 9.6$ ; Concas et al. 2022). In the SF population, i.e. galaxies without evidence of AGN activity, different works have found correlations between the kinematics of the outflowing gas and host galaxy properties such as stellar mass ( $M_*$ ) and star formation rate surface density ( $\Sigma_{\text{SFR}}$ ) at low (e.g., Avery et al. 2021) and high redshift (e.g., Davies et al. 2019; Gupta et al. 2023; Llerena et al. 2023). Although outflows in SF galaxies can reach velocities of several hundred km/s and entrain substantial amounts of ionized gas, their impact on the star formation activity of the hosts appears to be limited across cosmic time. This result is derived from the low ratio between the mass-loss rate and the SFR in the host, also known as the mass-loading factor,  $\eta$ . At least in local galaxies, however, outflows do seem to influence the distribution of metals and dust: they are often found to be more dust-obscured than their hosts (Rodríguez Del Pino et al. 2019) and enriched in metals, potentially contributing to the shaping of the mass–metallicity relation (Chisholm et al. 2018). At higher redshifts, however, this is a result that still needs to be explored.

Despite the extensive studies conducted up to  $z \sim 3$ , identifying and characterizing ionized outflows at earlier epochs has remained out of reach until recently, largely because no facilities offered spectroscopic coverage in the near-infrared regime beyond  $2.5 \mu\text{m}$ , where the  $\text{H}\alpha$  line is redshifted at  $z \geq 3$ . The successful launch and commissioning of the James Webb Space Telescope (JWST) has opened a new era in the exploration of distant galaxies. In fact, several works have already started to characterize ionized outflows in star-forming galaxies at  $3 < z < 9$  (Carniani et al. 2024; Xu et al. 2025; Cooper et al. 2025; Zhang et al. 2024; Zhu et al. 2025). These studies are reporting an incidence of ionized outflows that varies between 20–40% (Carniani et al. 2024; Xu et al. 2025) and 3.4% (Cooper et al. 2025). Such discrepancies are probably due to the different spectral resolution of the observations employed in each work, since higher spectral resolution favors the detection of a broad component, and the application of stricter outflow selection criteria. These studies also find contrasting results on the impact that star formation driven outflows have on the star formation activity in the host galaxy, quantified by the mass-loading factor,  $\eta$ , and the fraction of outflowing gas that can escape the host galaxies. Within similar ranges of stellar masses ( $\log_{10}(M_*/M_\odot) = [7.5, 9.5]$ ) and star formation activity ( $\log_{10}(\text{SFR}) = [-0.2, 2] \text{ M}_\odot \text{yr}^{-1}$ ), while Carniani et al. (2024) estimates median values of  $\eta \sim 2$  and outflow velocities that are on average three times higher than the escape velocity, Cooper et al. (2025) and Xu et al. (2025) find much lower values of  $\eta$  (0.1 – 1) and outflow velocities not large enough to escape from the gravitational potential of the hosts.

Although these previous JWST studies of ionized outflows at  $3 < z < 9$  are providing relevant information about their incidence, properties and impact on the host galaxies, all of them have been based on integrated information obtained from Multi Object Spectroscopy (MOS) or Wide Field Slitless Spectroscopy (WFSS). Moreover, they have targeted galaxies with  $\log(M_*/M_\odot) < 9.5$ , while the higher mass range of starbursts, a regime where outflows are theorized to be more

common but are increasingly suppressed by the deepening gravitational potential, remains to be explored. In this context, NIRSpec IFU observations provide, for the first time, the possibility to spatially resolve ionized outflows at high redshift. In fact, some studies have already started to identify and characterize spatially-resolved ionized outflows in star-forming galaxies at  $z > 3$  (Lamperti et al. 2024; Rodríguez Del Pino et al. 2024; Ivey et al. 2025; Parlanti et al. 2025; Marconcini et al. 2025; Scholtz et al. 2025a; Zamora et al. 2025a). In this work, we extend previous studies by exploiting NIRSpec IFU observations of a large sample of massive and luminous star-forming galaxies at  $3 < z < 9$  to provide a benchmark study of star-formation driven ionized outflows in the early Universe.

This paper is organized as follows. In Section 2 we describe the NIRSpec observations, the reduction, and the analysis of the data. Section 4 contains a description of the general properties of the sample and in Section 5 we describe the spectral modeling and the criteria to identify outflows. In Section 6 we present the main results obtained while a discussion on their implications is presented in Section 7. Finally, the summary of the main results and concluding remarks are presented in Section 8.

Throughout this paper, we adopt a Chabrier (2003) initial mass function ( $0.1 - 100 \text{ M}_\odot$ ) and a flat  $\Lambda\text{CDM}$  cosmology with  $H_0 = 70 \text{ km s}^{-1} \text{ Mpc}^{-1}$ ,  $\Omega_\Lambda = 0.7$ , and  $\Omega_m = 0.3$ . Emission lines are referred to using their rest-frame air wavelengths, although for the analysis we use their vacuum wavelengths.

## 2. Galaxy sample, observations and data reduction

### 2.1. GA-NIFS sample of star-forming galaxies

The data presented in this paper are part of the JWST Cycle 1 observations obtained within the NIRSpec IFS GTO program “Galaxy Assembly with NIRSpec IFS” (GA-NIFS<sup>1</sup>; PIs: S. Arribas, R. Maiolino). This program consists of more than 300 hours of NIRSpec/IFS observations of a sample of  $> 50$  galaxy systems at  $z \sim 2 - 11$ , including quiescent (D’Eugenio et al. 2023; Pérez-González et al. 2025), star-forming (SFGs; Arribas et al. 2024; Jones et al. 2024a,b; Lamperti et al. 2024; Rodríguez Del Pino et al. 2024; Jones et al. 2025; Parlanti et al. 2025; Marconcini et al. 2025; Scholtz et al. 2025a) and AGN galaxies (Marshall et al. 2023a; Perna et al. 2023; Übler et al. 2023; Parlanti et al. 2024; Perna et al. 2024; Übler et al. 2024a,b; Bertola et al. 2025; Marshall et al. 2025; Perna et al. 2025; Trefoloni et al. 2025; Zamora et al. 2025b). The GA-NIFS sub-sample of SFGs was selected with the goal of exploring the high-mass end of the star formation main sequence as well as bright starbursts at early epochs, favoring the selection of extended objects and/or presence of nearby companions, and therefore being appropriate for IFS studies and complementary to Multi Object Spectroscopy (MOS) survey samples (e.g. Bunker et al. 2024; Finkelstein et al. 2025; Maseda et al. 2024). The sample of SFGs was also chosen based on the absence of clear X-ray emission and of very broad emission lines that could be associated to the presence of an active supermassive black hole, based on pre-JWST observations. However, the classification of some of the formerly considered SFGs has been recently updated through the analysis of JWST NIRSpec/IFS data targeting the optical rest-frame emission that has revealed the presence of AGN activity (Übler et al. 2023, 2024a; Perna et al. 2025; Venturi et al. 2025).

After removing the previously identified AGN, we end up with a sample of 15 star-forming systems distributed in the

<sup>1</sup><https://ga-nifs.github.io/>

redshift range  $\sim 3 - 9$ . The individual properties of several of these systems have been already explored as part of the GA-NIFS survey, finding clear signatures of ionized outflows in some of them (e.g., Lamperti et al. 2024; Rodríguez Del Pino et al. 2024; Parlanti et al. 2025) and tentative evidence in others (e.g., Jones et al. 2024a,b). In this work we provide a systematic identification and characterization of ionized outflows in these previously studied SFGs and we present here for the first time an analysis of potential outflows in four further galaxies from GA-NIFS (GS\_23170, GS\_12306, EGSY8P7 and MACSJ0416-Y1), with the goal of exploring global properties of their spatially resolved outflows.

## 2.2. JWST/NIRSpec IFS Observations

The targets in our sample were observed with NIRSpec/IFS at high- (R2700) and low-resolution (R100/PRISM) configurations, with the exception of B14-65666 that was only observed at medium-resolution (R1000). Observations were included in proposals #1208 (PI: C. Willott), #1216, #1217, #1262 (PI: N. Luetzendorf), and #1264 (PI: L. Colina). The associated proposal IDs as well as the total exposure times for each galaxy are listed in Table 1. Observations were executed applying a medium (0.5'') cycling pattern of eight dithers, covering a contiguous area of  $3.1'' \times 3.2''$  with a native spaxel size of  $0.1''$  (Böker et al. 2022; Rigby et al. 2023). R100 observations provide a spectral resolution  $R \sim 30 - 330$  within  $0.6\mu\text{m} - 5.3\mu\text{m}$ , R1000 G395M/F290LP observations provide  $R \sim 700 - 1200$  within  $2.88\mu\text{m} - 5.20\mu\text{m}$ , whereas R2700 observations provide  $R \sim 1900 - 3500$  within  $1.7\mu\text{m} - 3.15\mu\text{m}$  and  $2.88\mu\text{m} - 5.20\mu\text{m}$  for G235H/F170LP and G395H/290LP, respectively.

## 2.3. Data reduction

Raw data were homogeneously reduced with the *JWST* Science Calibration pipeline<sup>2</sup> version 1.15.0 under the Calibration Reference Data System (CRDS) context jwst\_1241.pmap. Several modifications to the default reduction were introduced to improve the data quality (see Perna et al. 2023): count-rate frames were corrected for  $1/f$  noise through a polynomial fit, regions affected by failed open MSA shutters and strong cosmic ray residuals were masked after calibration in Stage 2, while the remaining outliers were flagged in individual exposures using an algorithm similar to LACOSMIC (van Dokkum 2001), rejecting the 95th (99.5th) percentile of the resulting distribution for the grating (R100/PRISM) observations. The reconstructed cubes of each dither position were combined using the ‘drizzle’ method, providing a pixel scale of  $0.05''$  in the final datacube. Background subtraction was performed by generating a master background spectrum using spaxels away from the emitting sources. Finally, since the noise provided in the ERROR extension of NIRSpec/IFS datacubes can be underestimated compared to the actual noise in the data (e.g., Rodríguez Del Pino et al. 2024), the ERROR vectors were re-scaled based on the standard deviation in continuum regions free of emission lines.

## 3. Analysis

### 3.1. Spectral modeling of emission lines

In this study we constrain the emission-line fluxes and kinematics of the ionized gas through the spectral modeling of the R2700 spectra (R1000 in the case of the B14 system). This analysis is performed on a spaxel-by-spaxel basis and in the integrated spectra extracted from different regions of the galaxies in our sample. Firstly, we perform the fitting of individual, strong emission lines (i.e., [O III]  $\lambda 5007$ , H $\alpha$ ) using a single Gaussian function to map the structure of the ionized emission (see Fig. 1). Secondly, a single Gaussian kinematic component is used to extract line fluxes from integrated regions by modeling the main optical emission lines available for each target (e.g., [O II]  $\lambda\lambda 3726, 29$ , H $\gamma$ , [O III]  $\lambda 4363$ , H $\beta$ , [O III]  $\lambda 5007$ , [Ne III]  $\lambda 3869$ , H $\alpha$ , [N II]  $\lambda 6584$  and [S II]  $\lambda\lambda 6716, 31$ ; see Sec. 4). Afterwards, we explore the presence of additional kinematic components in the spectra of our galaxies by including a second Gaussian kinematic component, with a larger velocity dispersion, in the spaxel-by-spaxel modeling of either [O III]  $\lambda 5007$  or H $\alpha$  (see Sec. 5). We consider that the emission from a kinematic component (either narrow or broad) is detected in any line when the maximum line flux is at least three times larger than the scatter in the neighboring continuum (i.e., signal-to-noise ratio,  $S/N, \geq 3$ ).

In the spectral modeling, all emission lines associated to a kinematic component (in the one- and two-component cases) are fit together tying their kinematics. The ratios [O II]  $\lambda 3729/\lambda 3726$  and [S II]  $\lambda 6716/\lambda 6731$  are constrained within [0.3839, 1.4558] and [0.4375, 1.4484], respectively, corresponding to the theoretical limits for low ( $1 \text{ cm}^{-3}$ ) and high ( $10^5 \text{ cm}^{-3}$ ) density regimes (Sanders et al. 2016). We assume the Calzetti et al. (2000) attenuation law and intrinsic values H $\alpha$ /H $\beta$  = 2.860 and H $\gamma$ /H $\beta$  = 0.468, corresponding to an electron temperature  $T_e = 10^4 \text{ K}$  and electron density of  $n_e = 100 \text{ cm}^{-3}$  for case B recombination (Osterbrock & Ferland 2006).

The spectral modeling is performed using a Bayesian approach based on Markov Chain Monte Carlo (MCMC) techniques. In particular, we employ the EMCEE software developed by Foreman-Mackey et al. (2013). The reported  $1-\sigma$  uncertainties on each parameter are calculated as half the difference between the 16th and 84th percentiles of the posterior probability density distribution. The spectral modeling takes into account the wavelength-dependent spectral resolution of NIRSpec (Jakobsen et al. 2022).

### 3.2. Stellar mass estimation

The available R100 NIRSpec/IFS observations for all galaxies in our sample provide access to their stellar emission, allowing the estimation of stellar masses. The only exceptions are the B14 system, which was observed in the R1000 configuration and lacks the depth to detect the stellar emission, and HFLS3, where the continuum emission is very weak. For the computation of the stellar masses we employ the integrated spectra extracted from the large apertures that encompass the extended emission of the ionized gas (pink apertures in Figure 1). The modeling of the spectral energy distribution is performed with the software Bagpipes (Carnall et al. 2019), that uses the Bruzual & Charlot (2003) stellar population models. We assume the same extinction for the stellar and nebular component and a Calzetti et al. (2000) dust attenuation law, with  $A_V$  varying between 0 and 3.0. The values for the ionization parameter ( $\log U$ ) and the metallicity

<sup>2</sup><https://jwst-pipeline.readthedocs.io/en/stable/jwst/introduction.html>

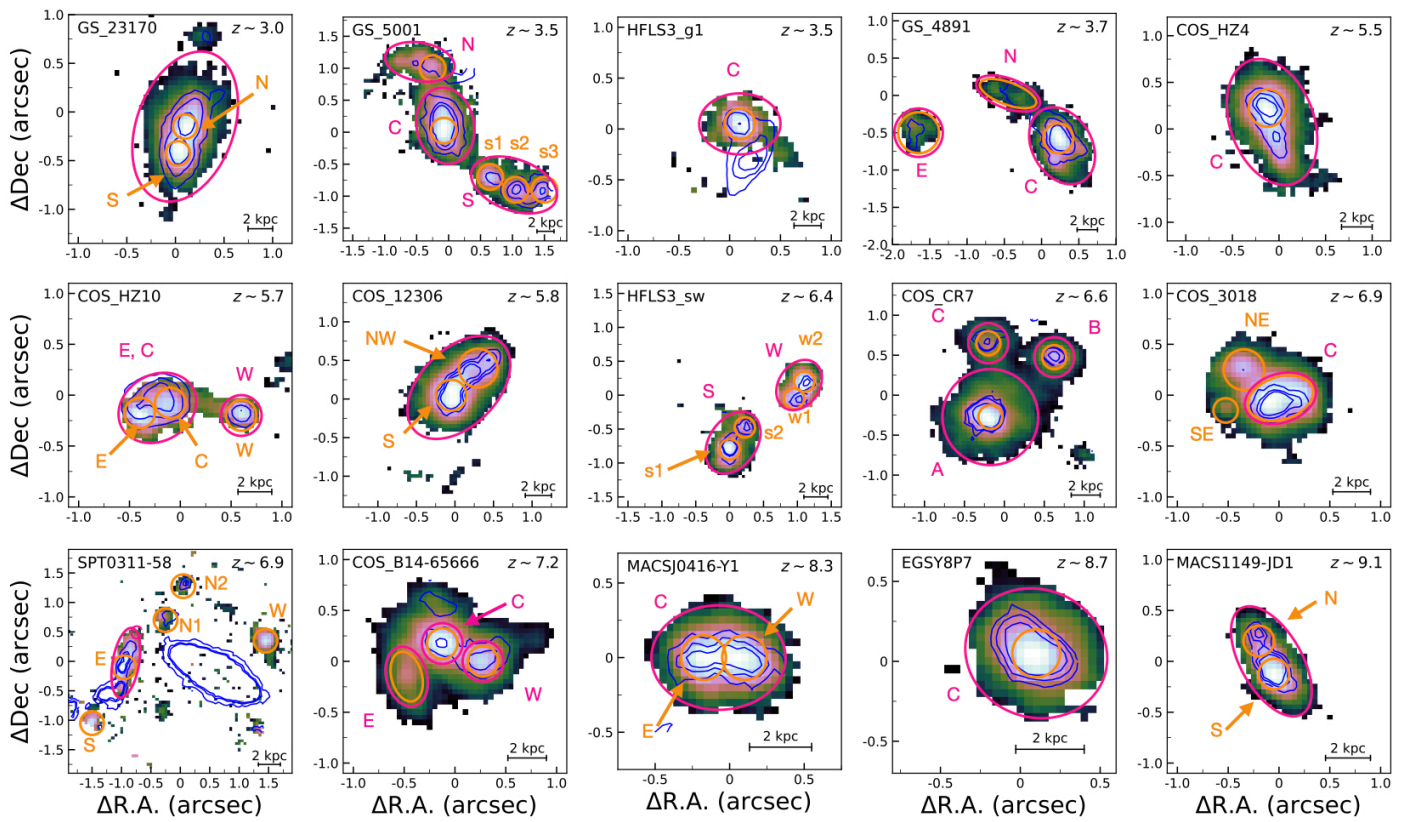


Fig. 1: Maps of integrated fluxes in [O III]  $\lambda 5007$  for all the galaxy systems in our sample, with the exception of HFLS3\_g1 for which we show integrated H $\alpha$  fluxes. Orange apertures mark small regions at the peaks of emission of the different (sub-) systems to constrain the dominant ionization mechanisms (see Figure 2 and Section 4.1). Pink apertures mark the larger regions used to study their extended emission. Blue contours correspond to the continuum emission at 2500-3000 $\text{\AA}$  rest-frame at different levels, starting from 3 $\times$  the standard deviation of the background. Note that for HFLS3\_g1 at  $z=3.5$ , these contours also include the emission from the  $z=6.3$  system.

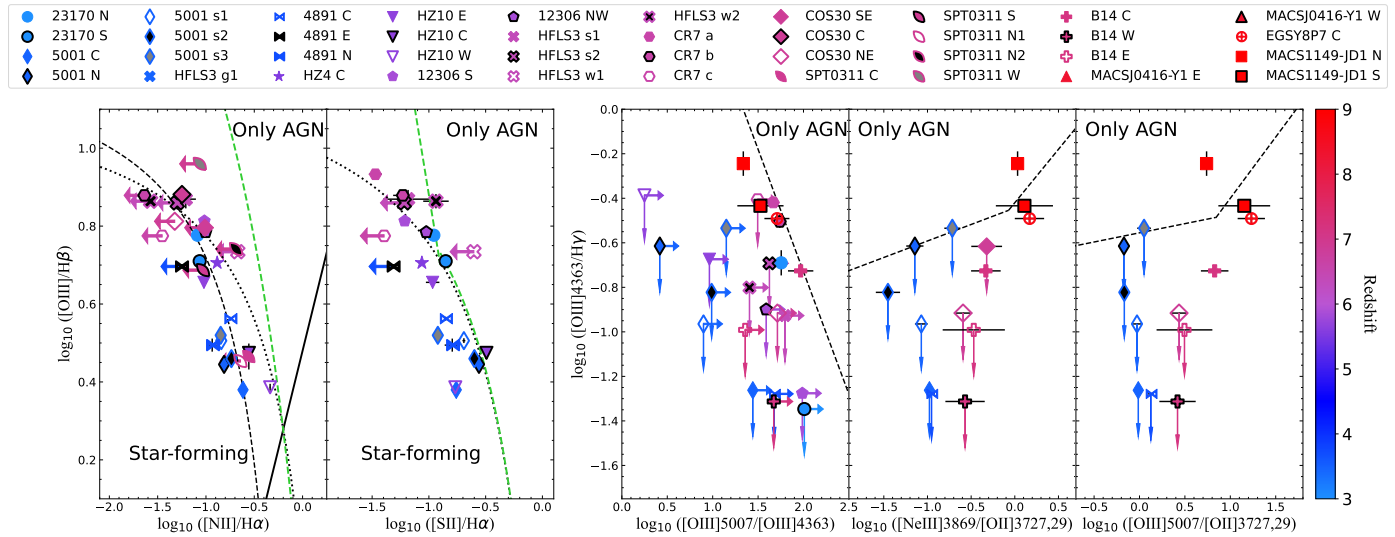


Fig. 2: Emission-line diagnostics for the galaxies in our sample obtained for the apertures highlighted in Figure 1. *Left:* BPT-NII and BPT-SII diagrams (Baldwin et al. 1981; Veilleux & Osterbrock 1987). Dashed (Kauffmann et al. 2003) and dotted black lines (Kewley et al. 2001) demarcate the separation between ionization coming from star formation and AGN activity based on studies of local galaxies. The dashed green lines in both plots have been recently proposed by Scholtz et al. (2025b) to conservatively separating AGN galaxies (see Sect. 4.1 for details). *Right:* Alternative diagnostic diagrams using  $[\text{O III}]\lambda 4363$  from Mazzolari et al. (2024)

Target	Galaxies / regions	Pointing R.A. (deg)	Pointing Dec. (deg)	Program	Redshift	$T_{\text{exp}} \text{ (s)}$ (R2700   R100)	$\log_{10} M_{\star} \text{ (M}_{\odot}\text{)}$	$\log_{10} SFR \text{ (M}_{\odot} \text{yr}^{-1})$
GS_23170	N, S	53.15746	-27.70911	1216	2.979	14705.6   3968.2	9.69	$1.70 \pm 0.01$
GS_5001	C	53.09725	-27.86588	1216	3.471	14705.6   3968.2	10.89	$2.02 \pm 0.01$
	N				3.474		9.86	$1.77 \pm 0.02$
	S (s1, s2, s3)				3.469		10.27	$1.73 \pm 0.01$
GS_4891	C	53.07621	-27.86644	1216	3.703	15872.7   3968.2	9.91	$1.61 \pm 0.01$
	E				3.703		8.64	$0.34 \pm 0.08$
	N				3.703		9.34	$0.73 \pm 0.05$
COS_HZ4	C	149.61884	+2.05187	1217	5.545	18206.9   3968.2	9.83	$1.73 \pm 0.01$
COS_HZ10	E, C	150.24713	+1.55534	1217	5.650	18206.9   3968.2	10.11	$1.83 \pm 0.02$
	W				5.659		10.10	$1.82 \pm 0.02$
COS_12306	S, NW	150.12746	+2.32643	1217	5.843	18206.9   3968.2	10.11	$2.21 \pm 0.01$
HFLS3 <sup>†</sup>	S (s1, s2)	256.69917	+58.77320	1264	6.359	7352.8   3559.7	—	$1.44 \pm 0.01$
	W (w1, w2)				6.359		—	$2.02 \pm 0.04$
	g1				3.480		—	$1.73 \pm 0.01$
COS_CR7	A	150.24169	+1.80424	1217	6.602	18206.9   3968.2	9.63	$1.70 \pm 0.01$
	B				6.599		9.10	$1.02 \pm 0.02$
	C				6.598		8.85	$0.79 \pm 0.03$
COS_3018	C, NE, SE	150.12577	+2.26661	1217	6.851	18206.9   3968.2	9.67	$1.84 \pm 0.01$
SPT0311-58	E, S, W, N1, N2	47.88858	-58.39264	1264	6.919	7352.8   3559.7	10.39	$1.88 \pm 0.08$
COS_B14-65666	C	150.41954	+1.91460	1217	7.153	14705.6 <sup>††</sup>	—	$1.63 \pm 0.08$
	W			1217	7.149		—	$1.96 \pm 0.11$
	E			1217	7.153		—	$1.46 \pm 0.15$
MACSJ0416-Y1	E, W	64.03926	-24.09319	1208	8.312	18206.9   3968.2	9.61	$1.55 \pm 0.15$
EGSY8P7	C	215.03542	+52.89072	1262	8.677	18206.9   3968.2	9.87	$1.99 \pm 0.14$
MACS1149-JD1	N, S	177.38992	+22.41269	1262	9.110	18206.9   3968.2	8.76	$2.40 \pm 0.15$

Table 1: Summary of targets considered in this study, including the ID of the system, the galaxies/regions identified in each of them, the RA, DEC of the pointing, the JWST program, the redshift of the source and the exposure times. We also include the  $SFRs$  and stellar masses ( $M_{\star}$ ) obtained for the large apertures highlighted in pink in Fig. 1 (see Sec. 3). Errors in  $\log_{10} M_{\star}$  are always smaller than  $0.05 M_{\odot}$ . <sup>†</sup> Jones et al. (2024b) identified 4 galaxies at  $z \sim 6.3$  (including ‘S’ and ‘W’) and a foreground galaxy (‘g1’) at  $z \sim 3.5$ . <sup>††</sup> COS\_B14-65666 was only observed at medium spectral resolution (R1000). More details about each system are provided in Section 6.1.

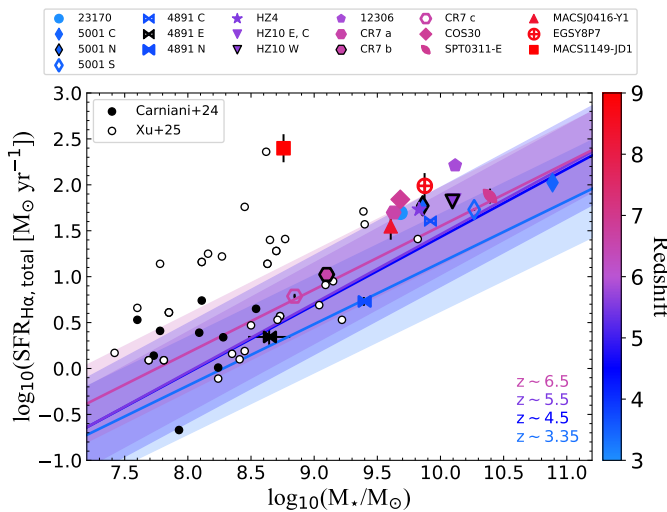


Fig. 3: Stellar mass vs total SFR for the individual star forming galaxies in our sample, color coded by redshift of the source. The values displayed are estimated from the large apertures highlighted in pink in Figure 1. Solid lines and shaded regions correspond to the star formation main sequence at different redshift bins and the associated scatter from Clarke et al. (2024). For comparison we show the sample of star forming galaxies with outflows at  $3 < z < 9$  from Carniani et al. (2024) and Xu et al. (2025).

( $Z$ ) are allowed to vary within the ranges  $[-3.5, -2.0]$  and  $[0.1 - 1 Z_{\odot}]$ , respectively, based on the values measured from their nebular emission (e.g. Lamperti et al. 2024; Rodríguez Del Pino et al. 2024). We consider a delayed exponential star formation history with a recent burst. For SPT0311-58-E, MACSJ0416-Y1 and MACS1149-JD1, which are lensed systems, stellar masses are estimated after correcting for magnification factors,  $\mu$ , of 1.15 (Arribas et al. 2024), 1.43 (Kawamata et al. 2016) and 10 (Marconcini et al. 2024), respectively. The estimated stellar masses for the galaxies/regions in our sample range within  $\log_{10} (M_{\star}/M_{\odot}) = 8.5 - 11$ . The individual values are included in Table 1.

#### 4. General properties of the sample

We start the characterization of the sample of star-forming systems by exploring the distribution of the ionized gas. We trace this gas through the  $[\text{O III}]\lambda 5007$  emission line, which is observed for all systems in our sample with the exception of HFLS3\_g1 (the additional galaxy at  $z \sim 3.5$  discovered in the foreground of the HFLS3 system at  $z = 6.3$  by Jones et al. 2024b), for which we use  $\text{H}\alpha$ . The maps of integrated line fluxes (obtained as described in Sec. 3.1 and when  $S/N > 3$ ), without applying a correction for dust attenuation, are shown in Figure 1, with blue contours highlighting the continuum emission at 2500-3000Å rest-frame. These maps of the ionized gas distribution illustrate the complexity of the systems, in many cases composed by several galaxies/regions.

Within these 15 complex systems, we identify numerous regions characterized by strong  $[\text{O III}]\lambda 5007$  or continuum emission. Based on this emission, we define a total of 40 regions that are associated to individual, detached galaxies, and to the peaks of  $[\text{O III}]\lambda 5007$  emission. These regions are highlighted in orange in Fig. 1 and listed in Table 1. We also define larger apertures encompassing the more extended emission, which are displayed in pink. For the subsequent analysis, we extract the integrated R100 and R2700 spectra within these apertures applying aperture corrections as described in Appendix A.

#### 4.1. Star formation as a dominant ionization mechanism

Since for this study we are interested in the characterization of feedback from star formation activity we need to work with a sample of galaxies that present no clear evidence of the presence of an AGN. To confirm the star forming nature of these complex systems and rule out clear evidence of AGN activity we study the spectra of the individual, nuclear regions (defined as orange apertures in Figure 1) that dominate the emission from the ionized gas. To determine the dominant ionization mechanism in each region, we explore in Figure 2 the location of the measured integrated line flux ratios (see Sect. 3.1) in the standard BPT-[NII] and BPT-[SII] diagnostic diagrams (Baldwin et al. 1981; Veilleux & Osterbrock 1987) as well as in the diagnostic diagrams recently developed by Mazzolari et al. (2024) which are based on  $[\text{O III}]\lambda 4363$ . The BPT diagrams include reference lines from studies of local galaxies that demarcate the regimes that could be explained considering only ionisation from star formation (below the black, dashed line from Kauffmann et al. 2003) and the one where theoretical models require the presence of AGN activity to explain the ionisation state of the gas (black, dotted lines from Kewley et al. 2001). In addition, we have also added the demarcation line (green) recently proposed by Scholtz et al. (2025b) to conservatively separate AGN. We only include measurements where the peak of the emission line has  $S/N > 3$  and employ  $1\sigma$  upper limits for the lines without a clear detection. The systems/galaxies included in each panel varies because of the different wavelength coverage of their rest-frame emission. The use of the BPT-[NII] diagram in high-redshift studies has raised concern because low metallicity AGN, typical of early cosmic epochs, tend to intrinsically present lower  $[\text{N II}]/\text{H}\alpha$  ratio, thus shifting towards the region of the diagram associated to ionization from star formation (Feltre et al. 2016; Übler et al. 2023; Scholtz et al. 2025b). This effect is not relevant for  $[\text{S II}]\lambda\lambda 6716, 31$ , although these lines are generally weak and/or outside the NIRSpec wavelength coverage at  $z > 6.5$ . Alternatively, the diagrams from Mazzolari et al. (2024) provide a cleaner selection of AGN as their higher ionization leads to a boost in the  $[\text{O III}]\lambda 4363$  emission compared to star forming galaxies. However, these diagrams only allow the identification of clear AGN cases, but cannot be used to discard the presence of AGN in systems without strong  $[\text{O III}]\lambda 4363$  emission. Despite these inherent caveats, we note that most of our sources lie in the regions of the diagrams that are not dominated by ionization from AGN. In the BPT-[NII] diagram all sources are on the left of the demarcation line by Scholtz et al. (2025b) while, in the BPT-[SII], three sources overlap with this conservative demarcation line, and only one (HFLS3\_w1) presents upper limits in the  $[\text{S II}]\lambda\lambda 6716, 31$  that are compatible with a clear AGN classification. A similar result is found in the  $[\text{O III}]\lambda 4363$ -based diagrams (three left panels in Fig. 2) where only MACS1149-JD1-N is located in the "Only AGN" region, just above the demarcation line, in two of the diagrams. Despite

the possible presence of an AGN in this galaxy, we keep it in our sample, bearing in mind that any outflow detected might also be driven by AGN activity. In the case of HFLS3\_w1, given that its possible AGN nature is only suggested by the BPT-[SII] using upper limits, we consider it as a star-forming system not dominated by AGN activity. Based on these diagnostic diagrams, and considering both the absence of X-ray emission and the lack of AGN-associated broad-line regions, we consider the classification of all other galaxies in the sample as SFGs to be robust.

Finally, as shown in the last two panels of Fig. 2, the  $[\text{Ne III}]\lambda 3869/[\text{O II}]\lambda\lambda 3726, 29$  and  $[\text{O III}]\lambda 5007/[\text{O II}]\lambda\lambda 3726, 29$  ratios clearly increase at higher redshifts, indicative of a higher ionization parameter at earlier epochs, as identified in other works (e.g., Cameron et al. 2023).

#### 4.2. Comparison with the general population of star-forming galaxies

In this section we compare the *SFRs* and stellar masses of our individual systems with the general population of star-forming galaxies at similar redshifts. We derive the *SFRs* using the line fluxes in  $\text{H}\alpha$  and  $\text{H}\beta$  measured in the one-component fit to the integrated spectra extracted from the same apertures used for the stellar mass estimates. We note that, although many of these systems present ionized outflows, most of the line flux extracted from the large apertures is recovered with a single component fit. The estimated line fluxes (see Sec. 3.1) are corrected for aperture losses and for magnification when required. We determine the nebular dust attenuation in our galaxies by comparing the observed and intrinsic ratios of a pair of Balmer emission lines, as in Domínguez et al. (2013). At  $z < 7$  we work with  $\text{H}\alpha$  and  $\text{H}\beta$ , while for higher redshift galaxies we employ  $\text{H}\beta$  and  $\text{H}\gamma$ . In the case of HFLS3\_g1 we do not cover any other hydrogen emission line apart from  $\text{H}\alpha$  and no dust correction can be estimated; thus, we compute lower limits on *SFR*. Finally, to convert  $\text{H}\alpha$  luminosities to *SFR* we apply the calibration from Clarke et al. (2024, ; Eq. 1), considering stellar metallicities  $Z_* = 0.004$ , which correspond to  $0.29 Z_\odot$  ( $12 + \log(\text{O/H}) = 8.15$ ), and assume a Chabrier (2003) IMF. The adopted metallicity for this calibration is consistent with the values of  $12 + \log(\text{O/H})$  measured in our work (see Sect. 6.2.2). For the galaxies at  $z > 7$  where we do not cover  $\text{H}\alpha$ , we infer its *SFR* from the  $\text{H}\beta$  and  $\text{H}\gamma$  and the estimated dust attenuation.

In Figure 3 we show the total *SFR* as a function of the stellar mass for our sample of star forming galaxies. As a reference, we include the 'star formation main sequence' (SFMS) relations derived at different redshift bins ([2.7, 4.0], [4.0, 5.0], [5.0, 6.0], [6.0, 7.0]) by Clarke et al. (2024), representing the general population of star forming galaxies. Since we do not provide a SFMS beyond  $z = 7$ , more distant galaxies (redder points in the plot) do not have a reference to compare with. We also add the samples of galaxies with ionized outflows at  $3 < z < 9$  from Carniani et al. (2024) and Xu et al. (2025), which also assume a Chabrier IMF. In general, our galaxies lie above the SFMS at their corresponding redshifts, indicating that most of them are observed in a star-bursting phase. Samples from previous works, especially in Xu et al. (2025), also present *SFRs* higher than those expected given their stellar masses. Besides that, our sample encompasses the higher mass end of the galaxy populations, with most of the sample having stellar masses within  $\log_{10}(\text{M}_*/\text{M}_\odot) = 8.5 - 11$ , while previous works generally contain galaxies with  $\log_{10}(\text{M}_*/\text{M}_\odot) < 9.5$ .

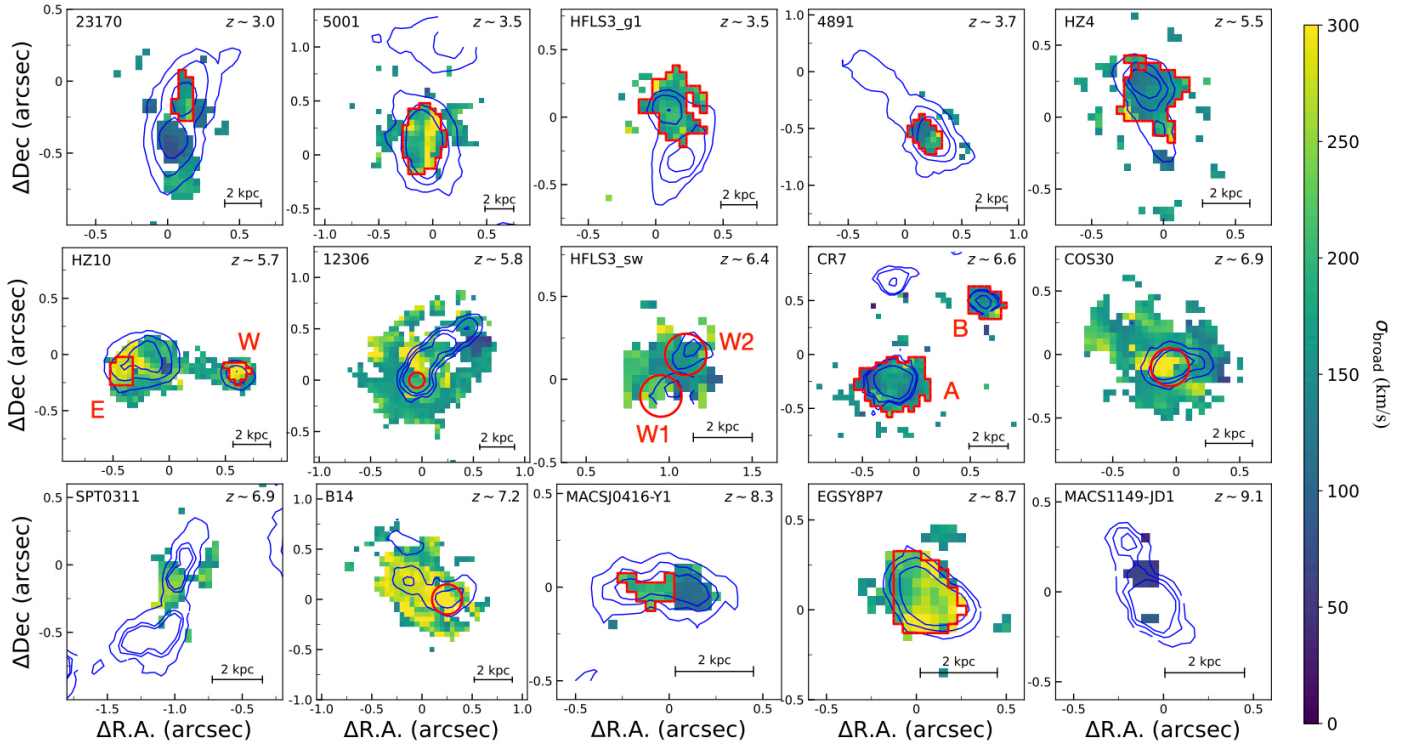


Fig. 4: Velocity dispersion maps of the broad component ( $\sigma_{\text{broad}}$ ) for all galaxies in our sample. The regions identified as outflows are highlighted in red. No outflows are identified in SPT0311-58 and MACSJ1149-JD1. Blue contours correspond to the stellar continuum emission, as in Fig. 1.

## 5. Identification of the regions hosting outflows

As described in Sec. 3.1, we perform the spectral modeling of the strong emission lines ( $[\text{O III}] \lambda 5007, \text{H}\alpha$ ) on a spaxel-by-spaxel basis using models with one and two kinematic components. The emission line profiles are considered to favor a two-component model when: (1) the Bayesian Information Criterion statistics (BIC; Schwarz 1978) is significantly better ( $> 10$ ) than for the one component model and (2) the narrow and broad components have  $S/N > 3$ . When two kinematic components are detected, the narrow one is associated to the host galaxy and is used to study its ISM properties and gas kinematics; the broad component is used to explore the presence and properties of galactic outflows.

The presence of mergers and substructures within our galaxy sample complicates the clear identification of outflows. This is because these violent events lead to an increase in the turbulence, tidal tails and overlap between different systems, that also produce a spectral broadening similar to that characteristic of outflows. Despite these uncertainties, our IFS data yield much better information than previous works based on MOS and WFSS spectra (e.g., Carniani et al. 2024; Xu et al. 2025), as they allow not only to determine better the extent of the broad component, but to isolate the emission from the region potentially hosting the outflows and adequately constrain the properties of the outflowing gas. Nevertheless, the definition of the outflowing regions requires a detailed inspection of the global kinematics of the gas, along with its connection to the stellar continuum emission coming from the starburst regions powering the star-formation driven outflows. In Figure 4 we present the velocity dispersion maps of the broad component (either from the one- or two-component fits) for all galaxies in our sample. These maps display extended regions of high

velocity dispersions of the broad component in most of the galaxies and demonstrate their complex morphologies and gas kinematics. To aid with the determination of the regions potentially hosting ionized outflows, we include in Figure 4 the continuum emission at 2500–3000Å rest-frame as blue contours, while in Appendix B we show the individual maps of line fluxes, velocity and velocity dispersion for the one- and two-component fits.

Based on all this information, we define the regions potentially hosting ionized outflows as those where two kinematic components are detected and the broad emission presents high velocity dispersion ( $\sigma_{\text{broad}} > 100 \text{ km/s}$ ). Moreover, as in Lamperti et al. (2024), we also interpret as potentially indicative of an outflow an emission line that is best-modeled with a single kinematic component that presents a significantly high velocity dispersion ( $> 140 \text{ km/s}$ ). In defining these regions, we ensure that they overlap with or are connected to the stellar continuum emission, as expected if the outflows are driven by star formation. This approach, however, may result in missing some outflows that, due to projection effects, are not co-spatial with the stellar emission. In this process, we conservatively exclude detached regions with high velocity dispersion that could be associated with tidally induced turbulence. As a result, we identify a total of 16 regions potentially hosting ionized outflows, which are highlighted in red in the velocity dispersion maps presented in Figure 4.

At this point, we acknowledge that the definition of the regions hosting outflows might be uncertain for some objects due to their complex nature, taking also into account that mergers and tidal interactions could contribute to the observed broad emission. Nevertheless, as we will see later in the paper, our results suggest that the present identification of the broad

component regions with outflows is globally correct, since the metallicity and dust attenuation in the broad component is, on average, enhanced with respect to the hosts (see Sec. 6.2.2). This behavior is not expected if the broad component is the result of a mixing mechanism, like those associated to interactions and mergers. However, for some individual sources the definition of regions hosting outflows on the basis of these admittedly simple criteria may be dubious. For instance, we find some cases with large red-shifted velocities ( $\Delta V \leq -200 \text{ kms}^{-1}$ ) with respect to the host galaxy (HZ10\_E and B14) that challenge the outflow scenario, since the redshifted component is expected to be obscured by the host galaxy. Even though these high- $z$  galaxies have relatively low extinction (see Sec. 6.2.2 and Table 2) and for some geometries the receding gas might appear to be in front of the galaxy from the observer's point of view, we consider these broad components as 'candidate' outflows (see further discussion in Sec. 7.2.2). Thus, although the measured properties of these two regions are listed in Table 2, we do not include them in our global analysis of the properties of ionized outflows in our sample. Finally, only two systems, SPT0311-58 and MACS1149-JD1, do not present evidence of hosting ionized outflows.

In some galaxies (4891, 5001, HFLS3\_g1, HZ4, CR7\_a, CR7\_b, EGSY8P7) we consider most of the extension of the broad emission as the region hosting the outflow, since they display relatively smooth variations in the velocity dispersion and largely overlap with the stellar continuum emission. In other galaxies that display a more clumpy structure (23170, HZ10\_E, HZ10\_W, MACSJ0416-Y1), we only consider the regions in the galaxy with the highest velocity dispersion. In the most complex systems that are mergers (12306, HFLS3\_w (1, 2), COS30 and B14) we adopt a conservative approach by considering only the nuclear region around the peak of stellar continuum emission, where the gas is expected to have shorter relaxation times and virialize faster, thus making a broad component more likely to be associated to outflowing gas.

To study the properties of the outflowing gas we extract the integrated spectra from the regions identified above (applying aperture corrections as described in Appendix A) and perform a two-component modeling of the main emission lines, tying the kinematics of all lines in the narrow and broad kinematic components. In this spectral modeling we apply the same constraints described in Sec. 3.1. We evaluate whether other emission lines apart from [O III]  $\lambda 5007$  and H $\alpha$  present a broad kinematic component by applying the criteria described in Section 5 individually for each line, finding that a broad component is frequently detected in H $\gamma$ , H $\beta$ , H $\alpha$  and [N II]. We show in Appendix D the modeling of the integrated outflow region in each galaxy, which includes the best fit model (one or two component) for each emission line.

## 6. Results

### 6.1. Overview of individual systems

As commented above, the presence of significant substructures and/or mergers in the systems in our sample poses a challenge in the identification of the regions that may host outflows since they also lead to turbulence, tidal tails and overlap between different galaxies that might also produce a spectral broadening similar to that characteristic of outflows. For this reason, the definition of the outflowing regions requires a detailed inspection of the global kinematics of the gas, along with its connection to the stellar continuum emission coming from starburst region

leading to the star-formation driven outflow. In Appendix B we analyze each galaxy/system in detail and define the regions considered to host ionized outflows. We base this definition on the velocity dispersion maps presented in Figure 4 and the individual kinematic maps also presented for each galaxy in the Appendix B.

We note here that the properties derived in this work (dust attenuation, oxygen abundance, kinematics) are consistent with those obtained in previous works on individual galaxies (e.g., Lamperti et al. 2024; Rodríguez Del Pino et al. 2024; Parlanti et al. 2025), but the actual values we obtained might differ slightly because of the different data processing steps (e.g., aperture corrections), selected regions and outflow selection criteria. A description of the findings in each system is given in Appendix B.

### 6.2. Characterization of the outflowing gas

In this section we constrain the main properties of the ionized outflows identified in our sample. We determine the spatial extent of the outflows, use the integrated spectra of these regions to estimate the dust attenuation and gas metallicity of the outflowing gas and compare them to those of the host galaxies, and compute the outflowing gas kinematics, exploring possible correlations with the properties of the host regions.

#### 6.2.1. Determination of the outflow size

The determination of the outflow sizes in the literature has been performed using a variety of methods. In recent studies of ionized outflows in high-redshift star-forming galaxies that used NIRSpec Multi-object spectroscopy and NIRCam Wide Field Slitless Spectroscopy (Carniani et al. 2024; Cooper et al. 2025; Xu et al. 2025), the extent of the outflow was considered to be the same as the host galaxy, thus employed the half-light radius of the source estimated from continuum imaging as the radius of the outflow. Our resolved velocity dispersion maps demonstrate that this approach might be valid for some sources where the outflow has a similar extension as the continuum emission (e.g., HZ4, EGSY8P7) but, in other cases, it can lead to underestimation (CR7\_a) or overestimation (4891) of the true extent of the outflow (see Fig. 4). These mismatches are likely related to the morphology of the source (clumpy or disk-like), the merging state and the orientation of the system with respect to the observer. In their study of [C II] outflows in main-sequence galaxies at  $z \sim 5$ , Birkin et al. (2025) assume an outflow radius of 6 kpc, following the sizes estimated from the stacking of marginally spatially resolved [C II] emission at high velocities by Ginolfi et al. (2020).

In our case, we benefit from the spatially resolved information provided by NIRSpec IFS data that allows the spatial extent of the broad emission to be constrained. Other works on ionized outflows using NIRSpec IFS data have estimated the radius of the outflow as the distance from the center of the galaxy to the region with high velocity dispersion (e.g. Lamperti et al. 2024) or have considered a flux-weighted approach (Bertola et al. 2025). In our sample, as can be seen in Figure 4, the morphology and size of the regions hosting the outflows is very heterogeneous. We follow two approaches to define the size of the regions hosting outflows. On the one hand, in the cases where the region with high velocity dispersion is relatively isolated and associated with continuum emission (23170, 5001, HFLS3\_g1, 4891, HZ4, HZ10 (E, W),

Outflow host (Galaxy/region)	$v_{\text{out}}$ (km s $^{-1}$ )	$\sigma_{\text{out}}$ (km s $^{-1}$ )	$A_{V,\text{narrow}}$	$A_{V,\text{broad}}$	$Z_{\text{narrow}}$	$Z_{\text{broad}}$	$r_{\text{out}}$ (kpc)	$\log_{10} SFR$ (M $_{\odot}$ yr $^{-1}$ )	$\eta = \dot{M}_{\text{out}}/SFR$
GS_23170	$179 \pm 8$	$135.7 \pm 4.4$	$0.05^{+0.09}_{-0.05}$	$1.57 \pm 0.12$	$8.26 \pm 0.07$	–	0.9	$1.5 \pm 0.4$	$1.5 \pm 0.37$
GS_5001	$218 \pm 6$	$172.5 \pm 3.4$	$0.77 \pm 0.04$	$2.54 \pm 0.09$	$8.52 \pm 0.04$	$8.51 \pm 0.05$	1.9	$2.0 \pm 0.7$	$0.13 \pm 0.02$
GS_4891	$272 \pm 9$	$157.6 \pm 4.6$	$1.39 \pm 0.06$	$0.18 \pm 0.14$	$8.33 \pm 0.06$	$8.57 \pm 0.06$	1.1	$1.5 \pm 0.1$	$0.01 \pm < 0.01$
COS_HZ4	$199 \pm 3$	$145.5 \pm 1.9$	$0.27 \pm 0.07$	$0.95 \pm 0.11$	$8.25 \pm 0.06$	$8.41 \pm 0.06$	1.4	$1.6 \pm 0.3$	$0.39 \pm 0.08$
COS_HZ10_E*	$480 \pm 12$	$259.8 \pm 6.2$	$0.80 \pm 0.14$	$1.75 \pm 0.18$	$7.59 \pm 0.29$	$8.47 \pm 0.07$	0.7	$1.2 \pm 0.3$	$0.55 \pm 0.14$
COS_HZ10_W	$416 \pm 26$	$264.0 \pm 13.0$	$1.57 \pm 0.36$	$2.41 \pm 0.21$	$8.55 \pm 0.08$	$8.56 \pm 0.06$	0.6	$1.7 \pm 0.8$	$1.72 \pm 0.65$
COS_12306	$313 \pm 8$	$175.2 \pm 4.2$	$1.26 \pm 0.18$	$1.01 \pm 0.07$	$8.2 \pm 0.09$	$8.19 \pm 0.08$	1.7	$1.7 \pm 0.5$	$1.0 \pm 0.23$
HFLS3_w1	$297 \pm 16$	$230.4 \pm 8.3$	$0.67 \pm 0.43$	$2.66 \pm 0.31$	$8.23 \pm 0.14$	$8.39 \pm 0.09$	0.7	$1.8 \pm 1.1$	$5.06 \pm 2.59$
HFLS3_w2	$317 \pm 11$	$156.3 \pm 5.5$	$1.84 \pm 0.23$	$1.18 \pm 0.26$	$7.99 \pm 0.18$	$8.28 \pm 0.14$	0.7	$1.6 \pm 0.8$	$0.36 \pm 0.15$
HFLS3_g1	$462 \pm 88$	$330.7 \pm 44.2$	–	–	–	–	1.7	$> 0.6$	$< 0.01$
COS_CR7_a	$189 \pm 2$	$153.9 \pm 1.2$	$0.01^{+0.03}_{-0.01}$	$0.88 \pm 0.09$	$7.83 \pm 0.14$	–	1.6	$1.7 \pm 0.3$	$0.77 \pm 0.3$
COS_CR7_b	$169 \pm 4$	$142.4 \pm 2.3$	$0.01^{+0.06}_{-0.01}$	$0.48 \pm 0.21$	$7.96 \pm 0.18$	–	0.9	$1.0 \pm -0.1$	$0.8 \pm 0.39$
COS_3018	$448 \pm 18$	$334.3 \pm 9.0$	$1.00 \pm 0.04^{\dagger}$	–	$7.94 \pm 0.11$	–	0.8	$> 1.2$	$0.09 \pm < 0.01$
COS_B14*	$586 \pm 10$	$324.1 \pm 5.3$	$1.73 \pm 0.32^{\dagger}$	–	$8.11 \pm 0.22$	$8.28 \pm 0.41$	0.8	$1.6 \pm 1.0$	$0.58 \pm < 0.01$
MACSJ0416-Y1	$251 \pm 14$	$193.7 \pm 7.5$	$0.18^{+0.26^{\dagger}}_{-0.18}$	–	$7.90 \pm 0.22$	–	0.5	$> 1.2$	$1.55 \pm 1.05$
EGSY8P7	$266 \pm 5$	$214.3 \pm 2.6$	$0.74 \pm 0.35$	$1.27 \pm 0.68$	$7.67 \pm 0.23$	–	1.0	$2.3 \pm 1.9$	$0.66 \pm 0.61$

Table 2: Summary of outflow properties.  $\sigma_{\text{out}}$  and  $v_{\text{out}}$  are the velocity dispersion and maximum velocity of the outflows.  $A_{V,\text{narrow}}$  and  $A_{V,\text{broad}}$  are the dust attenuation in the narrow (systemic) and broad (outflow) kinematic components, estimated from H $\alpha$  and H $\beta$  fluxes (at  $z < 7$ ) from H $\beta$  and H $\gamma$  fluxes (at  $z > 7$ ).  $A_{V,\text{broad}}$  is only provided when a broad component is clearly detected in both emission lines.  $Z_{\text{narrow}}$  and  $Z_{\text{broad}}$  are the oxygen abundances (12+log(O/H)) in the narrow and broad components, respectively.  $Z_{\text{broad}}$  values are provided for galaxies in which we detect broad emission lines in H $\beta$ , [O III], H $\alpha$ , [N II] and we could estimate the metallicity using the R3 and N2 metallicity indicators.  $r_{\text{out}}$  is the size of the outflow,  $M_{\text{out}}$  is the mass of outflowing gas and  $\eta$  is the mass-loading factor. \*Candidate outflows.  $^{\dagger}A_{V,\text{narrow}}$  values estimated from the single component fit.

CR7 (a,b), MACSJ0416-Y1, EGSY8P7) we compute the radius of the outflow,  $r_{\text{out}}$ , as the circularized radius of the region hosting the outflow (i.e., the area of the regions highlighted in red in Fig. 4), as in Rodríguez Del Pino et al. (2024). On the other hand, in the cases where the broad emission presents a large extension beyond the continuum emission, suggesting that tidal interactions or mergers could also be inducing the broad emission (HFLS3\_w (1,2), 12306, B14, COS30), we define small, circular regions with  $r_{\text{out}} = 0.25 - 0.3''$  around the peak of continuum emission, assuming that in these cases the outflow could have a larger extension. We also note that our size estimations should be considered as lower limits, since what we observe are projected sizes on the sky. The estimated values of  $r_{\text{out}}$  are listed in Table 2. The ionized outflows in our sample have a mean extent of  $r_{\text{out}} = 1.1$  kpc, ranging from a minimum of 0.5 kpc (MACSJ0416-Y1) to a maximum of 1.7 kpc (HFLS3\_g1, 12306). These sizes are generally larger than those estimated by Carniani et al. (2024) for their sample of outflows in lower-mass ( $\log_{10} (M_{\star}/M_{\odot}) < 9.5$ ) galaxies at  $3 < z < 9$  based on the continuum emission from the host, finding in most of the cases  $r_{\text{out}} < 1$  kpc and a mean size  $r_{\text{out}} = 0.67$  kpc.

### 6.2.2. Dust attenuation and gas metallicity of the outflows

The detection of a broad kinematic component across multiple emission lines in the integrated spectra of the outflows offers the opportunity to probe the properties of the outflowing gas in detail and directly compare them with those of the host galaxy. In this section we focus on the study of the dust attenuation and metallicity of the different gas components.

Applying the same method described in Section 4.2, we determine the dust attenuation in the narrow (systemic) and broad (outflow) kinematic components using a pair of Balmer emission lines, H $\alpha$  and H $\beta$  for galaxies at  $z < 7$  and H $\beta$  and H $\gamma$

for those at  $z > 7$ . We could perform an estimation of  $A_{V,\text{broad}}$  only when a broad component is clearly detected ( $S/N > 3$ ) in both emission lines. This estimation is possible in the integrated spectra of 12 regions, while in the rest a broad line is only detected in one Balmer emission line (HFLS3\_g1, COS3018, MACSJ0416-Y1 and B14). In the left panel of Figure 5 we show a comparison between  $A_{V,\text{narrow}}$  and  $(A_{V,\text{broad}}$ , with a dashed line demarcating the one-to-one relation (in this plot we exclude the candidate outflows in HZ10\_E and B14). We find that the dust attenuation is generally higher in the outflowing gas, where it reaches values as high as  $\sim 2.6$  mag, while only two galaxies display higher attenuation in the host galaxy. On average, the dust attenuation in the outflowing gas is  $\sim 0.59$  mag higher than in the systemic component (host galaxy).

To constrain the gas metalicities we use standard metallicity indicators based on optical emission lines such as R2 ([O II]  $\lambda\lambda 3726, 29/\text{H}\beta$ ), R3 ([O III]  $\lambda 5007/\text{H}\beta$ ) and N2 ([N II]  $\lambda 6584/\text{H}\alpha$ ). We separately estimate the gas metallicity in the narrow (systemic) and broad (outflow) kinematic components when a broad component is detected in enough emission lines to compute, at least, two metallicity indicators. Such a requirement is satisfied in seven galaxies in our sample for R3 and N2. In the other systems, we compute the metallicity using the line fluxes from the single kinematic component fit. Line fluxes are corrected for dust attenuation when the indicators use emission lines with large wavelength separation (e.g., R2). Oxygen abundances are computed using the recent calibrations based on star-forming galaxies at  $z = 1.4 - 7.2$  for local galaxies from the AURORA survey Sanders et al. (2025) for the two indicators, which are combined to find a common value and provide the associated uncertainties. The right panel of Figure 5 presents a comparison of the oxygen abundance in the narrow (systemic) and broad (outflow) components, with a dashed line demarcating the one-to-one relation. All seven galaxies for

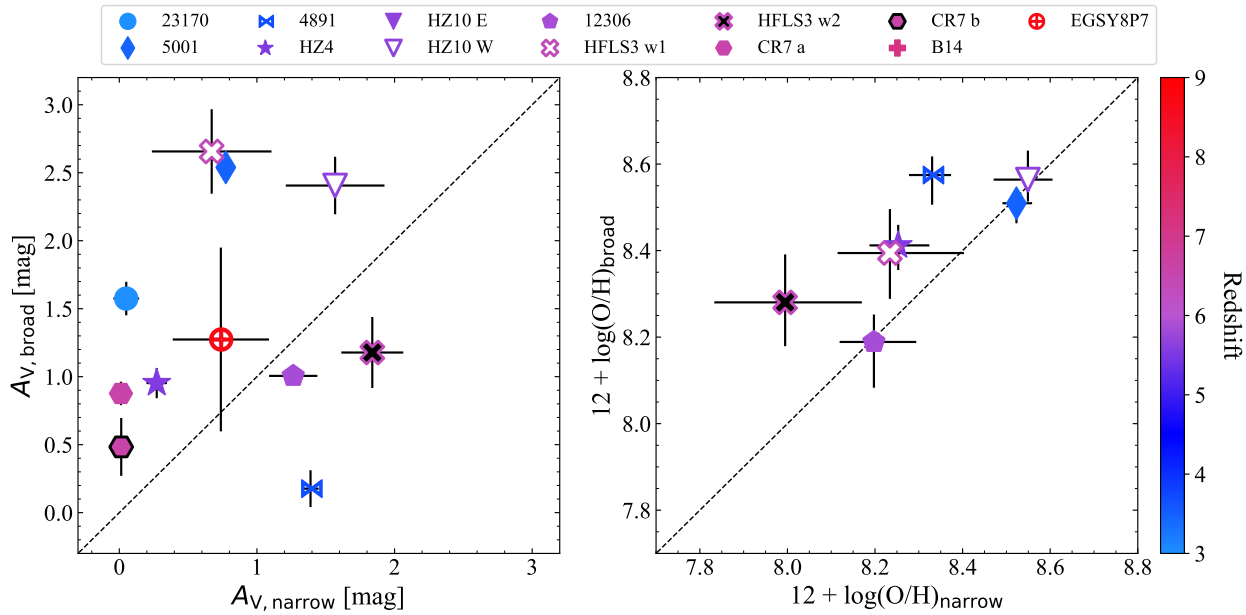


Fig. 5: Comparison of the nebular dust attenuation (left) and gas metallicity (right) for the narrow and broad components in the galaxy regions in our sample identified to host ionized outflows. Symbols are color-coded according to the redshift of the galaxies. The black dashed lines show the one-to-one relation.

which this comparison can be done are at  $z < 6.5$ . Remarkably, all the points lie on top or above the one-to-one relation, indicating that the outflowing gas is more metal-enriched than the gas in the host galaxies. On average, outflowing gas presents  $\sim 0.13$  dex higher oxygen abundances. At this stage, we note that the high metallicities in the outflowing gas could be due to the enhancement in N2 expected in shocks (e.g., Ho et al. 2014). However, we do not expect this effect to be relevant since we require an additional metallicity indicator, which is generally R3, to reduce degeneracies in the estimations of the oxygen abundances. We discuss the implications of these findings in Sect. 7.2.2.

### 6.2.3. Outflow kinematics

In this section we explore the variation of the kinematic properties of the outflowing gas as a function of the properties of the host regions. From the spectral modeling of the integrated spectra of the outflows we derive the Full Width at Half Maximum of the broad component,  $FWHM_{\text{out}}$ , and the velocity difference between the broad and narrow kinematic components,  $\Delta V = v_{\text{out}} - v_{\text{narrow}}$ , which are used to define the outflow velocity as  $v_{\text{out}} = |\Delta V| + FWHM_{\text{out}}/2$ , following Xu et al. (2025). To estimate the total, attenuation-corrected,  $H\alpha$  luminosity ( $L_{H\alpha}$ ) of the host regions we use total line fluxes including all kinematic components, thus assuming that the outflow emission is due to photons escaping from the star-forming regions and ionizing the outflowing gas, rather than in-situ star formation within the outflow. We derive the  $SFRs$  from  $L_{H\alpha}$  as in Sec. 4.2 and compute the  $H\alpha$  luminosity surface density (thus  $\Sigma_{\text{SFR}}$ ) using the outflow sizes estimated in Sec. 6.2.1. It is worth noting here that an adequate estimation of  $\Sigma_{\text{SFR}}$  is possible thanks to the spatially resolved information provided by our NIRSpec IFS observations. We also explore variations as a function of the stellar mass of the host galaxies/regions using the values obtained in Sec. 3 for the large apertures (pink) defined in Fig. 1.

In Fig. 6 we show a comparison between the kinematic properties of the outflow ( $\sigma_{\text{out}}$ ,  $\Delta V$ ,  $v_{\text{out}}$ ) and the properties of the host. For comparison, we also include in the plots the samples of outflows from Carniani et al. (2024), Ivey et al. (2025) and Xu et al. (2025). At a first glance, these plots highlight that our sample of galaxies covers higher values of SFR and stellar mass than previous studies. Thus, this expanded parameter space allows us to conduct a comprehensive census of galactic outflows at  $3 < z < 9$  across a wide a range of stellar masses and SFRs.

As shown in the plots in the top row of Fig. 6, our sample of ionized outflows display velocity dispersions, traced by  $\sigma_{\text{out}}$ , within  $\sim 130 - 340$  km/s, similar to those measured in less luminous and less massive star-forming galaxies in previous works. The velocity dispersion does not seem to vary as a function of the host properties within the wide ranges we probe. The distribution of the  $\Delta V$  values presented in the middle panels illustrates that most of the outflows we identify are blue-shifted with respect to the systemic emission or present slightly red-shifted, positive velocity differences  $< 100$  km/s. There are only two outflows in our sample with large, positive velocities  $\sim 200$  km/s, HZ10\_E and B14. As explained in Section 5, we consider these outflows as ‘candidates’, since in a standard outflow scenario we would expect to see the unattenuated blue-shifted gas while the redshifted emission is more likely to be obscured by the host galaxy. Nevertheless, as shown in the plots, we note that red-shifted outflows are also reported in the previous works by Carniani et al. (2024) and Ivey et al. (2025), suggesting that the geometry and dust distribution can frequently make the red-shifted outflowing gas more prominent than the blue-shifted counterpart. Red-shifted broad components can also be explained by gas inflows of pristine gas, however, our results of a higher metallicity in the outflowing gas (see Sec. 6.2.2) does not support this scenario.

Finally, it is noticeable that at high SFRs ( $> 1.5 M_{\odot} \text{yr}^{-1}$ ) and high stellar masses ( $\log_{10} (M_{\star}/M_{\odot}) > 9.5$ ), ranges mostly covered by our sample but also by Xu et al. (2025), the

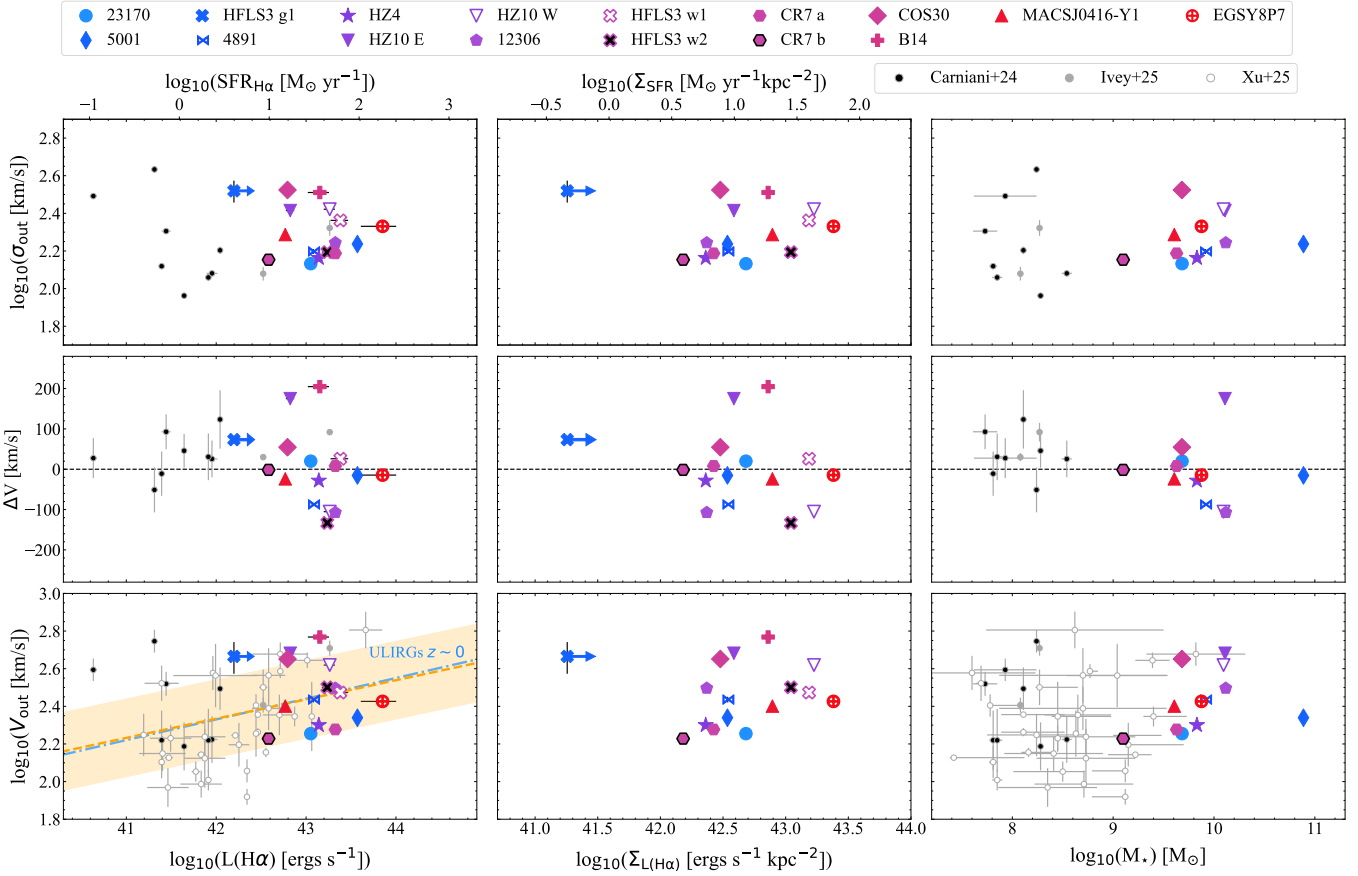


Fig. 6: Kinematic properties of the outflows,  $\sigma_{\text{out}}$ ,  $\Delta V$ ,  $V_{\text{out}}$ , compared to host properties,  $L_{\text{H}\alpha}$  (SFR),  $\Sigma_{L(\text{H}\alpha)}$  ( $\Sigma_{\text{SFR}}$ ),  $M_*$ . Large symbols correspond to the outflows identified in our study, and are color-coded according to their redshifts, as in Fig. 5. Results from previous studies of ionized outflows at  $3 < z < 9$  are shown as small black, gray and white circles (Carniani et al. 2024; Ivey et al. 2025; Xu et al. 2025). In the bottom-left panel we show as an orange, dashed line, the best fit to the data points, together with a shaded region marking the  $1-\sigma$  scatter. The data presents a statistically significant ( $> 3\sigma$ ) positive correlation. For comparison, in that panel we also show as a blue, dot-dashed line, the correlation found for local ULIRGs by Arribas et al. (2014).

outflows present  $v_{\text{out}} > 150 - 200$  km/s, while outflows at lower SFRs and stellar masses can have lower velocities, down to 100 km  $\text{s}^{-1}$ . Moreover, supported by these different velocity regimes, we identify a trend of increasing  $v_{\text{out}}$  as a function of  $L(\text{H}\alpha)$  including all samples, with a Spearman's correlation test probability  $> 3\sigma$ . The best linear fit to the data points (with a slope of  $\sim 0.098$ ) is shown (orange, dashed line) in the bottom-left panel of Fig. 6. We also show the relation found for local ULIRGs (blue, dot-dashed line) by Arribas et al. (2014) shifted to match at  $L(\text{H}\alpha) = 10^{42.5} \text{ L}_\odot$ , which is obtained within a similar range in SFRs using also  $\text{H}\alpha$ , although with a slightly different definition of  $v_{\text{out}}$ . Remarkably, the two correlations have a very similar slope indicating that, regardless of the cosmic time, there is a expected range in the velocity of ionized outflows at a given SFR. We do not find statistically significant correlation between  $\sigma_{\text{out}}$ ,  $v_{\text{out}}$  and the host properties  $\Sigma_{L(\text{H}\alpha)}$  nor  $M_*$ . Although not shown in the plot, we also explore correlations between the kinematics and the specific star formation rate  $SSFR$ , finding no significant trends.

## 7. Discussion

### 7.1. High prevalence of ionized outflows

We have identified ionized outflows in 14 out of the 40 individual star-forming galaxies/regions explored in our sample of 15 complex systems. Compared to previous works covering similar redshifts ( $3 < z < 9$ ), this incidence of outflows ( $\sim 35\%$ ) is similar to that reported by Carniani et al. (2024, 25-40% in the sample of 52 galaxies), but higher than in the works by Cooper et al. (2025, 3.4% (34/1007)) and Xu et al. (2025, 23% (30/130)). These differences can be ascribed to several factors, including (1) the stellar mass coverage ( $\log_{10}(M_*/M_\odot) = 8.5 - 11$ ), (2) the type and depth of the observations and (3) the outflow selection criteria. (1) Regarding stellar mass, our sample of galaxies with identified outflows have stellar masses within  $\log_{10}(M_*/M_\odot) = 8.75 - 10.9$ , while previous works generally contain galaxies with  $\log_{10}(M_*/M_\odot) < 9.5$ . Given that the incidence of outflow has been observed to increase with stellar mass at low (e.g. Rodríguez Del Pino et al. 2019) and high redshift (e.g. Carniani et al. 2024), it is expected that our sample presents a higher incidence than previous works that studied lower mass systems. (2) The spatial resolution of our IFS observations allows us to isolate the regions potentially hosting ionized outflows, extract all the emission from the outflows that might be missed in

MOS observations, and minimize contamination from mergers that might present similar spectral signatures. However, with our data is less challenging and subject to lower uncertainties than for the NIRCam Wide Field Slitless and NIRSpec MSA observations used in the works mentioned above. Moreover, the high spectral resolution (R2700) of our observations (with the exception of B14 that was observed with R1000) also enhances the detectability of a possible broad component. This result is demonstrated by the increasing fraction of outflows (from 23% to 30%) identified in Xu et al. (2025) when only high resolution observations are considered and by the low incidence of outflows reported in Cooper et al. (2025) where only R1000 data was employed. (3) The outflow selection criteria in individual studies, including ours (see Sec. 5), generally require a minimum S/N (e.g.  $> 3$ ) in the broad component and a statistical improvement in the spectral modeling that favors a secondary kinematic component associated to an outflow. Although each study applies different thresholds to these criteria, they are expected to be reasonably consistent. However, a direct comparison of the criteria would be needed to properly quantify any potential differences, but this is beyond the scope of this work.

The detection of ionized outflows in most of our systems resembles the results from studies of local Ultra Luminous Infrared Galaxies (ULIRGs) where ionized outflows are ubiquitous (e.g. Bellochi et al. 2013; Arribas et al. 2014) due to their high masses ( $\log_{10} (M_*/M_\odot) > 9.5$ ) and star formation rates ( $> 1.5 M_\odot \text{yr}^{-1}$ ). In addition, similar to our sample of star forming galaxies, local ULIRGs also tend to display high disordered motions and signatures of ongoing mergers (Crespo Gómez et al. 2021; Perna et al. 2022). Finally, our results are also comparable to the widespread presence of outflows found in AGN at  $z \sim 3$  (Bertola et al. 2025; Venturi et al. 2025) and at  $z > 4$  (Marshall et al. 2023b; Loiacono et al. 2024; Liu et al. 2024; Suh et al. 2025) also with NIRSpec IFS observations.

## 7.2. Impact on the host galaxy

Although starburst-driven outflows are expected to have a lower impact on the host galaxies than AGN-driven ones, they might still affect their star formation activity (e.g. Carniani et al. 2024) and play an important role in the regulation of the metal content in galaxies (e.g., Chisholm et al. 2018). In this section we explore these two scenarios.

### 7.2.1. Limited ejective feedback in high- $z$ star-forming systems

A common approach to assessing whether outflows are suppressing star formation in their host galaxies is to compare the outflowing mass rate,  $\dot{M}_{\text{out}}$ , that is the rate at which gas is expelled from the SF region, with the  $SFR$ , which quantifies the rate at which gas is converted into stars. The ratio between these two quantities is known as the mass loading factor,  $\eta = \dot{M}_{\text{out}}/SFR$ . A value of  $\eta > 1$  is interpreted as an indication that the outflow is suppressing star formation in the host. To estimate the outflow rate, we assume a conical outflow with a constant mass outflow rate with time (Lutz et al. 2020), which is given by

$$\dot{M}_{\text{out}} = M_{\text{out}} v_{\text{out}} / r_{\text{out}}, \quad (1)$$

where  $M_{\text{out}}$  is the mass of the outflowing gas and  $r_{\text{out}}$  is the size of the outflow (e.g., Maiolino et al. 2012; González-Alfonso

et al. 2017). We continue by estimating  $M_{\text{out}}$  following the method outlined in Carniani et al. (2024), specifically their Equation 4, which we reproduce below:

$$M_{\text{out}} = 0.8 \times 10^8 \left( \frac{L_{[\text{OIII}],\text{out}}^{\text{corr}}}{10^{44} \text{ erg s}^{-1}} \right) \left( \frac{Z_{\text{out}}}{Z_\odot} \right)^{-1} \left( \frac{n_{\text{out}}}{500 \text{ cm}^{-3}} \right)^{-1} M_\odot, \quad (2)$$

$L_{[\text{OIII}],\text{out}}^{\text{corr}}$  is the  $[\text{O III}]$  luminosity of the broad component corrected for dust attenuation whereas  $Z_{\text{out}}$  and  $n_{\text{out}}$  are the metallicity and electron density of the outflow, respectively. We perform the correction for dust attenuation in the broad component using the  $A_{\text{V},\text{broad}}$  values estimated in Sect. 6.2.2. In the four cases (HFLS3\_g1, COS30-18, B14 and MACSJ0416-Y1) where  $A_{\text{V},\text{broad}}$  could not be estimated, we assume that the dust attenuation in the outflow is the same as in the host. Regarding the metallicity of the outflow, we use individual estimates for the galaxies where we could measure it directly from the spectra (see Sect. 6.2.2), while for the rest of systems we assume for the outflow the same gas metallicity estimated for the systemic component. Finally, an accurate determination of the electron density of the outflow remains challenging, primarily because the  $[\text{O II}]$  and  $[\text{S II}]$  emission line doublets required for such measurements are frequently blended or display insufficient S/N. Due to this difficulty, we consider the same electron density for the outflow and systemic components. Given that previous works have estimated the electron density of the host galaxies we employ those values when available:  $540 \text{ cm}^{-3}$  for 5001 (Lamperti et al. 2024);  $776 \text{ cm}^{-3}$  for 4891 (Rodríguez Del Pino et al. 2024);  $270 \text{ cm}^{-3}$  for HZ4 (Parlanti et al. 2025);  $1000 \text{ cm}^{-3}$  for HZ10\_E and  $316 \text{ cm}^{-3}$  for HZ10\_W (Jones et al. 2025);  $1200 \text{ cm}^{-3}$  for COS3018 (Scholtz et al. 2025a);  $2200 \text{ cm}^{-3}$  for EGSY8P7 (Zamora et al. 2025a)). For the remaining 9 galaxies/regions we adopt a common value of  $500 \text{ cm}^{-3}$  based on the measured electron densities within  $3 < z < 9$  in Isobe et al. (2023, see also Marconcini et al. 2024). Under these assumptions, we use Eq. 2 to estimate the mass of the outflowing gas for the whole sample, which is found to range between  $\sim 10^6$  and  $\sim 9 \times 10^8 M_\odot$ .

With these estimations of the outflowing gas mass together with the values derived for the outflow velocity,  $v_{\text{out}}$ , in Sect. 6.2.3 and for the outflow radius,  $r_{\text{out}}$ , in Sect. 6.2.1, we calculate the mass outflow rate,  $\dot{M}_{\text{out}}$ , using Eq. 1, and the mass loading factor  $\eta$ . The estimated values of  $\eta$  for the outflows identified in this work are listed in Table 2 and shown in Fig. 7 as a function of the  $SFR_{\text{H}\alpha}$  (derived from the  $\text{H}\alpha$  luminosity,  $L_{\text{H}\alpha}$ ; left) and the stellar mass of the hosts (right) in comparison with other works at similar redshifts. In our sample,  $\eta$  ranges from  $< 10^{-3}$  to 12, with 4 out the 14 outflows presenting values above unity. These results suggest that in these four systems, outflows may be actively suppressing star formation in the host galaxies, whereas in the rest of the sample, their impact on star formation appears to be less significant. Taking previous studies into account, the range of  $\eta$  values we find in our sample appears more consistent with the results of Xu et al. (2025), who report no outflows with  $\eta$  values exceeding 1. In contrast, Carniani et al. (2024) find that the majority of their outflows, 10 out of 14, have  $\eta > 1$ . We note that, if instead of adopting the value of  $n_{\text{e,out}} = 500 \text{ cm}^{-3}$  for the outflows without a measurement of the host  $n_{\text{e}}$ , we adopted a value of  $n_{\text{e}} = 380 \text{ cm}^{-3}$  from Carniani et al. (2024),  $\eta$  would increase by 30%, having two more outflows with  $\eta > 1$ . Alternatively, if we used the redshift-dependent scaling relation from Isobe et al. (2023), assuming  $n_{\text{e}} = 1000 \text{ cm}^{-3}$  at  $z = 8$  as in Xu et al. (2025), the number of outflows with  $\eta > 1$  in our work would remain unchanged.

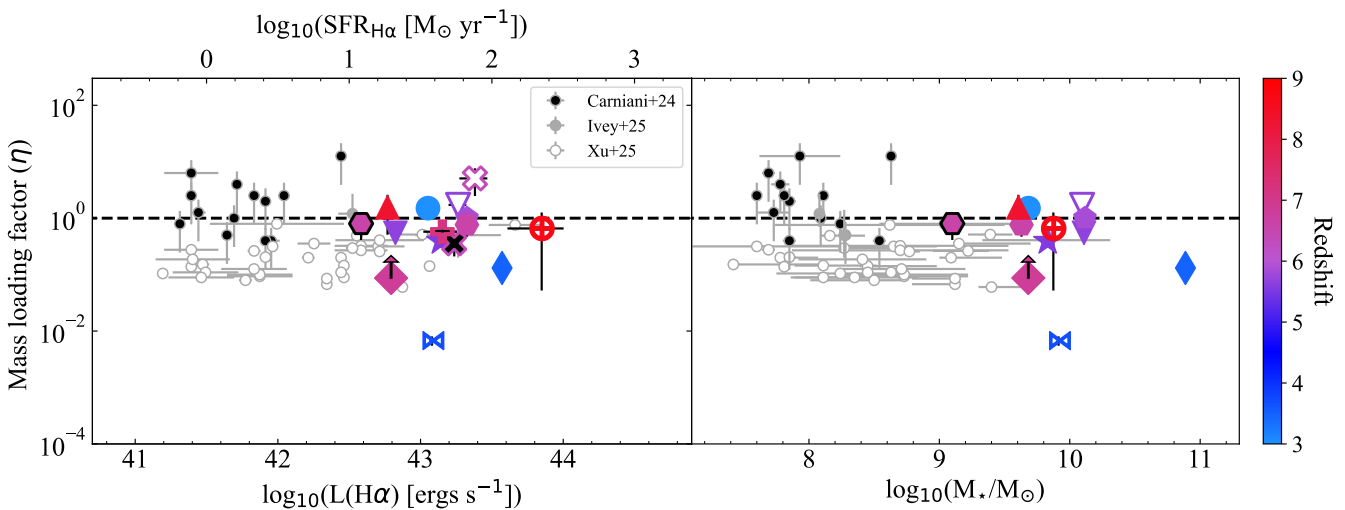


Fig. 7: Mass loading factor ( $\eta$ ) of the outflows in our sample as a function of  $SFR_{H\alpha}$  ( $L_{H\alpha}$ ; left) and stellar mass,  $M_*$ , of the host galaxy (right). Symbols are the same as in Fig. 6. For comparison, we show the sample of star forming galaxies with outflows at  $3 < z < 9$  from Carniani et al. (2024), Xu et al. (2025) and Ivey et al. (2025).

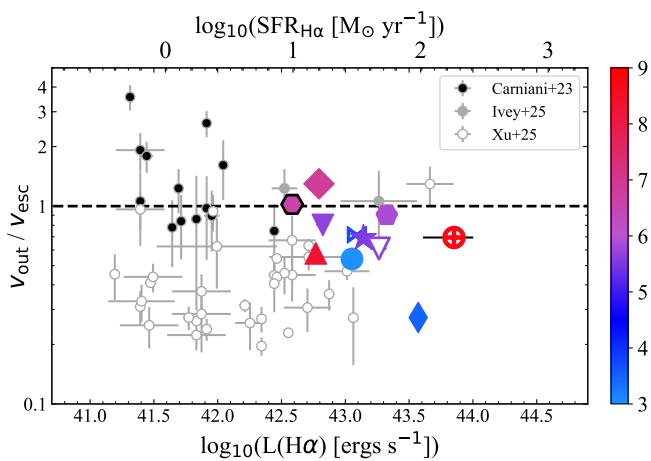


Fig. 8: Ratio between the outflow velocity ( $v_{\text{out}}$ ) and the  $v_{\text{esc}}$  as a function of  $SFR_{H\alpha}$  ( $L_{H\alpha}$ ).

In Fig. 7 we show the estimated values of  $\eta$  for our sample of outflows as a function of  $SFR$  and  $M_*$ , including also results from previous works (Carniani et al. 2024; Xu et al. 2025). The generally low values of  $\eta$  found in our sample of outflows agree quite well with the values from Xu et al. (2025), even though our sample is characterized by more luminous and massive hosts. On the contrary, the values measured in Carniani et al. (2024) are significantly higher, with a large fraction of their outflows displaying  $\eta > 1$ . We ascribe these discrepancies to the lower electron densities adopted in Carniani et al. (2024) and to the fact that their definition of  $v_{\text{out}}$  ( $\Delta V + 2\sigma_{\text{out}}$  instead of  $\Delta V + FWHM_{\text{out}}/2$ ) assumes faster velocities of the outflowing gas, both leading to higher values of  $\eta$ . Finally, although our results suggest that the starburst-driven outflows do not have a strong impact in the SF activity of the hosts, we have to bear in mind that these estimates only account for the impact of the ionized, and the actual impact might be larger if the neutral and molecular phases are considered.

## 7.2.2. Dust and metal redistribution through galactic outflows

The analysis presented in Section 6.2.2 and shown in Figure 5 confirms a result that was already glimpsed in works on individual galaxies from our sample (Lamperti et al. 2024; Rodríguez Del Pino et al. 2024; Parlanti et al. 2025), but now has been established analyzing a large sample: in high-redshift ( $3 < z < 9$ ) star-forming galaxies, outflowing gas has generally higher dust attenuation and oxygen abundances than the gas in the host galaxies. The higher dust attenuation is observed in 8 out of 11 outflows, while a higher or roughly equal metallicity to the host is found in all 7 outflows that could be evaluated. Interestingly, in a recent work, Crespo-Gómez et al. (2025) found two distinct outflows in a galaxy at  $z \sim 6.1$  with a more dust-attenuated outflowing gas, supporting the general behavior we observe in our sample. Metal-enriched outflows have also been found in large samples of local star-forming galaxies (e.g., Rodríguez Del Pino et al. 2019) and their influence has been suggested to contribute to shape the mass-metallicity relation, based on the observed decrease in the metal-loading factor as a function of stellar mass (Chisholm et al. 2018). Although metal-enriched outflows are common in the local Universe, to our knowledge, this is the first time this result is reported in a relatively large sample of galaxies at  $3 < z < 9$ . Finally, the higher metallicity of the gas associated to the broad component emission also confirms the outflowing nature of this component, thus discarding an inflow or merger scenario leading to the broad emission. In the former case, the metallicity of the gas coming from the circumgalactic medium (CGM) is expected to be lower, as it has not been processed by star formation (e.g., Arribas et al. 2024). In the latter, the metallicity is not expected to be systematically high in one of the two components.

We evaluate now whether the dust and metal-enriched outflows in our galaxies could be expelled from their host galaxies and reach the CGM by comparing the maximum velocity of the outflowing gas,  $v_{\text{out}}$ , with the escape velocity,  $v_{\text{esc}}$ , of the galaxy. The estimation of  $v_{\text{esc}}$  can be obtained from the dynamical masses of the galaxies following the method described in Arribas et al. (2014). In our case, since we do not have estimations of the dynamical masses, we assume  $M_{\text{dyn}} =$

$2 \times M_\star$ , based on the values obtained for individual galaxies in our sample (e.g. Rodríguez Del Pino et al. 2024). Then, we estimate the escape velocity at the radius of the outflow,  $r_{\text{out}}$ , for an isothermal sphere truncated at 10 kpc. To estimate whether part of the gas could escape the potential well of their host galaxies, we plot in Figure 8 the ratio between  $v_{\text{out}}$  and  $v_{\text{esc}}$  and explore its variation with SFR. In only one case, COS30, the outflowing gas presents enough velocity to escape the host galaxies and reach the CGM. In the rest of the cases, the outflowing gas remains bound, which is consistent with the low mass loading factor inferred above and further corroborate the idea that such outflows are not powerful enough to alter the host equilibrium by suppressing SF. Instead, they probably redistribute gas throughout the galaxies, potentially contributing to the observed gradients and heterogeneous distribution of dust and metals in high redshift galaxies (e.g. Venturi et al. 2024). In the interpretation of our results, we note that in compact/rotating systems where  $M_{\text{dyn}}$  can exceed  $2 \times M_\star$  we might underestimate  $v_{\text{esc}}$ . However, this would only strengthen our conclusion that the outflows remain bound. These results are in contrast with the detection of metal-enriched gas from [C II] emission extended on physical sizes of  $\sim 20 - 30$  kpc (diameter scale) firstly identified by Fujimoto et al. (2019) in stacking analysis at  $5 < z < 7$  and later confirmed in a larger sample by Ginolfi et al. (2020) at  $4 < z < 6$ .

## 8. Summary and conclusions

In this work we have presented the search and characterization of ionized outflows in a sample of 40 individual galaxies/regions that are part of 15 complex star-forming systems at  $3 < z < 9$  with no evidence of AGN activity. Leveraging JWST/NIRSpec IFU data from the GA-NIFS GTO program we have used the [O III] and H $\alpha$  emission lines as tracers of the ionized gas to search for broad kinematic components that indicate the potential presence of outflowing gas. Our study complements previous works on ionized outflows at  $3 < z < 9$  by probing more luminous and massive systems, allowing us to perform a comprehensive census of galactic outflows within a wide range of SFRs ( $\log_{10}(SFR_{\text{H}\alpha}/M_\odot \text{yr}^{-1}) = [-0.11, 2.5]$ ) and stellar masses ( $\log_{10}(M_\star/M_\odot) = 7.5 - 11$ ). We have constrained the regions hosting the ionized outflows and use their integrated information to derive the kinematics of the outflowing gas as well as its dust attenuation and oxygen abundance. In addition, we have evaluated whether the detected outflows might contribute to the suppression of star formation in the host galaxies and/or expel gas out to the CGM. The main findings of these analyses are:

- We have identified outflows in 13 out of 15 star-forming systems. In terms of the individual galaxies/regions explored, we find outflows in 14 out of 40 of them, which translates into an outflow incidence of 35%. We ascribe this high prevalence of ionized outflows, which is larger than in previous works at similar redshifts, mainly due to the higher stellar masses ( $\log_{10}(M_\star/M_\odot) > 8.5$ ) and SFRs ( $\log_{10}(SFR_{\text{H}\alpha}/M_\odot \text{yr}^{-1}) = [-0.3, 2.5]$ ) of our galaxies, and the advantages provided by our deep IFS data to identify galactic outflows.
- The outflowing gas presents, on average,  $\sim 0.59$  mag higher dust attenuation and  $\sim 0.13$  dex higher oxygen abundances than the host galaxies, indicating that outflows entrain significant amounts of dust and metals. However, the velocities are not large enough ( $v_{\text{out}}/v_{\text{esc}} < 1$ ) for

the outflowing gas to escape the host galaxies and reach the CGM, so instead they probably redistribute the gas throughout the galaxies.

- The outflows identified in this study present velocity dispersions within  $\sigma_{\text{out}} = 140 - 340$  km/s, similar to those measured in less luminous and massive star-forming galaxies in previous works. We identify a statistically significant trend of increasing  $v_{\text{out}}$  as a function of SFR across the wide range covered by this and previous samples of star-forming galaxies at  $3 < z < 9$ .
- The majority of the ionized outflows we detect (10/14) do not seem to have a relevant impact on the star formation activity, based on the values obtained for the mass-loading factor ( $\eta < 1$ ). Comparison with previous works indicates that, considering similar assumptions in electron densities and the same definition of the outflow velocity as in our work, starburst-driven outflows have a limited impact in the SF activity of the hosts within a wide range of SFRs ( $\log_{10}(SFR_{\text{H}\alpha}/M_\odot \text{yr}^{-1}) = [-0.11, 2.5]$ ) and stellar masses ( $\log_{10}(M_\star/M_\odot) = 7.5 - 11$ ).

This work represents the first spatially resolved study of star-formation driven galactic outflows in a relatively large sample of galaxies at  $3 < z < 9$  and provides a detailed characterization of their properties and impact on the host galaxies. Our results suggest that massive galaxies at high redshift are potential hosts of ionized outflows that might not have a significant impact suppressing star formation or expelling gas to the CGM, but could potentially redistribute metals and dust throughout galaxies. Given that this work has focused only on the ionized phase of the gas, a more complete picture would be provided by the study of the neutral and molecular phases.

**Acknowledgements.** We would like to acknowledge the whole JWST mission and the instrument science teams for a successful launch and commissioning of the observatory. BRP, SA, MP acknowledge support from the research projects PID2021-127718NB-I00, PID2024-159902NA-I00, PID2024-158856NA-I00, and RYC2023-044853-I of the Spanish Ministry of Science and Innovation/State Agency of Research (MCIN/AEI/10.13039/501100011033), FSE+, and by “ERDF A way of making Europe”. IL acknowledges support from PRIN-MUR project “PROMETEUS” financed by the European Union - Next Generation EU, Mission 4 Component 1 CUP B53D23004750006. AJB acknowledges funding from the “First Galaxies” Advanced Grant from the European Research Council (ERC) under the European Union’s Horizon 2020 research and innovation programme (Grant agreement No. 789056). SC, GV and SZ acknowledge support by European Union’s HE ERC Starting Grant No. 101040227 - WINGS. MP, GC and EB acknowledge the support of the INAF Large Grant 2022 “The metal circle: a new sharp view of the baryon cycle up to Cosmic Dawn with the latest generation IFU facilities”. GC and EB also acknowledge the INAF GO grant “A JWST/MIRI MIRACLE: Mid-IR Activity of Circumnuclear Line Emission”. EB acknowledges funding through the INAF “Ricerca Fondamentale 2024” programme (mini-grant 1.05.24.07.01). HÜ acknowledges funding by the European Union (ERC APEX, 101164796). Views and opinions expressed are however those of the authors only and do not necessarily reflect those of the European Union or the European Research Council Executive Agency. Neither the European Union nor the granting authority can be held responsible for them. FDE, RM, GCJ, and JS acknowledge support by the Science and Technology Facilities Council (STFC), by the ERC through Advanced Grant 695671 “QUEENCH”, and by the UKRI Frontier Research grant RISEandFALL. This work is based on observations made with the NASA/ESA/CSA James Webb Space Telescope. The data were obtained from the Mikulski Archive for Space Telescopes at the Space Telescope Science Institute, which is operated by the Association of Universities for Research in Astronomy, Inc., under NASA contract NAS 5-03127 for JWST.

## References

Álvarez-Márquez, J., Colina, L., Crespo Gómez, A., et al. 2024, *Astronomy and Astrophysics*, 686, A85  
 Arribas, S., Colina, L., Bellocchi, E., Maiolino, R., & Villar-Martín, M. 2014, *Astronomy and Astrophysics*, 568, A14

Arribas, S., Perna, M., Rodríguez Del Pino, B., et al. 2024, *Astronomy and Astrophysics*, 688, A146

Avery, C. R., Wuyts, S., Förster Schreiber, N. M., et al. 2021, *Monthly Notices of the Royal Astronomical Society*, 503, 5134

Bakx, T. J. L. C., Tamura, Y., Hashimoto, T., et al. 2020, *Monthly Notices of the Royal Astronomical Society*, 493, 4294

Baldwin, J. A., Phillips, M. M., & Terlevich, R. 1981, *Publications of the Astronomical Society of the Pacific*, 93, 5

Belllocchi, E., Arribas, S., Colina, L., & Miralles-Caballero, D. 2013, *Astronomy and Astrophysics*, 557, A59

Bertola, E., Cresci, G., Venturi, G., et al. 2025, *Astronomy and Astrophysics*, 699, A220

Birkin, J. E., Spilker, J. S., Herrera-Camus, R., et al. 2025, *ApJ*, 985, 243

Böker, T., Arribas, S., Lützgendorf, N., et al. 2022, *Astronomy and Astrophysics*, 661, A82

Brusa, M., Bongiorno, A., Cresci, G., et al. 2015, *Monthly Notices of the Royal Astronomical Society*, 446, 2394

Bruzual, G. & Charlot, S. 2003, *Monthly Notices of the Royal Astronomical Society*, 344, 1000

Bunker, A. J., Cameron, A. J., Curtis-Lake, E., et al. 2024, *Astronomy and Astrophysics*, 690, A288

Calzetti, D., Armus, L., Bohlin, R. C., et al. 2000, *The Astrophysical Journal*, 533, 682

Cameron, A. J., Saxena, A., Bunker, A. J., et al. 2023, *Astronomy and Astrophysics*, 677, A115

Capak, P. L., Carilli, C., Jones, G., et al. 2015, *Nature*, 522, 455

Carnall, A. C., Leja, J., Johnson, B. D., et al. 2019, *The Astrophysical Journal*, 873, 44

Carniani, S., Venturi, G., Parlanti, E., et al. 2024, *A&A*, 685, A99

Chabrier, G. 2003, *Publications of the Astronomical Society of the Pacific*, 115, 763

Chisholm, J., Tremonti, C., & Leitherer, C. 2018, *Monthly Notices of the Royal Astronomical Society*, 481, 1690

Cicone, C., Maiolino, R., & Marconi, A. 2016, *Astronomy and Astrophysics*, 588, A41

Clarke, L., Shapley, A. E., Sanders, R. L., et al. 2024, *The Astrophysical Journal*, 977, 133

Concas, A., Maiolino, R., Curti, M., et al. 2022, *Monthly Notices of the Royal Astronomical Society*, 513, 2535

Cooper, R. A., Caputi, K. I., Iani, E., et al. 2025, High-Velocity Outflows in [OIII] Emitters at  $Z=2.5\text{--}9$  from JWST NIRSpec Medium-Resolution Spectroscopy

Crespo Gómez, A., Piqueras López, J., Arribas, S., et al. 2021, *Astronomy and Astrophysics*, 650, A149

Crespo-Gómez, A., Tamura, Y., Colina, L., et al. 2025, RIOJA. Dusty Outflows and Density-Complex ISM in the N-enhanced Lensed Galaxy RXCJ2248-ID at  $Z=6.1$

Davies, R. L., Schreiber, N. M. F., Übler, H., et al. 2019, *ApJ*, 873, 122

D'Eugenio, F., Perez-Gonzalez, P., Maiolino, R., et al. 2023

Domínguez, A., Siana, B., Henry, A. L., et al. 2013, *The Astrophysical Journal*, 763, 145

Feltre, A., Charlot, S., & Gutkin, J. 2016, *Mon Not R Astron Soc*, 456, 3354

Finkelstein, S. L., Bagley, M. B., Arrabal Haro, P., et al. 2025, *ApJL*, 983, L4

Foreman-Mackey, D., Hogg, D. W., Lang, D., & Goodman, J. 2013, *Publications of the Astronomical Society of the Pacific*, 125, 306

Förster Schreiber, N. M., Übler, H., Davies, R. L., et al. 2019, *The Astrophysical Journal*, 875, 21

Franck, J. R. & McGaugh, S. S. 2016, *The Astrophysical Journal*, 817, 158

Freeman, W. R., Siana, B., Kriek, M., et al. 2019, *ApJ*, 873, 102

Fujimoto, S., Ouchi, M., Ferrara, A., et al. 2019, *The Astrophysical Journal*, 887, 107

Genzel, R., Newman, S., Jones, T., et al. 2011, *The Astrophysical Journal*, 733, 101

Ginolfi, M., Jones, G. C., Béthermin, M., et al. 2020, *Astronomy and Astrophysics*, 633, A90

González-Alfonso, E., Fischer, J., Spoon, H. W. W., et al. 2017, *ApJ*, 836, 11

Grogan, N. A., Kocevski, D. D., Faber, S. M., et al. 2011, *The Astrophysical Journal Supplement Series*, 197, 35

Gupta, A., Tran, K.-V., Mendel, T., et al. 2023, *Monthly Notices of the Royal Astronomical Society*, 519, 980

Harrison, C. M., Alexander, D. M., Mullaney, J. R., & Swinbank, A. M. 2014, *Monthly Notices of the Royal Astronomical Society*, 441, 3306

Hashimoto, T., Laporte, N., Mawatari, K., et al. 2018, *Nature*, 557, 392

Herrera-Camus, R., Förster Schreiber, N., Genzel, R., et al. 2021, *Astronomy and Astrophysics*, 649, A31

Ho, I.-T., Kewley, L. J., Dopita, M. A., et al. 2014, *Monthly Notices of the Royal Astronomical Society*, 444, 3894

Isobe, Y., Ouchi, M., Nakajima, K., et al. 2023, *The Astrophysical Journal*, 956, 139

Ivey, L. R., Scholtz, J., Danhaive, A. L., et al. 2025, Exploring Spatially-Resolved Metallicities, Dynamics and Outflows in Low-Mass Galaxies at  $z \sim 7.6$

Jakobsen, P., Ferruit, P., Alves de Oliveira, C., et al. 2022, *Astronomy and Astrophysics*, 661, A80

Jones, G. C., Bowler, R., Bunker, A. J., et al. 2024a, GA-NIFS: Interstellar Medium Properties and Tidal Interactions in the Evolved Massive Merging System B14-65666 at  $z = 7.152$

Jones, G. C., Bunker, A. J., Telikova, K., et al. 2025, *Monthly Notices of the Royal Astronomical Society*, 540, 3311

Jones, G. C., Übler, H., Perna, M., et al. 2024b, *Astronomy and Astrophysics*, 682, A122

Jones, G. C., Vergani, D., Romano, M., et al. 2021, *Monthly Notices of the Royal Astronomical Society*, 507, 3540

Kakkad, D., Mainieri, V., Vietri, G., et al. 2020, *Astronomy and Astrophysics*, 642, A147

Kauffmann, G., Heckman, T. M., Tremonti, C., et al. 2003, *Monthly Notices of the Royal Astronomical Society*, 346, 1055

Kawamata, R., Oguri, M., Ishigaki, M., Shimasaku, K., & Ouchi, M. 2016, *ApJ*, 819, 114

Kewley, L. J., Dopita, M. A., Sutherland, R. S., Heisler, C. A., & Trevena, J. 2001, *ApJ*, 556, 121

Koekemoer, A. M., Faber, S. M., Ferguson, H. C., et al. 2011, *The Astrophysical Journal Supplement Series*, 197, 36

Lamperti, I., Arribas, S., Perna, M., et al. 2024, *Astronomy and Astrophysics*, 691, A153

Laporte, N., Streblyanska, A., Kim, S., et al. 2015, *Astronomy and Astrophysics*, 575, A92

Larson, R. L., Finkelstein, S. L., Kocevski, D. D., et al. 2023, *The Astrophysical Journal Letters*, Volume 953, Issue 2, id.L29, <NUMPAGES>26</NUMPAGES> pp., 953, L29

Liu, W., Fan, X., Yang, J., et al. 2024, *The Astrophysical Journal*, 976, 33

Llerena, M., Amorín, R., Pentericci, L., et al. 2023, *Astronomy and Astrophysics*, 676, A53

Loiacono, F., Decarli, R., Mignoli, M., et al. 2024, *Astronomy and Astrophysics*, 685, A121

Lutz, D., Sturm, E., Janssen, A., et al. 2020, *A&A*, 633, A134

Ma, Z., Sun, B., Cheng, C., et al. 2024, *The Astrophysical Journal*, 975, 87

Maiolino, R., Gallerani, S., Neri, R., et al. 2012, *Mon Not R Astron Soc Lett*, 425, L66

Mallery, R. P., Mobasher, B., Capak, P., et al. 2012, *The Astrophysical Journal*, 760, 128

Marconcini, C., D'Eugenio, F., Maiolino, R., et al. 2025, *Astronomy and Astrophysics*, 699, A154

Marconcini, C., D'Eugenio, F., Maiolino, R., et al. 2024, *Monthly Notices of the Royal Astronomical Society*, 533, 2488

Marrone, D. P., Spilker, J. S., Hayward, C. C., et al. 2018, *Nature*, 553, 51

Marshall, M. A., Perna, M., Willott, C. J., et al. 2023a, *Astronomy and Astrophysics*, 678, A191

Marshall, M. A., Perna, M., Willott, C. J., et al. 2023b, *Black Hole and Host Galaxy Properties of Two  $Z \sim 6.8$  Quasars from the NIRSpec IFU*

Marshall, M. A., Yue, M., Eilers, A.-C., et al. 2025, *Astronomy and Astrophysics*, 702, A50

Maseda, M. V., de Graaff, A., Franx, M., et al. 2024, *Astronomy and Astrophysics*, 689, A73

Matthee, J., Sobral, D., Santos, S., et al. 2015, *Monthly Notices of the Royal Astronomical Society*, 451, 400

Mazzolari, G., Übler, H., Maiolino, R., et al. 2024, *Astronomy and Astrophysics*, 691, A345

McLure, R. J., Pentericci, L., Cimatti, A., et al. 2018, *Monthly Notices of the Royal Astronomical Society*, 479, 25

Newman, S. F., Genzel, R., Förster-Schreiber, N. M., et al. 2012, *ApJ*, 761, 43

Osterbrock, D. E. & Ferland, G. J. 2006, *Astrophysics of Gaseous Nebulae and Active Galactic Nuclei*

Parlanti, E., Carniani, S., Übler, H., et al. 2024, *Astronomy and Astrophysics*, 684, A24

Parlanti, E., Carniani, S., Venturi, G., et al. 2025, *Astronomy and Astrophysics*, 695, A6

Pentericci, L., McLure, R. J., Garilli, B., et al. 2018a, *Astronomy and Astrophysics*, 616, A174

Pentericci, L., Vanzella, E., Castellano, M., et al. 2018b, *A&A*, 619, A147

Pérez-González, P. G., D'Eugenio, F., Rodríguez del Pino, B., et al. 2025, *Nature Astronomy*, 9, 1240

Perna, M., Arribas, S., Colina, L., et al. 2022, *Astronomy and Astrophysics*, 662, A94

Perna, M., Arribas, S., Ji, X., et al. 2024, GA-NIFS: A Galaxy-Wide Outflow in a Compton-thick Mini-BAL Quasar at  $z = 3.5$  Probed in Emission and Absorption

Perna, M., Arribas, S., Lamperti, I., et al. 2025, *Astronomy and Astrophysics*, 696, A59

Perna, M., Arribas, S., Marshall, M., et al. 2023, *Astronomy and Astrophysics*, 679, A89

Perna, M., Lanzuisi, G., Brusa, M., Mignoli, M., & Cresci, G. 2017, arXiv:1703.05335 [astro-ph] [arXiv:1703.05335]

Prieto-Jiménez, C., Álvarez-Márquez, J., Colina, L., et al. 2025, *Astronomy and Astrophysics*, 701, A31

Riechers, D. A., Bradford, C. M., Clements, D. L., et al. 2013, *Nature*, 496, 329

Rigby, J., Perrin, M., McElwain, M., et al. 2023, *Publications of the Astronomical Society of the Pacific*, 135, 048001

Roberts-Borsani, G. W., Bouwens, R. J., Oesch, P. A., et al. 2016, *ApJ*, 823, 143

Rodríguez Del Pino, B., Arribas, S., Piñeras López, J., Villar-Martín, M., & Colina, L. 2019, *Monthly Notices of the Royal Astronomical Society*, 486, 344

Rodríguez Del Pino, B., Perna, M., Arribas, S., et al. 2024, *A&A*, 684, A187

Rupke, D. S. N. 2018

Sanders, R. L., Shapley, A. E., Kriek, M., et al. 2016, *The Astrophysical Journal*, 816, 23

Sanders, R. L., Shapley, A. E., Topping, M. W., et al. 2025, *The AURORA Survey: High-Redshift Empirical Metallicity Calibrations from Electron Temperature Measurements at Z=2-10*

Saxena, A., Pentericci, L., Mirabelli, M., et al. 2020, *A&A*, 636, A47

Scholtz, J., Curti, M., D'Eugenio, F., et al. 2025a, *Monthly Notices of the Royal Astronomical Society*, 539, 2463

Scholtz, J., Maiolino, R., D'Eugenio, F., et al. 2025b, *A&A*, 697, A175

Schwarz, G. 1978, *The Annals of Statistics*, 6, 461

Scoville, N., Abraham, R. G., Aussel, H., et al. 2007a, *The Astrophysical Journal Supplement Series*, 172, 38

Scoville, N., Aussel, H., Brusa, M., et al. 2007b, *ApJS*, 172, 1

Smit, R., Bouwens, R. J., Carniani, S., et al. 2018, *Nature*, 553, 178

Stiavelli, M., Morishita, T., Chiaberge, M., et al. 2023, *The Astrophysical Journal*, 957, L18

Sugahara, Y., Álvarez-Márquez, J., Hashimoto, T., et al. 2025, *The Astrophysical Journal*, 981, 135

Suh, H., Scharwächter, J., Farina, E. P., et al. 2025, *Nature Astronomy*, 9, 271

Swinbank, A. M., Harrison, C. M., Tiley, A. L., et al. 2019, *Monthly Notices of the Royal Astronomical Society*, 487, 381

Tamura, Y., Mawatari, K., Hashimoto, T., et al. 2019, *ApJ*, 874, 27

Temple, M. J., Banerji, M., Hewett, P. C., et al. 2019, *Monthly Notices of the Royal Astronomical Society*, 487, 2594

Tozzi, G., Cresci, G., Perna, M., et al. 2024, *Astronomy and Astrophysics*, 690, A141

Trefoloni, B., Carniani, S., Bertola, E., et al. 2025, *GA-NIFS: An Extended [OIII] Halo around the Sub-Eddington Quasar J1342+0928 at Z=7.54*

Übler, H., D'Eugenio, F., Perna, M., et al. 2024a, *Monthly Notices of the Royal Astronomical Society*, 533, 4287

Übler, H., Maiolino, R., Curtis-Lake, E., et al. 2023, *Astronomy and Astrophysics*, 677, A145

Übler, H., Maiolino, R., Pérez-González, P. G., et al. 2024b, *Monthly Notices of the Royal Astronomical Society*, 531, 355

van Dokkum, P. G. 2001, *PASP*, 113, 1420

Veilleux, S., Maiolino, R., Bolatto, A. D., & Aalto, S. 2020, *Astron Astrophys Rev*, 28, 2

Veilleux, S. & Osterbrock, D. E. 1987, *The Astrophysical Journal Supplement Series*, 63, 295

Venturi, G., Carniani, S., Bertola, E., et al. 2025, *GA-NIFS: Powerful and Frequent Outflows in Moderate-Luminosity AGN at Zsim3-6\$*

Venturi, G., Carniani, S., Parlanti, E., et al. 2024, *Astronomy and Astrophysics*, 691, A19

Villar Martín, M., Emonts, B., Humphrey, A., Cabrera Lavers, A., & Binette, L. 2014, *Monthly Notices of the Royal Astronomical Society*, 440, 3202

Willott, C. J., McLure, R. J., Hibon, P., et al. 2013, *The Astronomical Journal*, 145, 4

Xu, Y., Ouchi, M., Nakajima, K., et al. 2025, *The Astrophysical Journal*, 984, 182

Zamora, S., Carniani, S., Bertola, E., et al. 2025a, *GA-NIFS: Understanding the Ionization Nature of EGSY8p7/CEERS-1019. Evidence for a Star Formation-Driven Outflow at z = 8.6*

Zamora, S., Venturi, G., Carniani, S., et al. 2025b, *Astronomy and Astrophysics*, 702, A102

Zhang, Y., Ouchi, M., Nakajima, K., et al. 2024, *The Astrophysical Journal*, 970, 19

Zhu, Y., Rieke, M. J., Ji, Z., et al. 2025, *ApJ*, 986, 162

Zitrin, A., Labbe, I., Belli, S., et al. 2015, *The Astrophysical Journal*, 810, L12

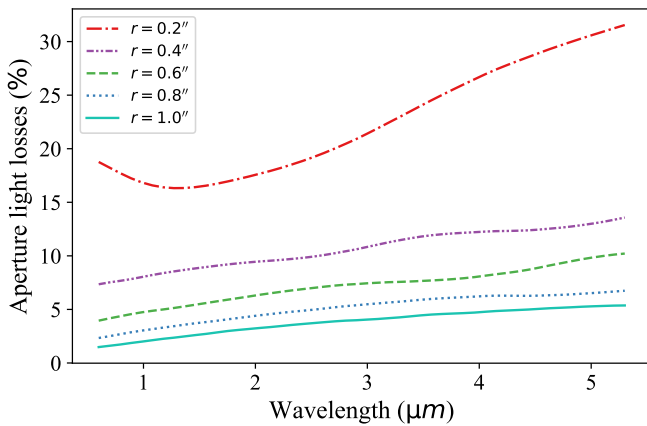


Fig. A.1: Light losses associated with the extraction of fluxes from a simulated data cube of the NIRSpec PSF in IFS mode, using circular apertures with different radii (see Appendix A).

## A: Aperture corrections

In the extraction of integrated fluxes from the data cubes (Sections 4 and 5) we apply a correction for the light losses outside the adopted apertures caused by the NIRSpec PSF. To compute these losses, we start by generating a data cube containing the simulated PSF of the NIRSpec IFS mode using the STPSF<sup>3</sup> Python package. At this stage we work with a data cube generated in the R100 mode, which allows to compute the losses across the entire wavelength range of NIRSpec and provides exactly the same results as the data cubes of individual filter/grating configurations in medium and high resolution modes. We perform a spectral binning of the PSF data cube in windows of 50 pixels and compute the fraction of the total light contained within each aperture. Corrections are estimated as the inverse of this fraction and are obtained at each wavelength through interpolation. As an example, in Figure A.1 we show the light losses as a function of wavelength corresponding to circular apertures with varying radius from  $0.2''$  to  $0.1''$ . For small apertures,  $r \leq 0.2''$  the light losses become significant, reaching  $20 - 30\%$  of the total light, while at larger apertures ( $r \geq 0.6''$ ) losses are always lower than  $10\%$ . These results are comparable to those reported by Zamora et al. (2025b, Fig. B.1) using a QSO to model the PSF of NIRSpec.

## B: Identification of outflows in individual systems

### B.1: GS-23170

This object is included in the VANDELS survey (McLure et al. 2018, Pentericci et al. 2018a) and studied by Saxena et al. (2020), who identified it as a bright and "narrow" (FWHM  $\sim 450$  km/s) He II  $\lambda 1640$  emitter. The presence of an AGN was excluded on the basis of the missing C IV and X-ray emission.

The present NIRSpec-IFS data reveal that [O III]  $\lambda 5007$  emission from this galaxy is characterized by the presence of two bright cores (23170-N and 23170-S) within a projected distance of  $\sim 2 - 3$  kpc. The emission in the northern core is well modeled with two kinematic components, with  $\sigma_{\text{broad}} > 150$  km/s within a radius of  $\sim 1.5$  kpc around the peak in the continuum emission, consistent with an outflow scenario. The southern core also presents two kinematic components, although in this case their

velocity dispersions are low ( $\sigma < 100$  km/s), suggesting the overlap along the line of sight of two kinematically distinct structures (e.g., a clump and the extended disc of component N). More to the south there is another region with high velocity dispersion, although in this case only one kinematic component is needed to model the data. Since this region is not directly connected to the outflow at the north, and its continuum emission is weak, we associate its turbulence to a tidal tail or interaction rather than to an outflow.

### B.2: GS-5001

The GS-5001 system lies within the central regions of a large-scale overdensity of galaxies that has been classified as a candidate protocluster (Franck & McGaugh 2016).

The central and brightest source (hereafter 5001-C) and its close environment have been recently studied by means of NIRSpec-IFS data by Lamperti et al. (2024). These observations cover a region of about 20 kpc, which, in addition of 5001-C, also includes two other close companions at similar redshifts, GS-4923 (we refer to it as 5001-S) and 5001-N, as well as several substructures revealing clear signs of interactions<sup>4</sup>. In their study, Lamperti et al. (2024) already identified a spatially resolved ionized bi-conical outflow with an extension of  $\sim 3$  kpc along the minor axis of the central galaxy of this system (see their Figure 6). Similarly to their results, we find a region with enhanced velocity dispersion extending to the East and West from the central regions of 5001-C, reaching values of up to 300 km/s, thus consistent with an outflow. We do not find clear evidence for outflows in 5001-S nor in 5001-N.

### B.3: GS- 4891

By means of NIRSpec-IFS data, this system was studied in detail by Rodríguez Del Pino et al. (2024), who found a spatially resolved outflow extending up to a distance of  $\sim 1.5$  kpc from the central parts of the main galaxy (hereafter 4891-C). In our analysis, we also identify this extended emission along the Southeast – Northwest direction, slightly smaller than in the previous work (1.05 kpc vs 1.2 kpc) due to the different criteria applied to identify outflows. Nevertheless, the overall properties of the outflow are very similar in both works. Rodríguez Del Pino et al. (2024) also find in the FoV two companions galaxies at a redshift similar to 4891-C, 4891-N and GS-28356 (we refer to it as 4891-E), but none of these galaxies has traces of outflowing gas.

### B.4: HZ4

HZ4 is a complex star forming system, with an extensive set of multi-wavelength pre-JWST data sets including HST (Scoville et al. 2007a), Keck (Mallery et al. 2012), and ALMA (Capak et al. 2015, Herrera-Camus et al. 2021, Jones et al. 2021). The recently analyzed NIRSpec - IFS data (Parlanti et al. 2025) have revealed three close merging galaxies/structures in the system, HZ4-N, HZ4-C, and HZ4-S, all within a projected distance of about 4 kpc.

They detect and characterize ionized outflows in HZ4-C and found that it extends over regions of up to 4 kpc with velocity

<sup>4</sup>The FoV also includes GS-4923, but this galaxy has a photometric redshift of about 0.2 according to Rainbow Data Base ([https://arcoirix.cab.inta-csic.es/Rainbow\\_Database/](https://arcoirix.cab.inta-csic.es/Rainbow_Database/)), and therefore it is ignored in the present study.

<sup>3</sup><https://stpsf.readthedocs.io/>

dispersions of  $\sim 200 - 250$  km/s (see their Figure 6), properties that are reproduced in our analysis. HZ4 is also the most distant star forming galaxy presenting evidence for a neutral outflow, traced by the [C II] line measured with ALMA (Herrera-Camus et al. 2021). Parlanti et al. (2025) compared the neutral and ionized outflows, finding that they are partially co-spatial with the former dominating by more than one order of magnitude the total mass outflow rate.

### B.5: HZ10

HZ10 was originally detected as a Lyman break galaxy (LBG) in the 2 square degree Cosmic Evolution Survey (Scoville et al. 2007b) field. Follow-up observations revealed that this source is a UV-luminous Ly $\alpha$  emitter at  $z = 5.659$  with bright far-infrared emission ([C II]) consistent with  $SFR_{\text{IR}} = 169 \text{ M}_{\odot} \text{ yr}^{-1}$  (Capak et al. 2015). Using NIRSpec-IFS data, Jones et al. (2025) have recently studied this complex star forming system and identified three emission-line galaxies within a projected distance of  $\sim 10$  kpc, HZ10\_E, HZ10\_C, and HZ10\_W, likely in a merging pre-coalescence phase. They also identify blue- and red-shifted asymmetries of the order of  $\sim 200$  km/s in the [O III] and H $\alpha$  emission line profiles of the East and West members, that they attributed to the possible presence of an outflow or tidal tails.

In our  $\sigma_{\text{broad}}$  map (Fig. 4), we find that these two regions present the highest velocity dispersion, reaching up to 300 km/s and extensions of  $\sim 2$  and 0.5 kpc, respectively. They emerge from (or are coincident with) the central regions of these components, being then consistent with the expectations from an outflow scenario.

### B.6: COS\_12306

This galaxy was identified as one of the most luminous and extended star forming galaxies at  $z \sim 6$  in the CFHT Legacy Survey (Willott et al. 2013). Being located within the CANDELS field (Grogan et al. 2011; Koekemoer et al. 2011), it also has high-resolution HST/ACS and WFC3 imaging available. With an original photo-z of 6.197, it was later spectroscopically confirmed to be at  $z \sim 5.91$  through the detection of Ly $\alpha$  (Pentericci et al. 2018b), while our observations of the rest-frame optical emission lines provide a lower value,  $z \sim 5.84$ . The system presents a complex morphology in the [O III]  $\lambda 5007$  line emission map with two main components (12306-C, 12306-NW) and several substructures along  $\sim 6$  kpc, possibly all within a merging system. The broad component emission seems associated to the brightest central component and extends to the northeast in a structure that is consistent with a conical outflow along the minor axis of the system.

### B.7: HFLS3

HFLS3 is a complex, lensed star forming system at  $z = 6.3$  with an extreme infrared luminosity of  $2.86 \times 10^{13} \text{ L}_{\odot}$  and a SFR of about  $2900 \text{ M}_{\odot} \text{ yr}^{-1}$  (Riechers et al. 2013). This system has been recently studied in detail with NIRSpec-IFS data by Jones et al. (2024b), who find that instead of a single extreme starburst, the system consists of six star forming galaxies at  $z \sim 6.3$  (c1, c2, w1, w2, s1, and s2) that are lensed by two foreground galaxies: g1 ( $z \sim 3.48$ ) and g2 ( $z \sim 2$ ). Since the spectroscopic setup employed for the R2700 observations (G395H/F290LP) targets the rest-frame optical at  $z \sim 6.3$ , in HFLS3\_g1 the only strong

optical emission line covered is H $\alpha$ , while for HFLS3\_g2 the optical emission falls outside the wavelength coverage.

For the present analysis, we have searched for broad components in all the galaxies within the FoV, finding evidence for the presence of outflows in HFLS3\_g1 through H $\alpha$ , and in HFLS3\_w 1, 2 through [O III]. In particular, for HFLS3\_g1 we detect extended emission of  $\sim 1$  kpc in radius around its center, with  $\sigma_{\text{broad}} = 100 - 150$  km/s. We note that broad emission is detected also in forbidden lines, [N II]  $\lambda 6584$  and [S III]  $\lambda 9532$  (Jones et al. 2024b), confirming the outflow nature of the broad emission. For HFLS3\_w 1, 2, we have identified signatures of outflows in the regions around the peaks of continuum emission.

### B.8: CR7

This complex merging system was first identified by Matthee et al. (2015) as one of the most luminous Ly $\alpha$ -emitters ( $L_{\text{Ly}\alpha} \sim 10^{44} \text{ L}_{\odot}$ ) at  $z > 6$ . It consists of three main companion galaxies (CR7\_A, CR7\_B, CR7\_C) and several substructures, all within a projected distance of  $\sim 8$  kpc. The system has been recently studied using NIRSpec-IFS observations by Marconcini et al. (2025), who have probed the star formation history (SFH) of the three main galaxies and the complex interactions among the different components. They also reported the presence of ionized outflows in two galaxies of the system, CR7\_A and CR7\_B. In our analysis, we obtain similar results. In particular, we identify a broad component extending up to 3 kpc from the emission peak in CR7\_A and values of  $\sigma_{\text{broad}} \sim 150 - 300$  km/s, and a more compact broad region of  $< 1$  kpc and  $\sim 200$  km/s around the continuum maximum of CR7\_B.

### B.9: COS-3018

Scholtz et al. (2025a) have studied this system with NIRSpec-IFS finding that the SFH, the ISM conditions and kinematics, as well as the stellar population properties are better explained by a merging event of three galaxies (C, NE, SE) than by a rotating disc, as initially inferred from lower resolution ALMA observations (Smit et al. 2018). The main galaxy also shows sub-structure with a set of clumps aligned along the E-W direction, as revealed by NIRCam imaging taken as part of the PRIMER survey (PID1837, PI J. Dunlop).

Scholtz et al. (2025a) already reported the need of fitting the emission lines profiles of the main (C) galaxy with two narrow components and a broad component with  $FWHM_{\text{broad}} = 1210 \pm 120$  km/s, that they explained as due to a relatively compact outflow ( $\sim 2.1$  kpc).

To avoid contamination from the NE and SE galaxies, we focus our analysis on a circular aperture with radius  $0.15''$  (0.8 kpc) at the peak of stellar emission in the C galaxy (see Fig. 4). In the two-component modeling of the integrated spectrum of this region we identify a broad component with  $FWHM_{\text{broad}} = 787 \pm 21$  km/s. Although still high, these velocities are lower than those reported by Scholtz et al. (2025a). This difference could be attributed to their use of a larger aperture that includes galaxy C, potentially capturing gas at higher velocities beyond the nuclear regions and to the fact that their spectral modeling includes three kinematic components (two narrow and one broad), which might better account for the high-velocity wings of the emission-line profiles.

Another broad component seems to be in spatial agreement with the position of the NE galaxy. However, the weak continuum emission in this region does not support a

star-formation driven outflow as the cause for the high velocity dispersion, which could instead be produced by the merging of the galaxies.

### B.10: B14

This massive system consists of two main cores with strong  $[\text{O III}] \lambda 5007$  and continuum emission, and other fainter substructures as recently revealed by JWST NIRCam (Sugahara et al. 2025) and NIRSpec-IFS (Jones et al. 2025) observations. Jones et al. (2025) identified the presence of a broad component associated to the integrated spectra of these structures ( $FWHM \sim 550 - 750 \text{ km/s}$ ), as well as an extended broad emission as traced by the  $W80$  index over a region of about 4 kpc along the direction of the two main cores. They interpreted these features as due to tidal effects or the presence of an outflow. Prieto-Jiménez et al. (2025) has recently attempted to identify hints of this broad emission in the  $\text{H}\alpha$  line profile as observed by MIRI, but their analysis did not yield a significant detection.

As in Jones et al. (2025), we detect very extended broad emission beyond the continuum emission and identify regions with red-shifted velocities ( $< -200 \text{ km/s}$ ) around the W nucleus (see Fig. C.12). Based on these properties, we do not consider the presence of a clear outflow in this system, as the broad emission could potentially be a consequence of an ongoing merger or tidal interactions.

### B.11: MACSJ0416-Y1

MACSJ0416-Y1 was first selected as a  $z = 8$  candidate (Laporte et al. 2015) and later on spectroscopically-confirmed at  $z = 8.31$  through the detections of  $[\text{O III}] 88 \mu\text{m}$  (Tamura et al. 2019) and  $[\text{C II}] 157.7 \mu\text{m}$  (Bakx et al. 2020). In a recent study using NIRCam/WFSS data, Ma et al. (2024) estimated high  $SFRs$  ( $\sim 165 \text{ M}_\odot \text{ yr}^{-1}$ ), relatively large dust extinction  $A_V = 0.92 - 1.10 \text{ mag}$  and very young stellar populations ( $< 5 \text{ Myr}$ ).

In our study, we identify a compact ( $r_{\text{out}} = 0.5 \text{ kpc}$ ) ionized outflow in a star-forming region at the East of the system, and  $\sigma_{\text{out}} \sim 200 \text{ km/s}$ .

### B.12: EGSY8P7

This galaxy was initially identified through photometric dropout by Roberts-Borsani et al. (2016,  $z_{\text{phot}} = 8.57^{+0.22}_{-0.43}$ ), and later on confirmed through strong  $\text{Ly}\alpha$  emission ( $z_{\text{spec}} = 8.683^{+0.001}_{-0.004}$ ; Zitrin et al. 2015), making it one of the most distant  $\text{Ly}\alpha$  emitters known to date. Recently, NIRSpec MOS medium-resolution observations revealed a tentative detection of a broad  $\text{H}\beta$  component with  $FWHM \sim 1200 \text{ km/s}$  that was interpreted as evidence of a broad-line AGN by Larson et al. (2023). In a detailed analysis using NIRSpec IFS data, Zamora et al. (2025a) identified a broad component in  $\text{H}\beta$  and  $[\text{O III}] \lambda 5007$  with  $FWHM \sim 650 \text{ km/s}$ , extended over a distance of  $\sim 1 \text{ kpc}$  and consistent with an outflow driven by stellar feedback.

In our study, the ionization in this source does not reveal evidence of AGN activity (see right panels in Fig. 2). We detect an ionized outflow with  $r_{\text{out}} = 1 \text{ kpc}$  and  $\sigma_{\text{out}} = 214.3 \pm 2.6 \text{ km/s}$ , slightly lower velocities than those reported by Zamora et al. (2025a).

### B.13: MACS1149-JD1

MACS1149-JD1 resides behind the MACS J1149.6+2223 cluster and presents a magnification  $\mu = 10 \pm 0.7$  (Hashimoto et al. 2018; Stiavelli et al. 2023; Marconcini et al. 2024). Marconcini et al. (2024) have recently studied this system with NIRSpec IFS data. They identify a region towards the West with a relatively large velocity dispersion and requiring a second broad component. This is spatially coincident with a peak in the SFR density, and suggests the presence of an outflow. Álvarez-Márquez et al. (2024) measured the  $\text{H}\alpha$  kinematics with JWST/MIRI suggesting the hypothesis of outflowing gas powered by the UV-bright clump JD1-S.

Our analysis also supports the presence of a secondary kinematic component towards the West of the system. However, the associated  $\sigma_{\text{broad}} = 68 \text{ km/s}$  is too low to be interpreted as an outflow, and it could be instead a region of overlapping gas between the southern and northern systems.

### B.14: SPT0311-58

ALMA observations of the SPT0311-58 system at  $z \sim 6.9$ , showed that it resides in a massive dark-matter halo and hosts two dusty galaxies (E and W) with a combined  $SFR \sim 3500 \text{ M}_\odot \text{ yr}^{-1}$  (Marrone et al. 2018). Recent NIRSpec-IFS observations have revealed that the system also consists of ten additional smaller galaxies within a region of 17 kpc, representing the core of an extremely massive proto-cluster (Arribas et al. 2024). In this later work, the authors identified a region towards galaxy E that presented an additional kinematic component with a low velocity dispersion ( $\sigma < 100 \text{ km/s}$ ) and redshifted velocities ( $\sim 260 \text{ km/s}$ ) with respect to the systemic. Given the relatively high attenuation ( $A_V = 1.7 - 2.4$ ) found in galaxy E, a possible outflow in which only the redshifted component was visible was deemed unlikely, and instead this secondary component was interpreted as a satellite galaxy moving towards galaxy E in a minor merger.

In our analysis, we also find a secondary kinematic component with redshifted velocities although higher velocity dispersion ( $\sigma = 100 - 250 \text{ km/s}$ ) than those reported by Arribas et al. (2024). Nevertheless, these results confirm that the additional kinematic component is associated to a satellite.

## C: Kinematic maps

In this section we present, for each system in our sample, the maps of line fluxes and kinematics obtained from the emission-line analysis (of  $[\text{O III}] \lambda 5007$  or  $\text{H}\alpha$ ) described in Sec. 3.1. We include maps of integrated line fluxes, velocity and velocity dispersion for the one-component fit (top) and the narrow (middle) and broad (bottom) kinematic components. These maps, in particular the ones displaying the kinematics of the broad component, are used to define the regions hosting ionized outflows, which are highlighted in red, as in Fig. 4.

## D: Spectral modeling of outflow spectra

This section contains the spectral modeling of the integrated spectrum of the outflows identified in our sample of star-forming systems, including the main emission lines identified in each case. When an emission line is better modeled with two kinematic components (see Sec. 5) we show narrow (blue) and broad (red) components, otherwise we only show the one-component model (green).

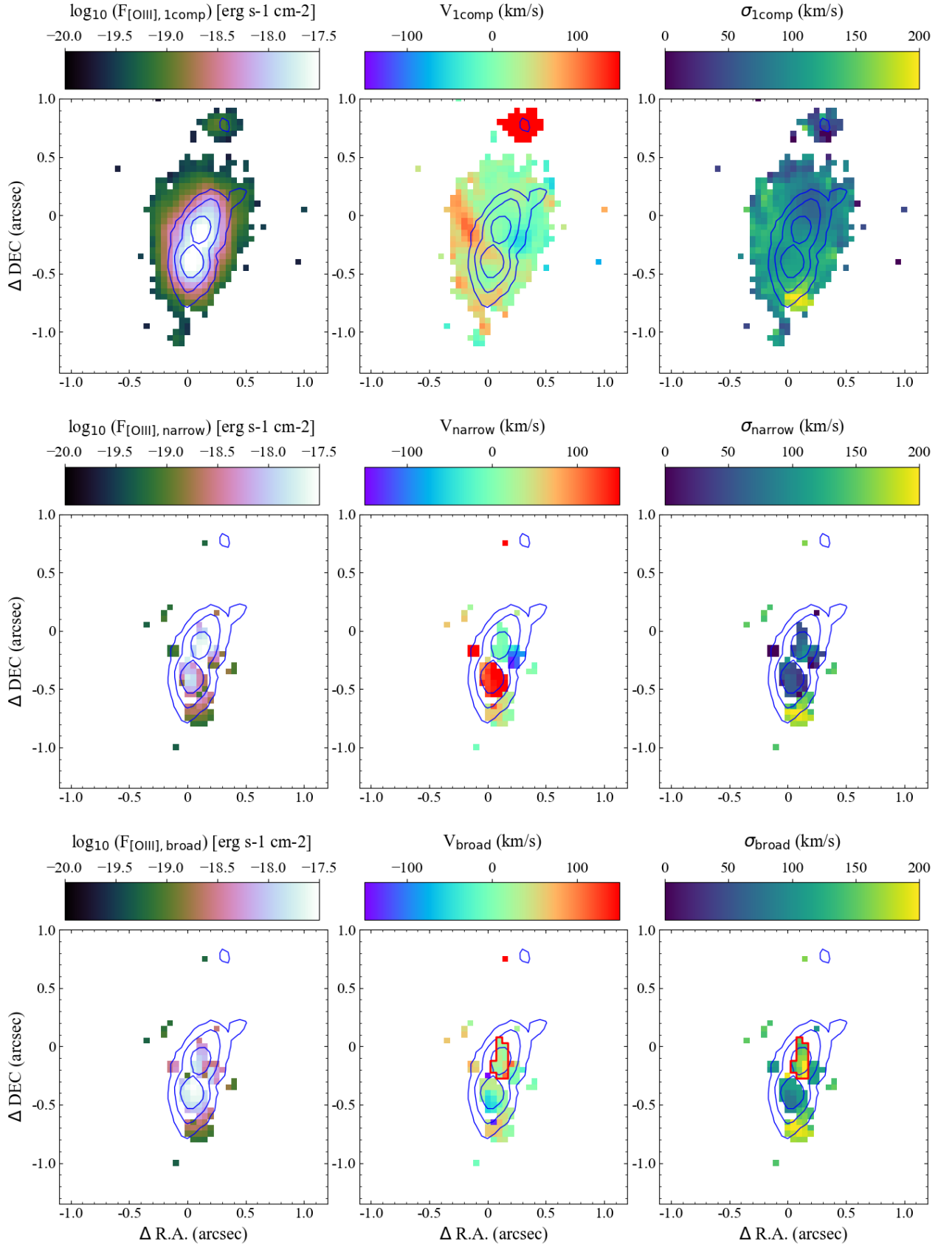


Fig. C.1: Maps of integrated line fluxes, velocity and velocity dispersion for the one-component fit (top), narrow kinematic component (middle) and broad kinematic component (bottom) for 23170. The outflowing region is highlighted in red in the bottom panels.

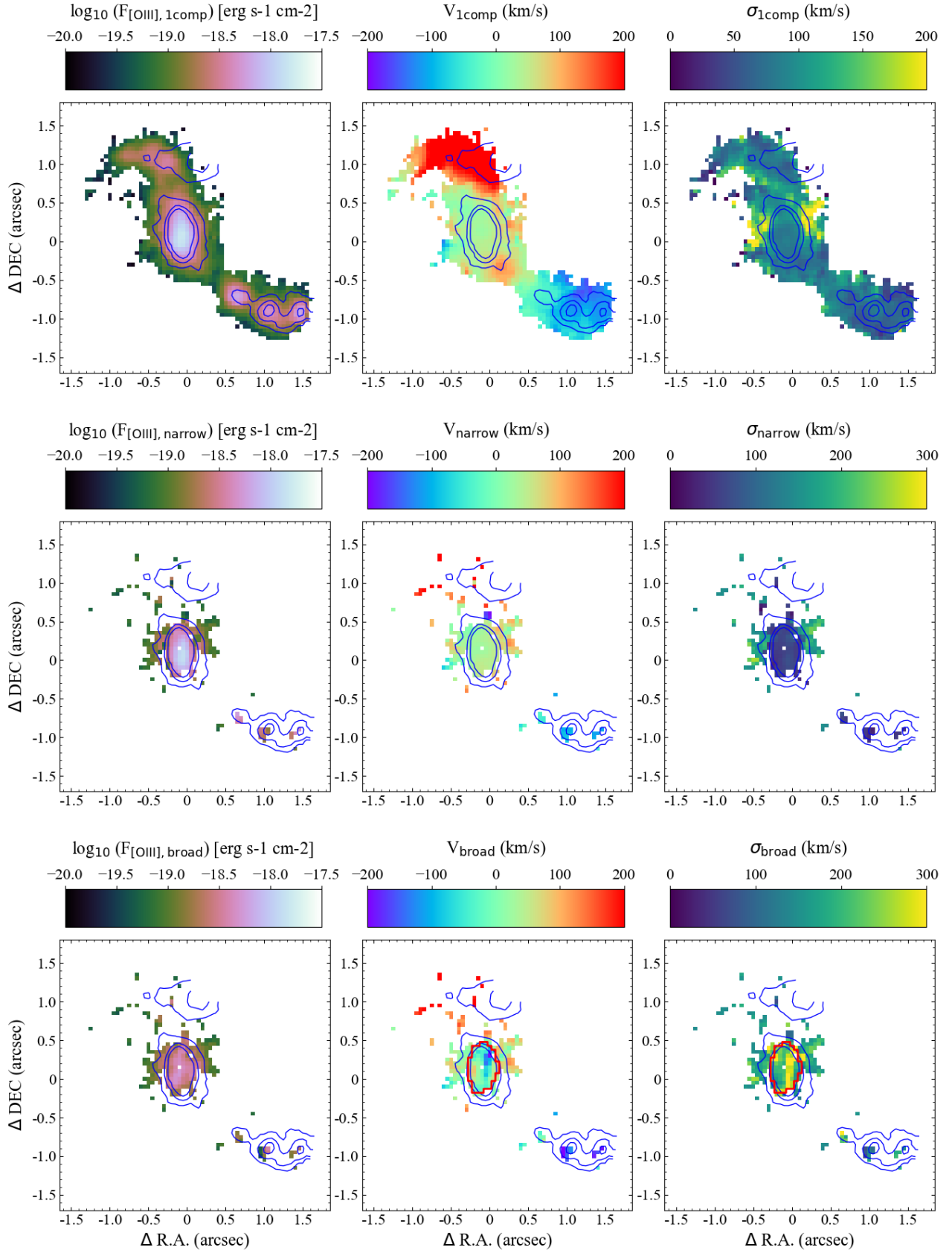


Fig. C.2: Same as Fig. C.1 for 5001.

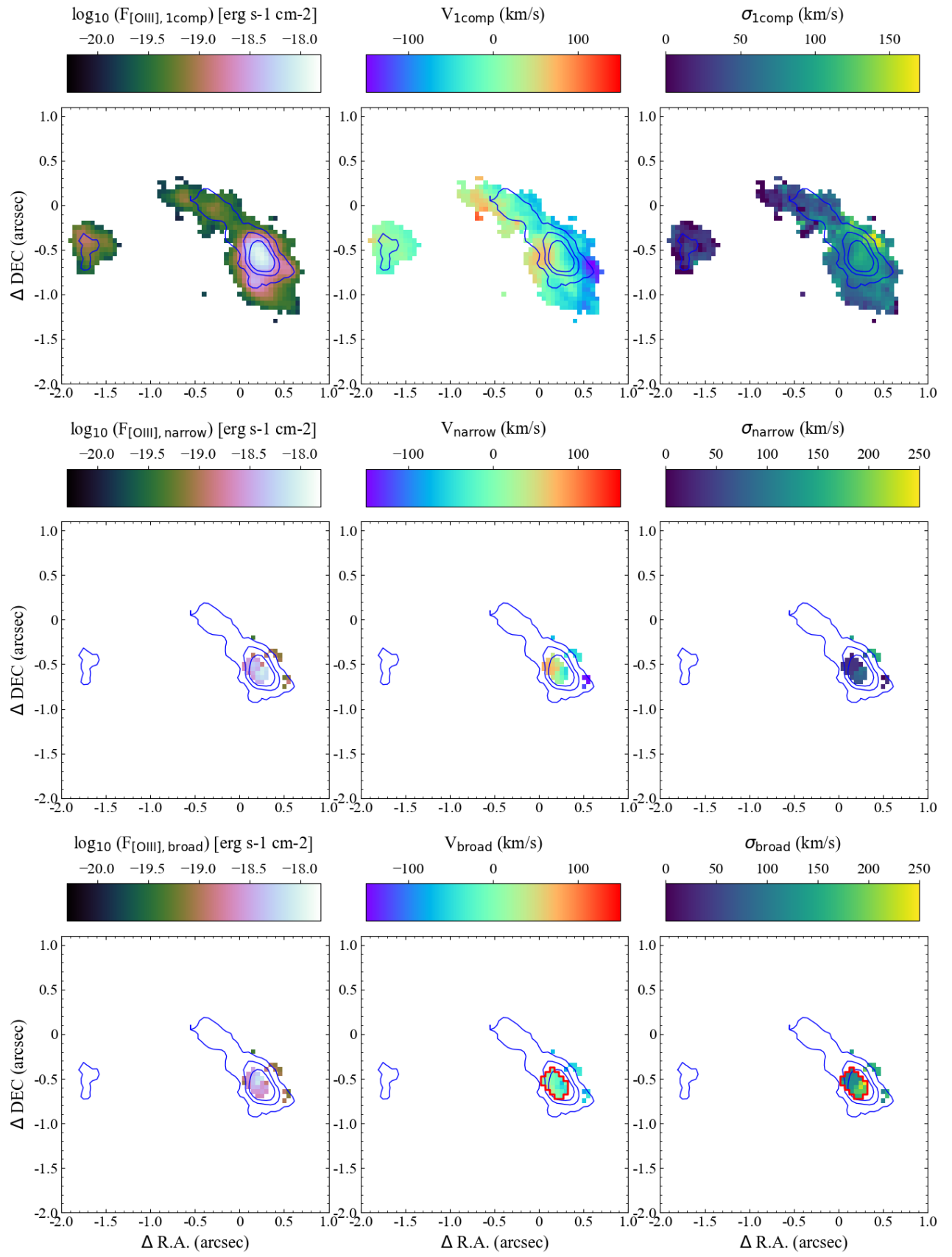


Fig. C.3: Same as Fig. C.1 for 4891.

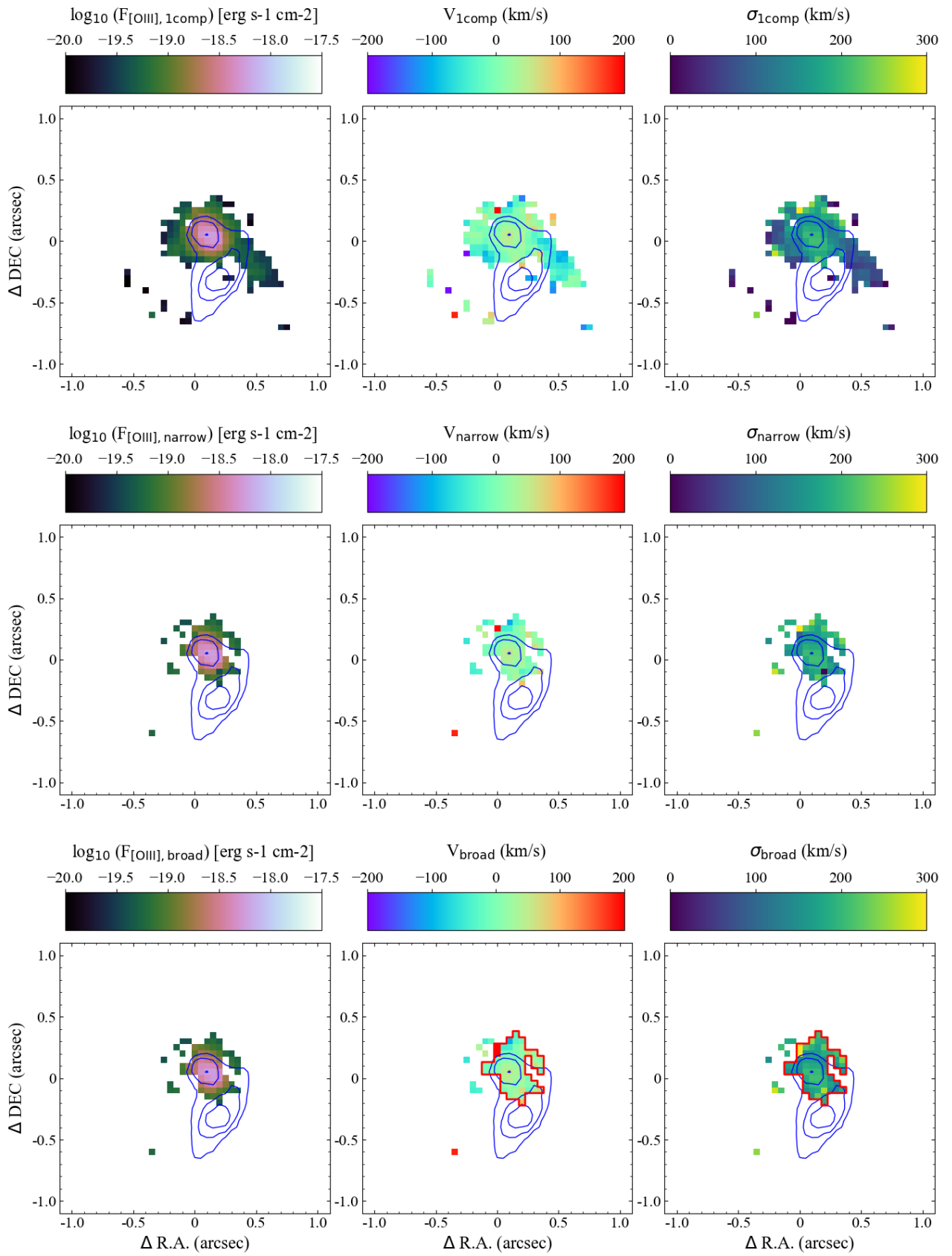


Fig. C.4: Same as Fig. C.1 for HFLS3\_g1.

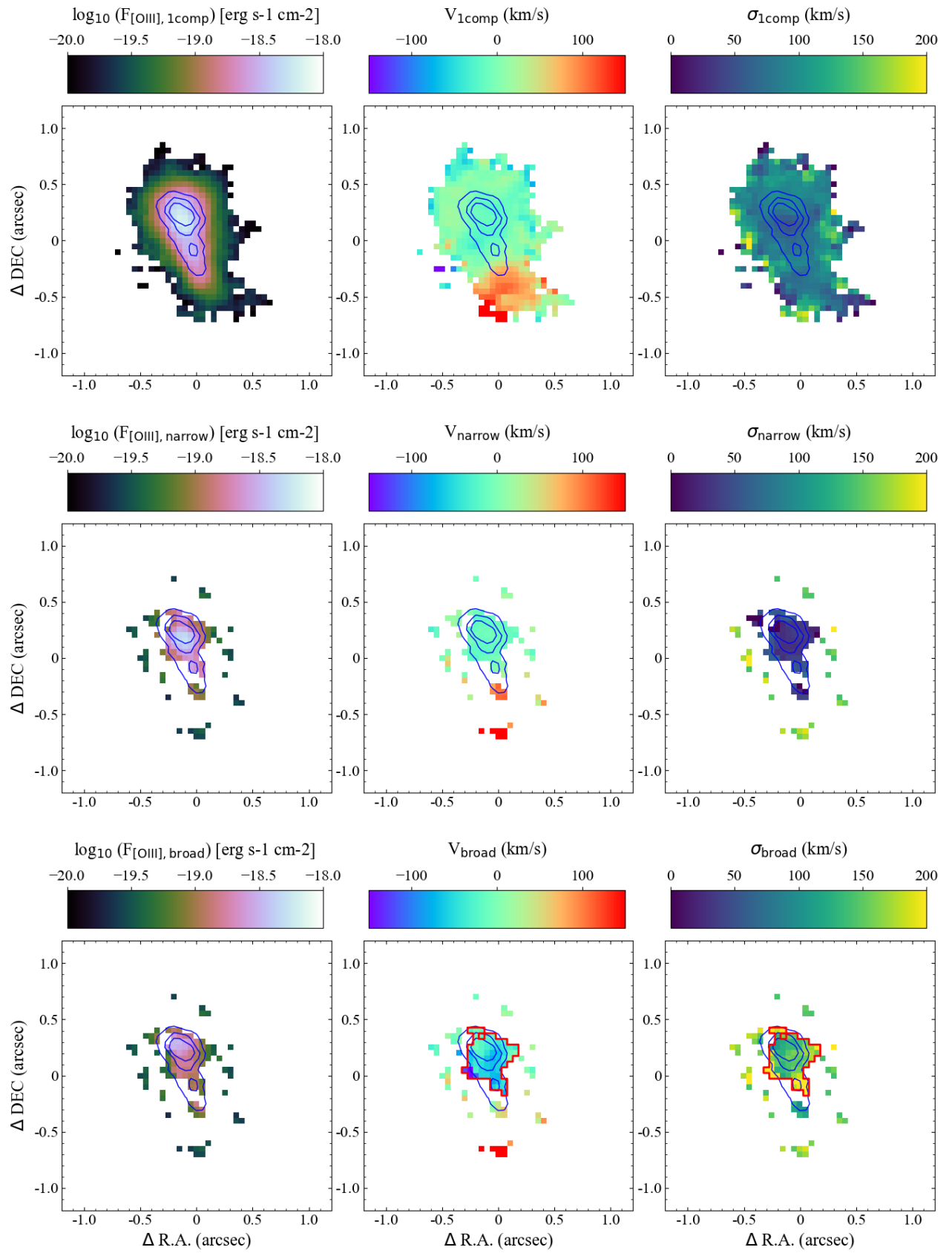


Fig. C.5: Same as Fig. C.1 for HZ4.

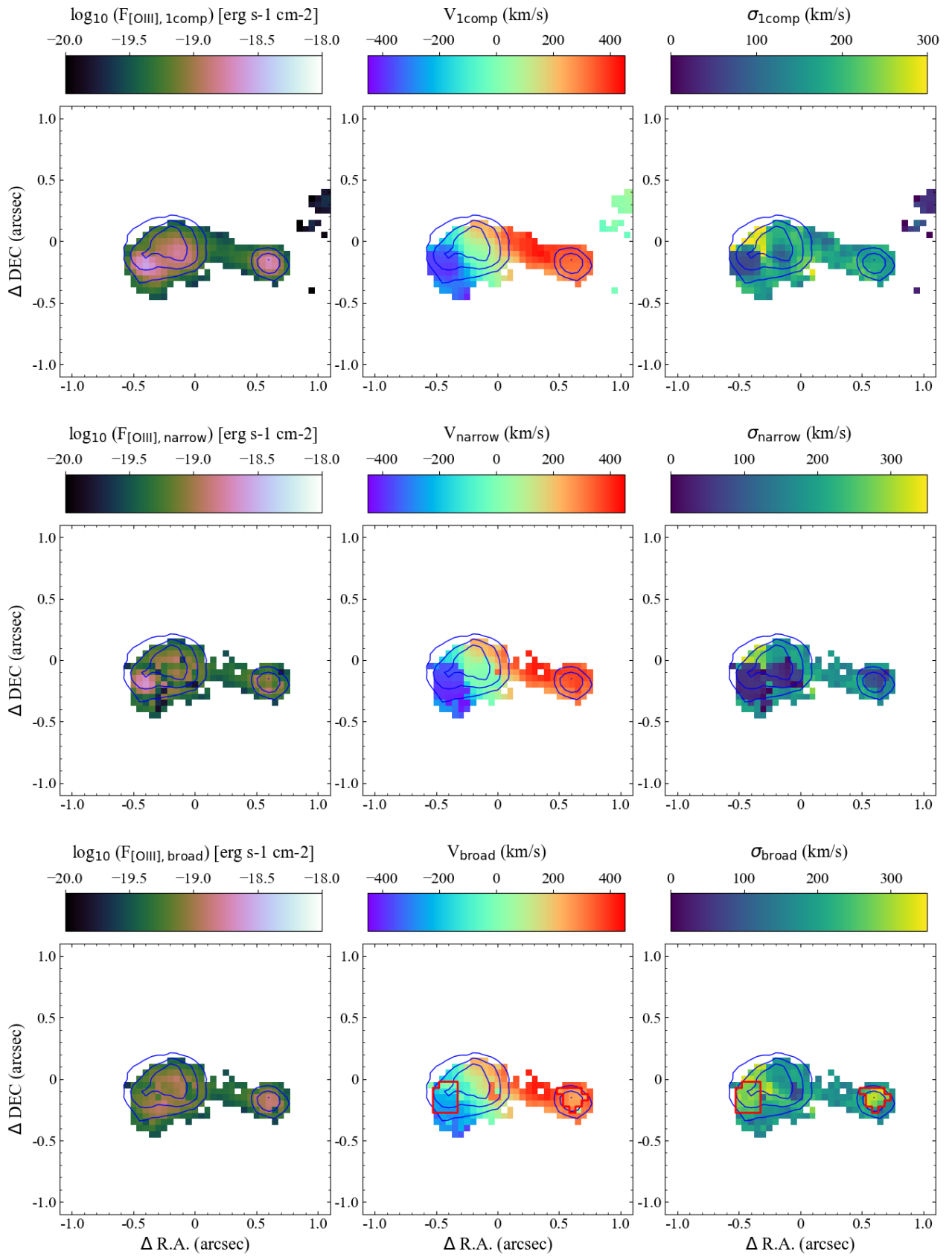


Fig. C.6: Same as Fig. C.1 for HZ10.

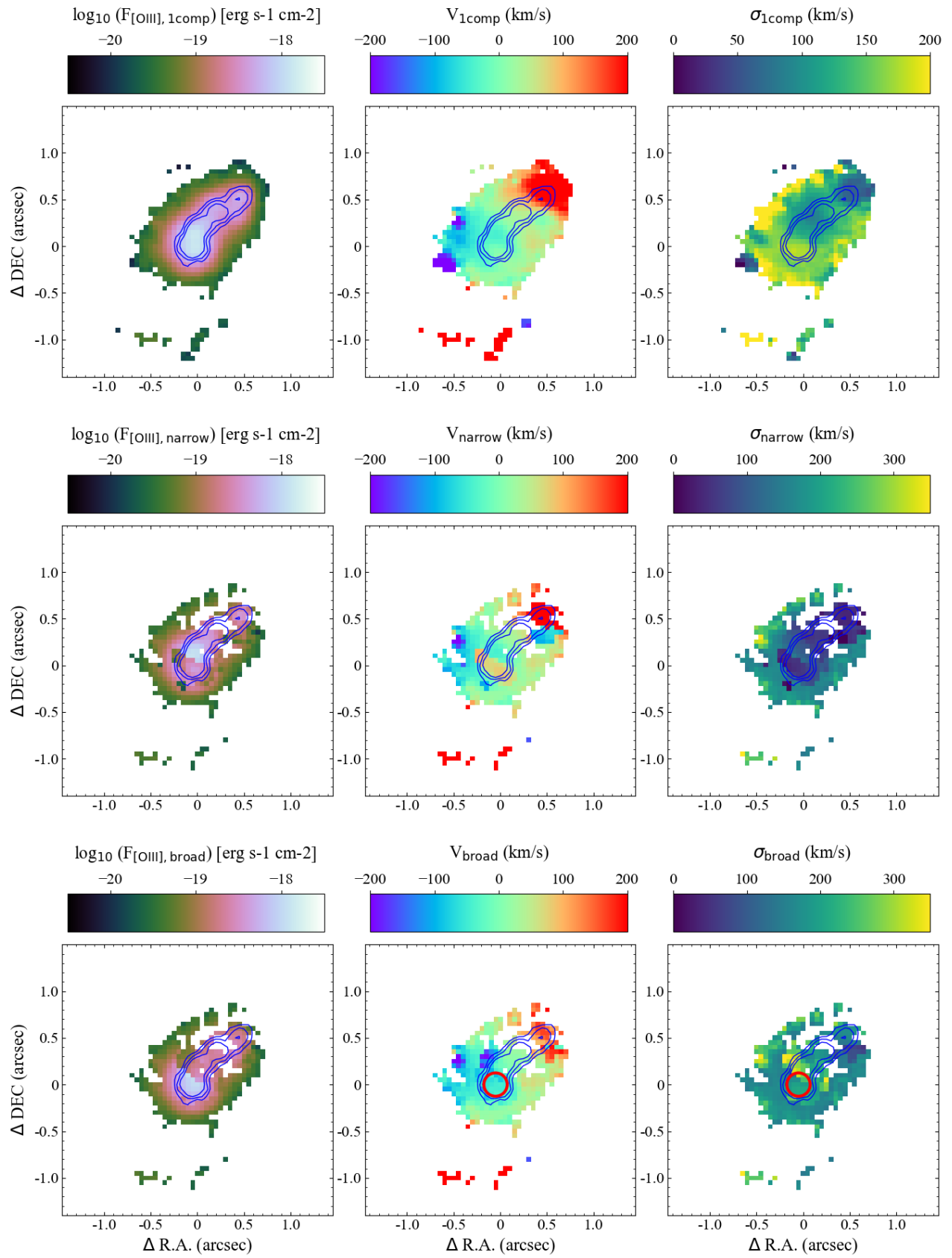


Fig. C.7: Same as Fig. C.1 for 12306.

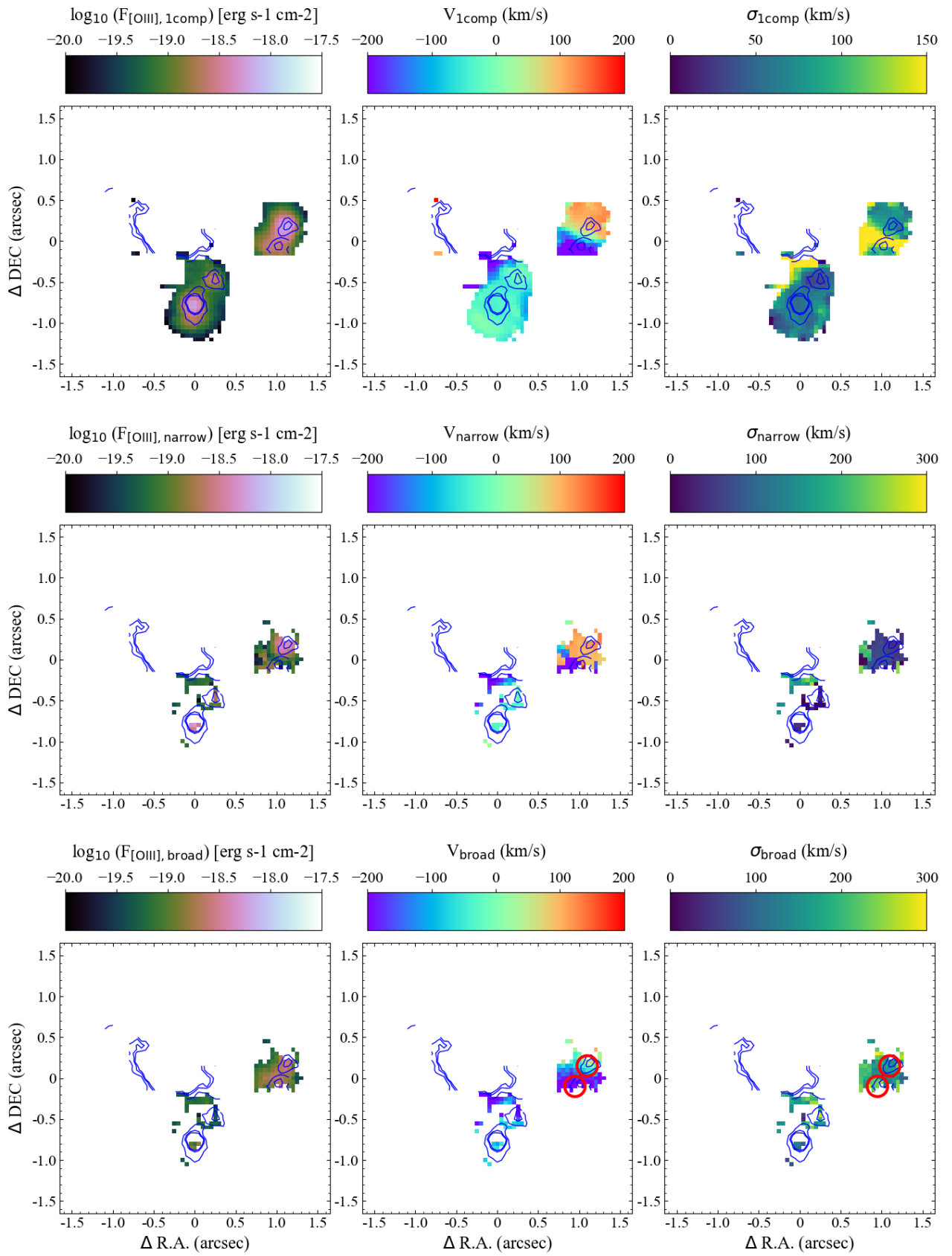


Fig. C.8: Same as Fig. C.1 for HFLS3\_w.

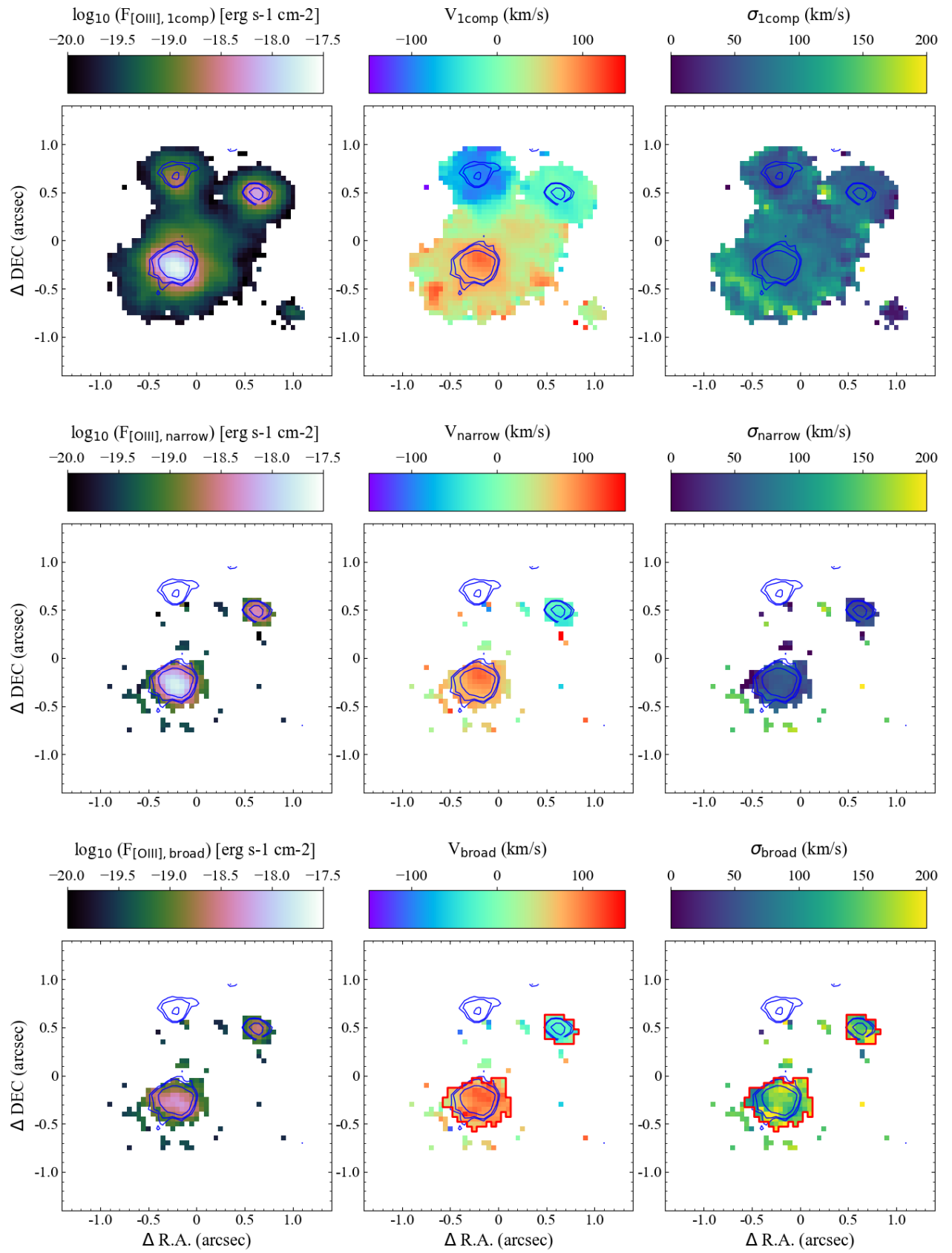


Fig. C.9: Same as Fig. C.1 for CR7.

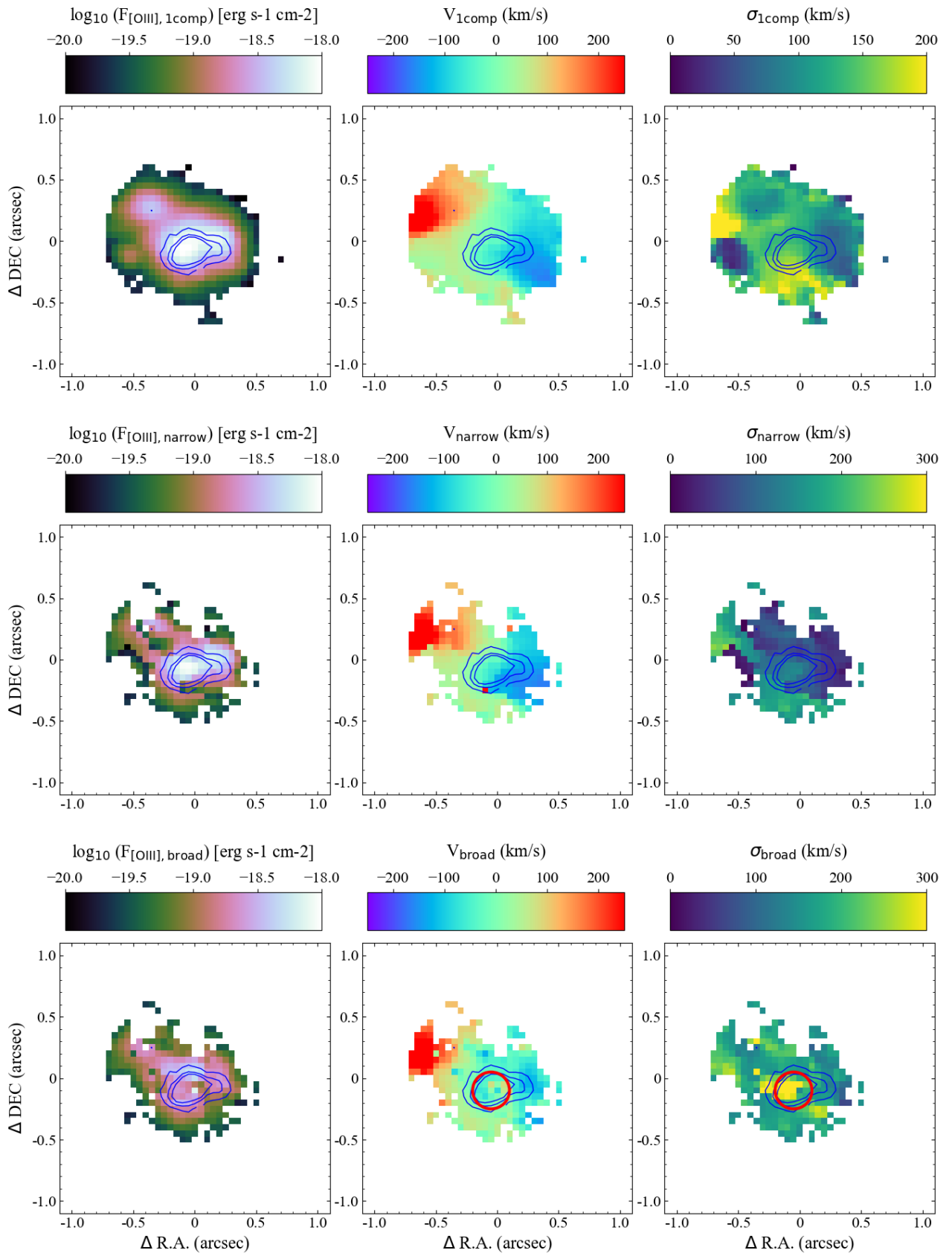


Fig. C.10: Same as Fig. C.1 for COS30.

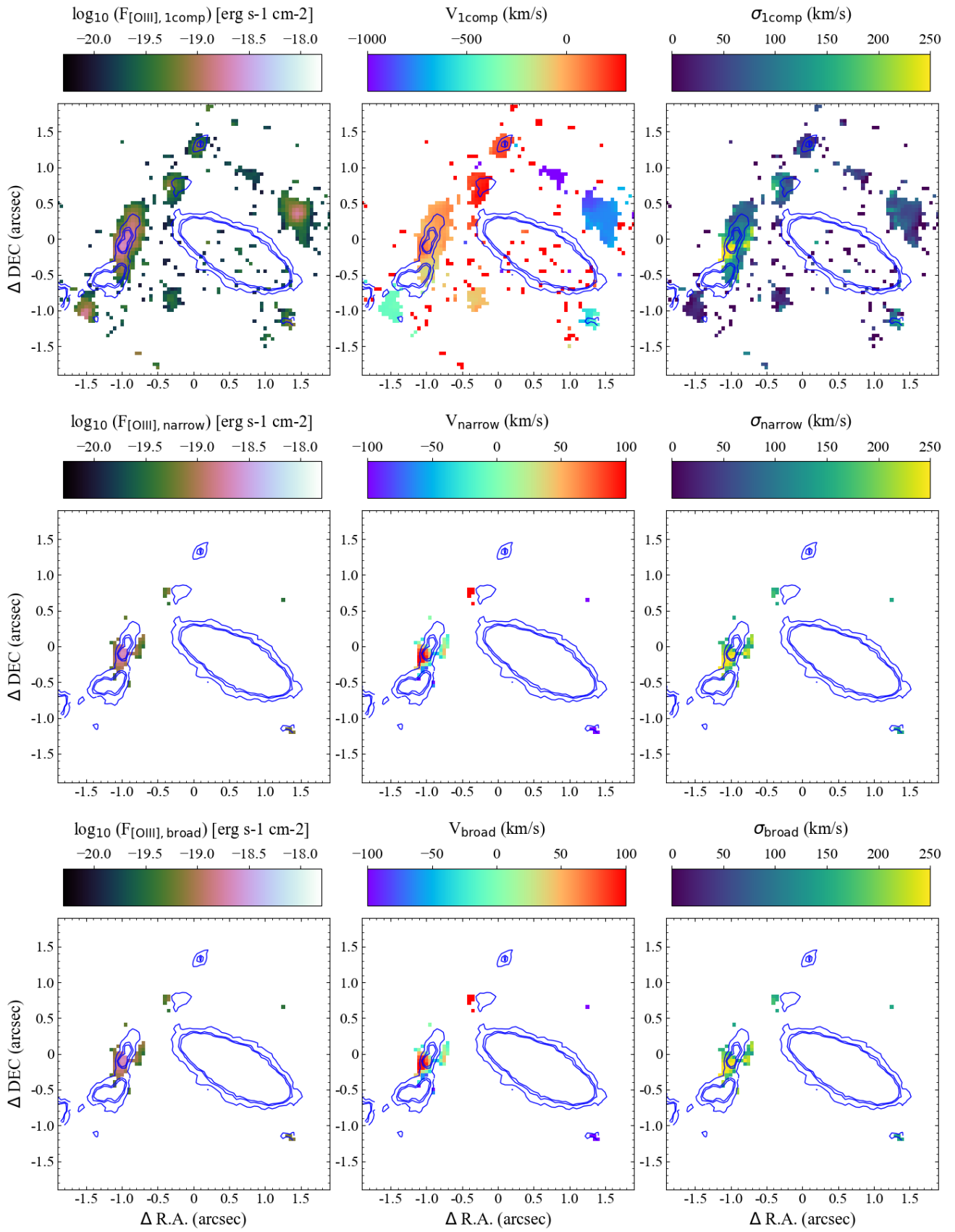


Fig. C.11: Same as Fig. C.1 for SPT0311, although in this galaxy we do not identify an outflow.

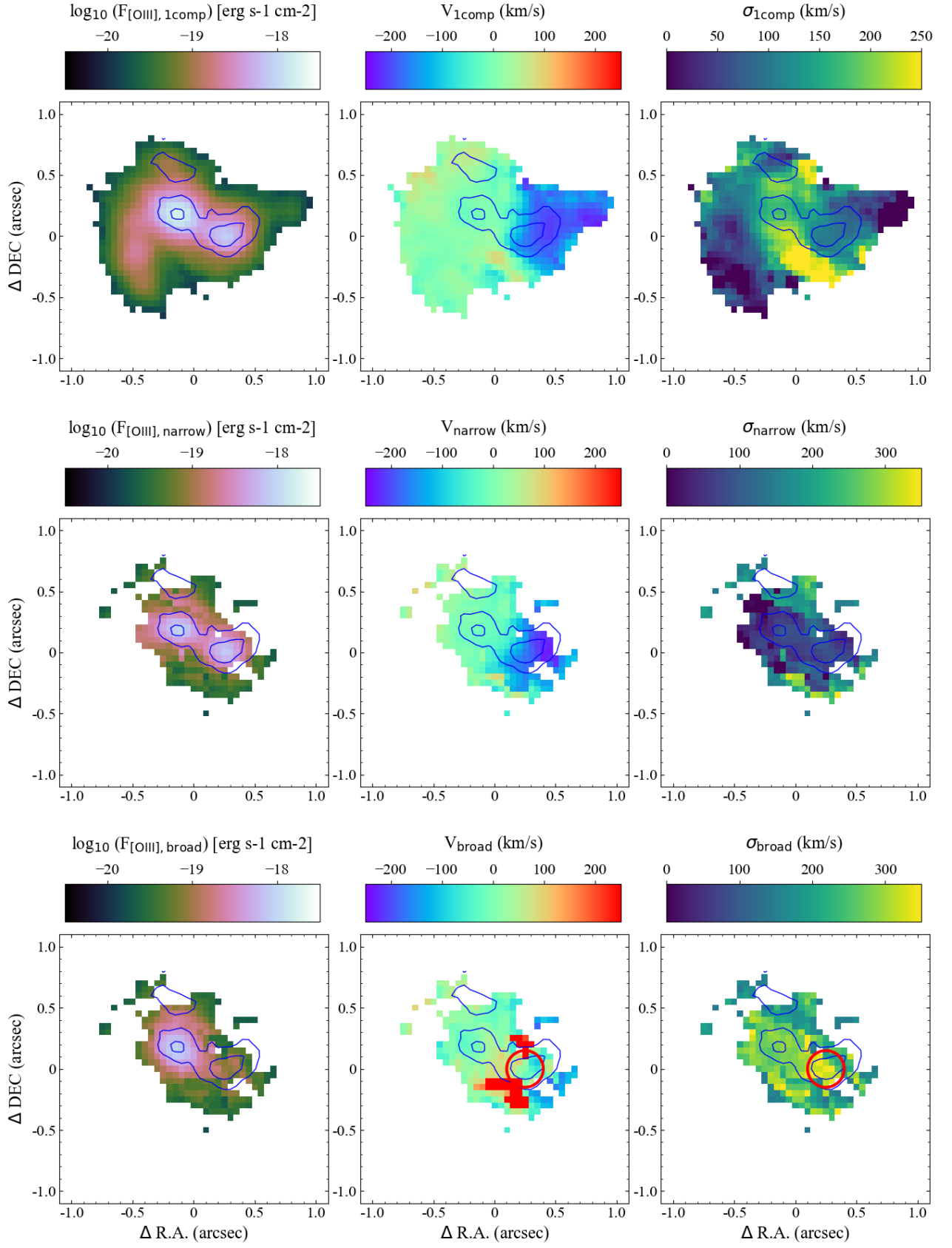


Fig. C.12: Same as Fig. C.1 for B14, although in this galaxy we do not identify an outflow.

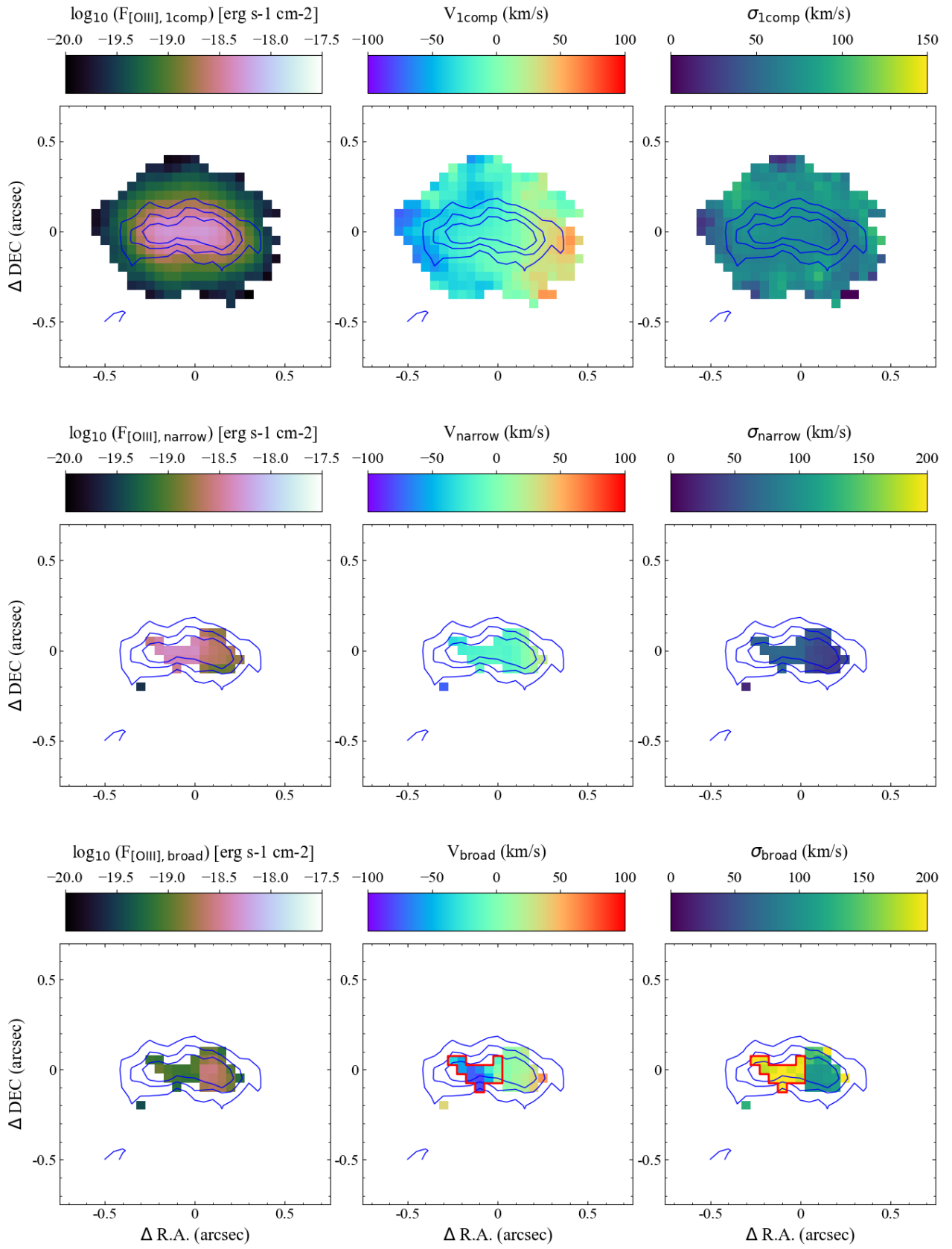


Fig. C.13: Same as Fig. C.1 for MACSJ0416-Y1.

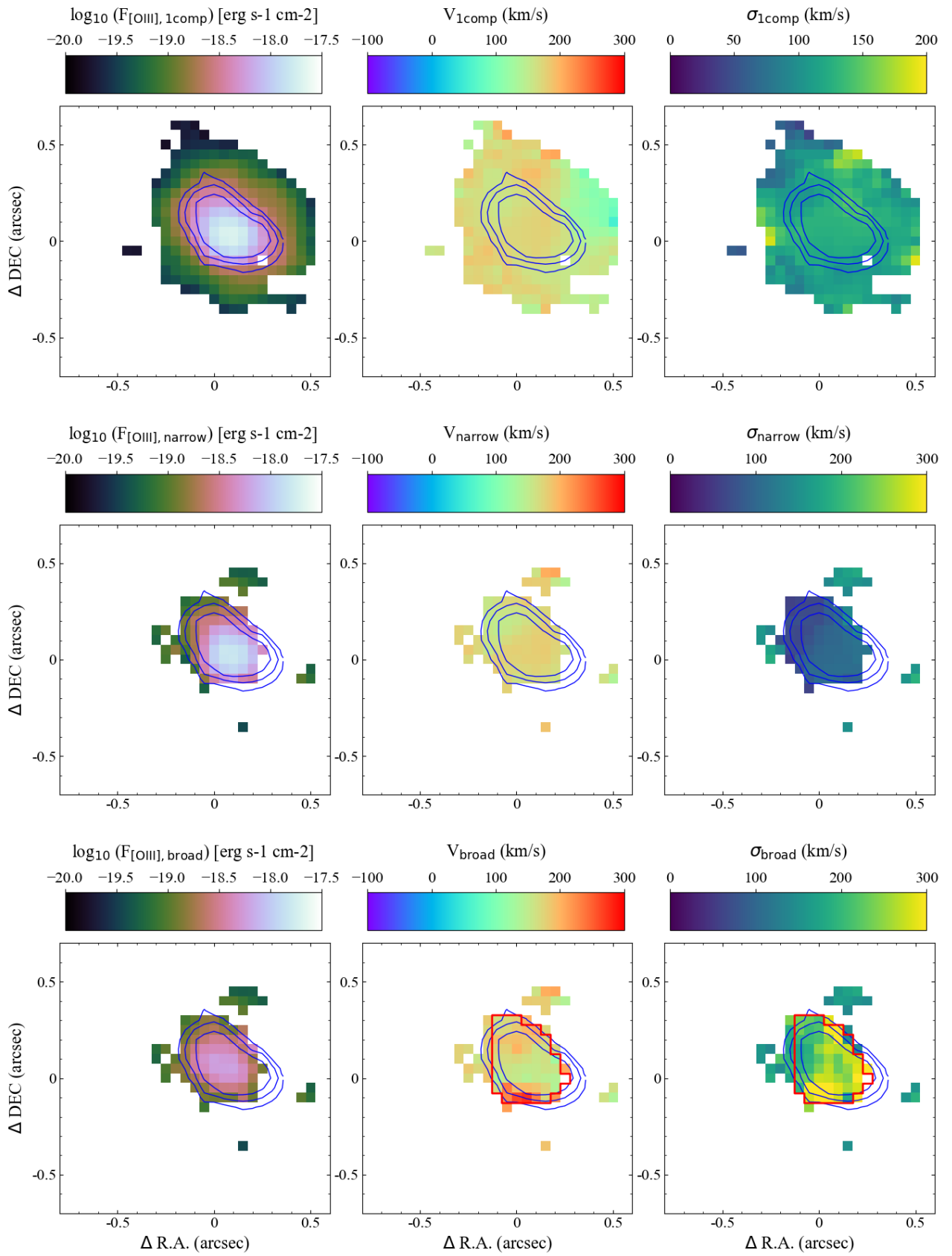


Fig. C.14: Same as Fig. C.1 for EGSY8P7.

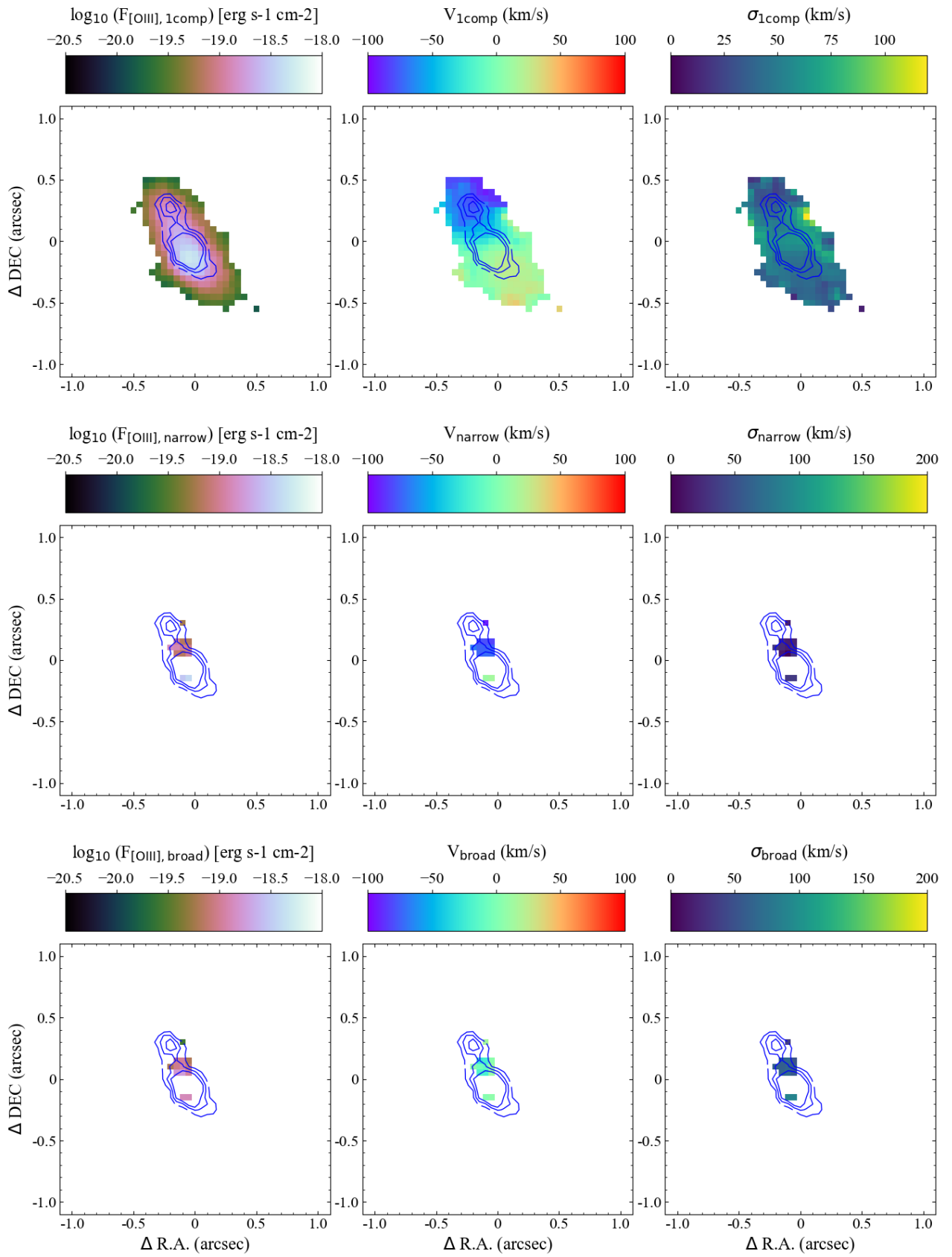


Fig. C.15: Same as Fig. C.1 for MACS1149-JD1.

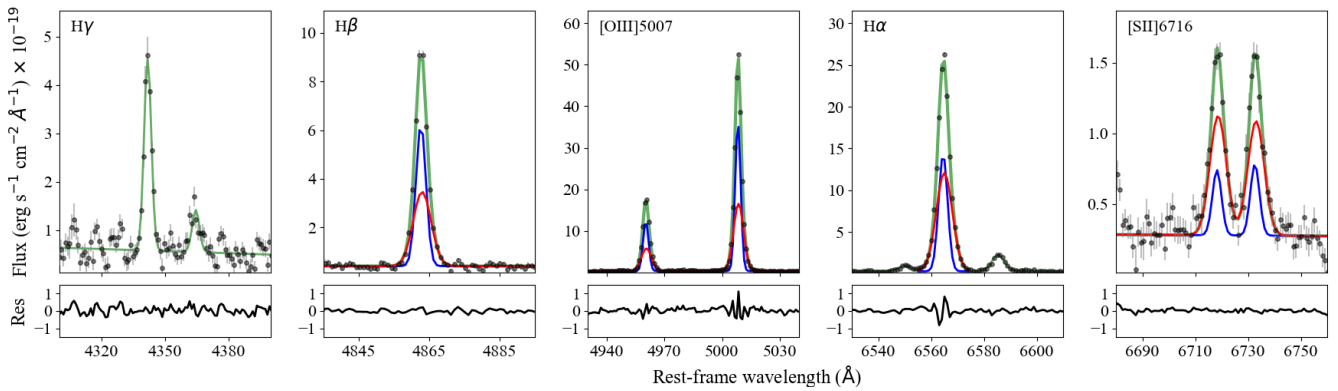


Fig. D.1: Spectral modeling of the main emission lines present in the integrated spectrum of the ionized outflow identified in 23170. Green lines correspond to the total best-fit. When the profile of an emission line is better modeled with two kinematic components (see Sec. 5) we also display the narrow and broad components as blue and red lines, respectively. Residuals shown in the bottom panels are obtained by subtracting the best-fit model to the data points.

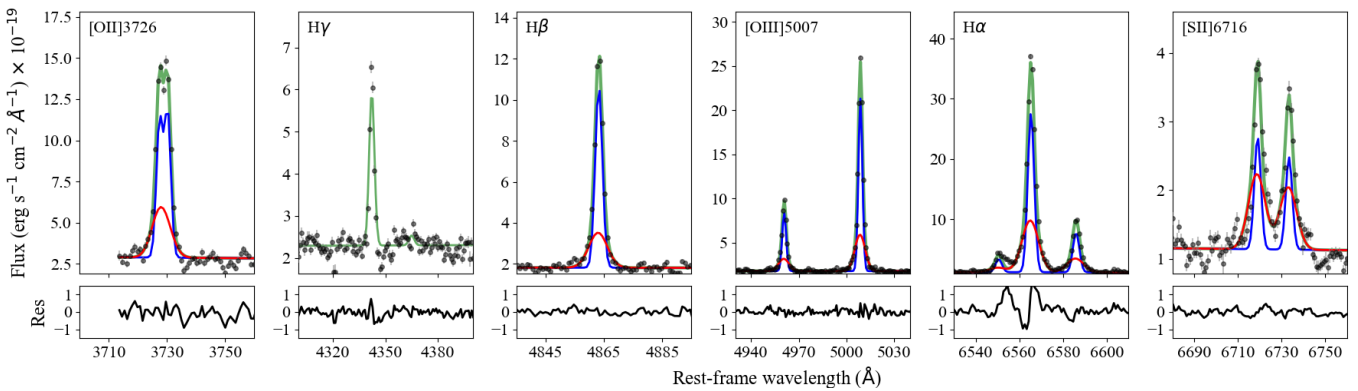


Fig. D.2: Spectral modeling of the main emission lines present in the integrated spectrum of the ionized outflow identified in 5001. A description of the panels is provided in Fig. D.1.

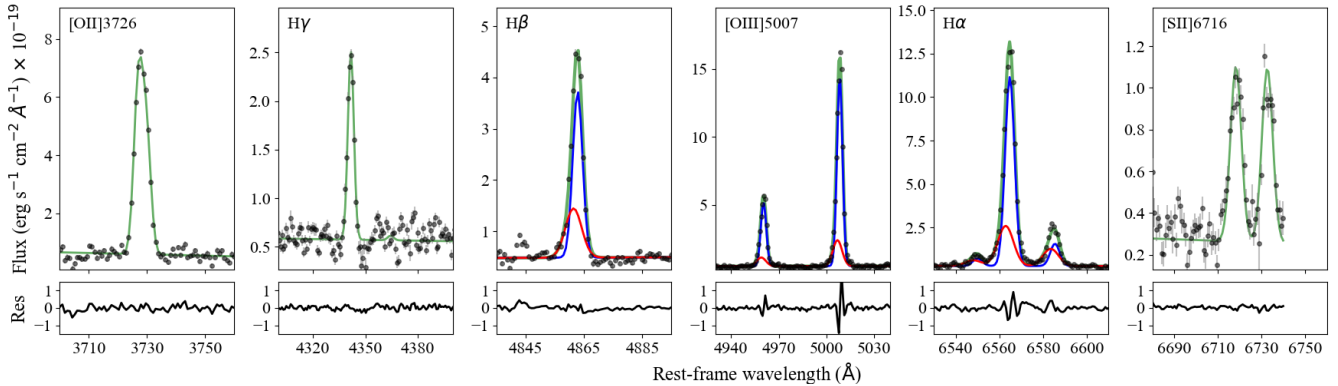


Fig. D.3: Spectral modeling of the main emission lines present in the integrated spectrum of the ionized outflow identified in 4891. A description of the panels is provided in Fig. D.1.

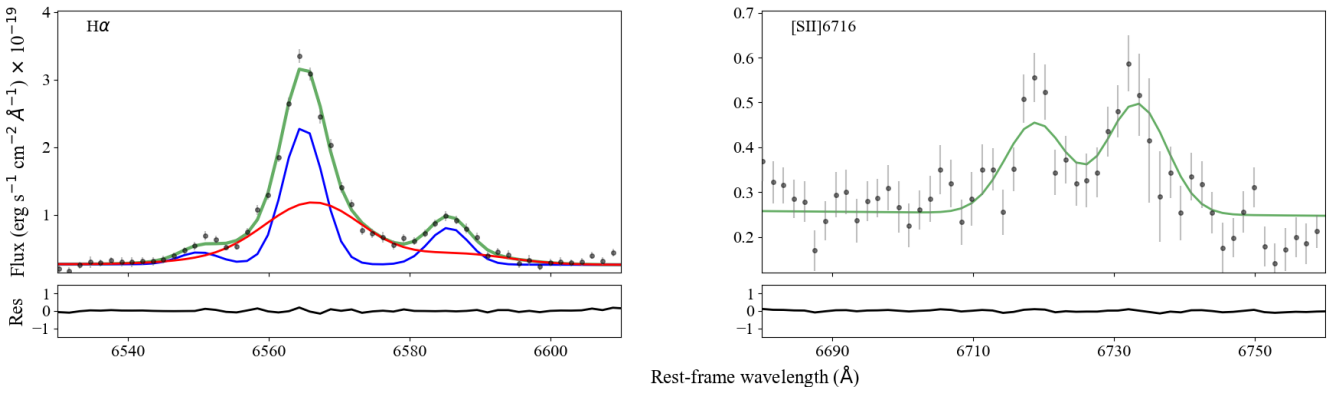


Fig. D.4: Spectral modeling of the main emission lines present in the integrated spectrum of the ionized outflow identified in HFLS3\_g1. A description of the panels is provided in Fig. D.1.

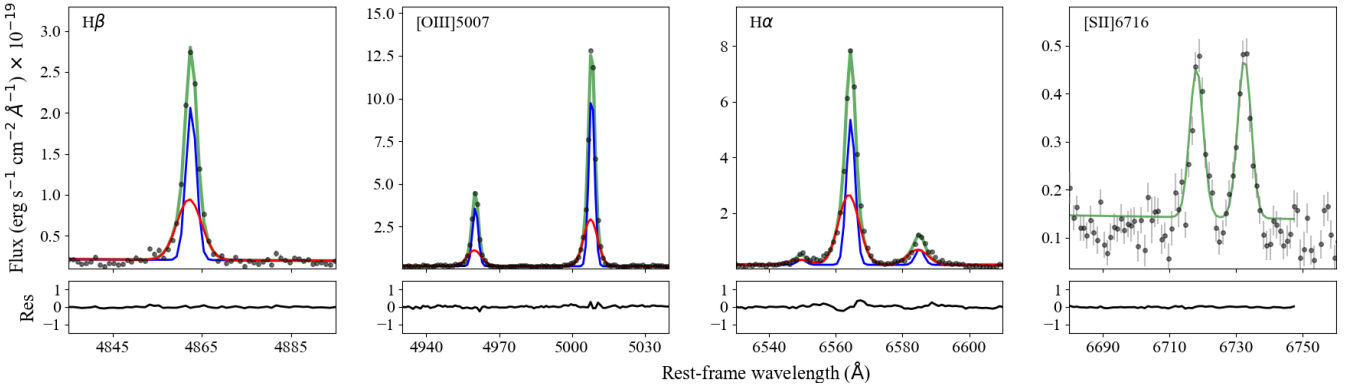


Fig. D.5: Spectral modeling of the main emission lines present in the integrated spectrum of the ionized outflow identified in HZ4. A description of the panels is provided in Fig. D.1.

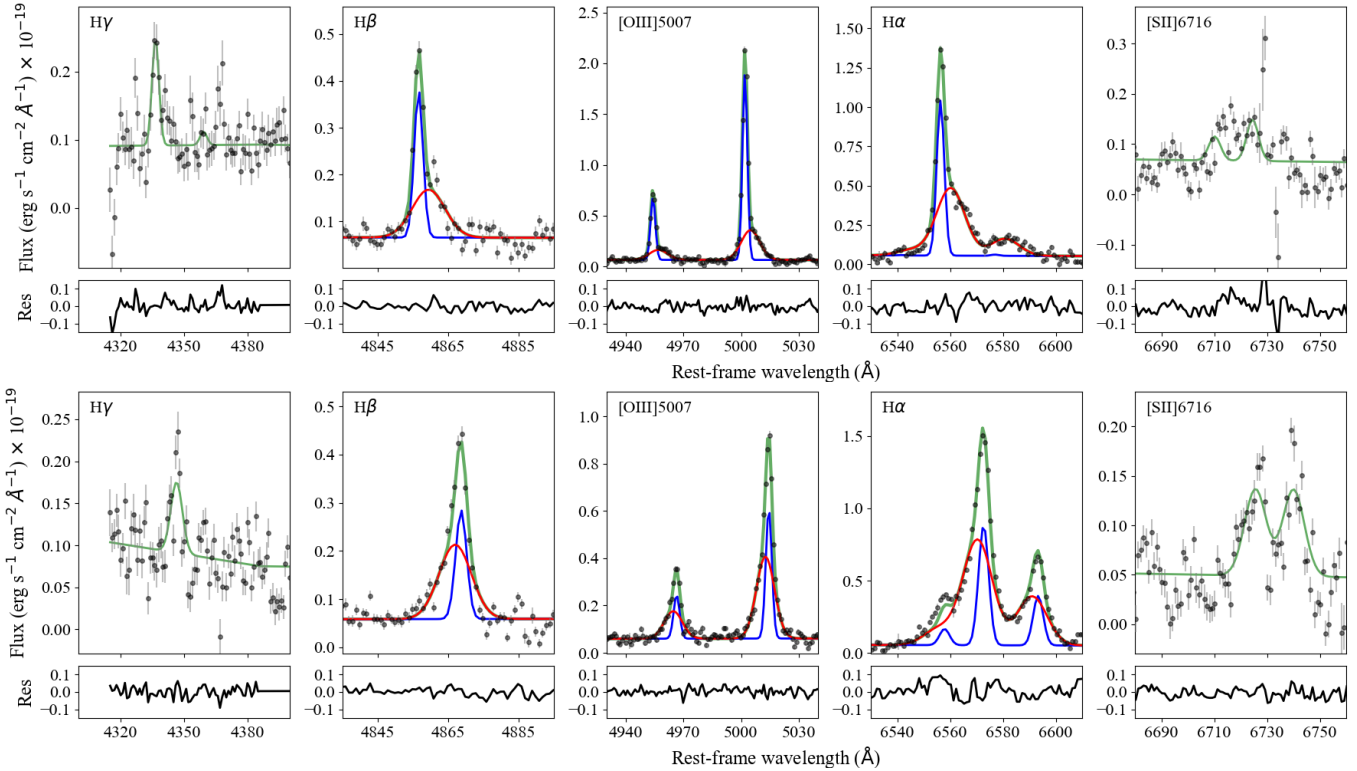


Fig. D.6: Spectral modeling of the main emission lines present in the integrated spectra of the ionized outflows identified in HZ10\_E (top) and HZ10\_W (bottom). A description of the panels is provided in Fig. D.1.

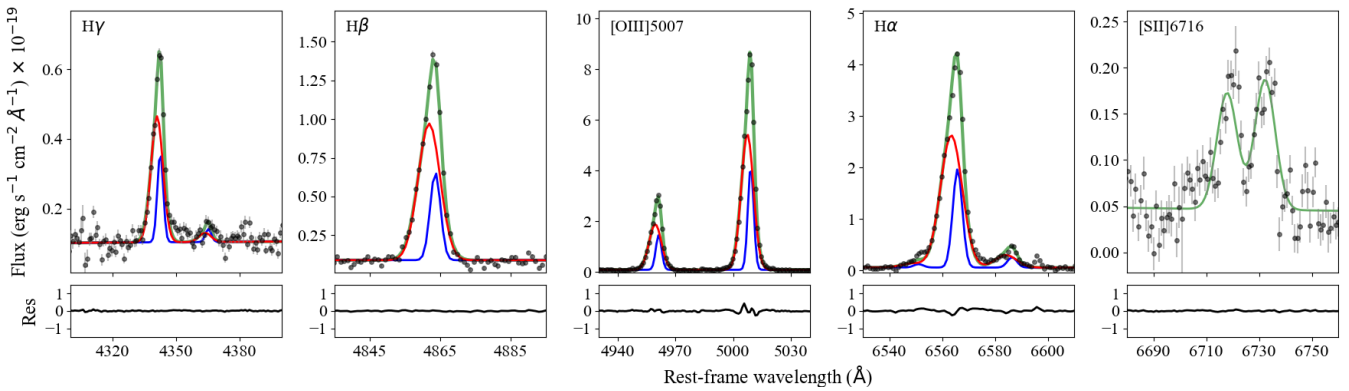


Fig. D.7: Spectral modeling of the main emission lines present in the integrated spectrum of the ionized outflow identified in the nuclear region of 12306. A description of the panels is provided in Fig. D.1.

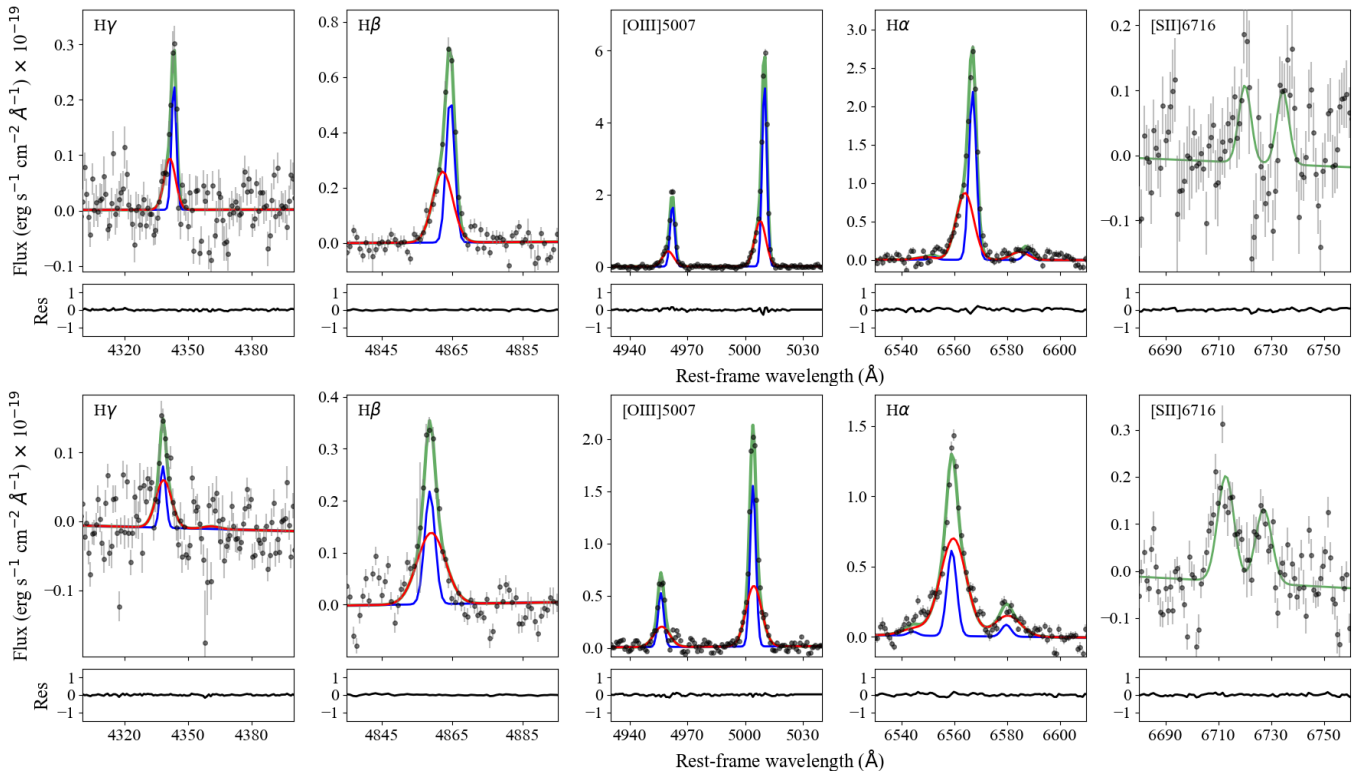


Fig. D.8: Spectral modeling of the main emission lines present in the integrated spectra of the ionized outflows identified in HFLS3\_w 1 (top) and (bottom). A description of the panels is provided in Fig. D.1.

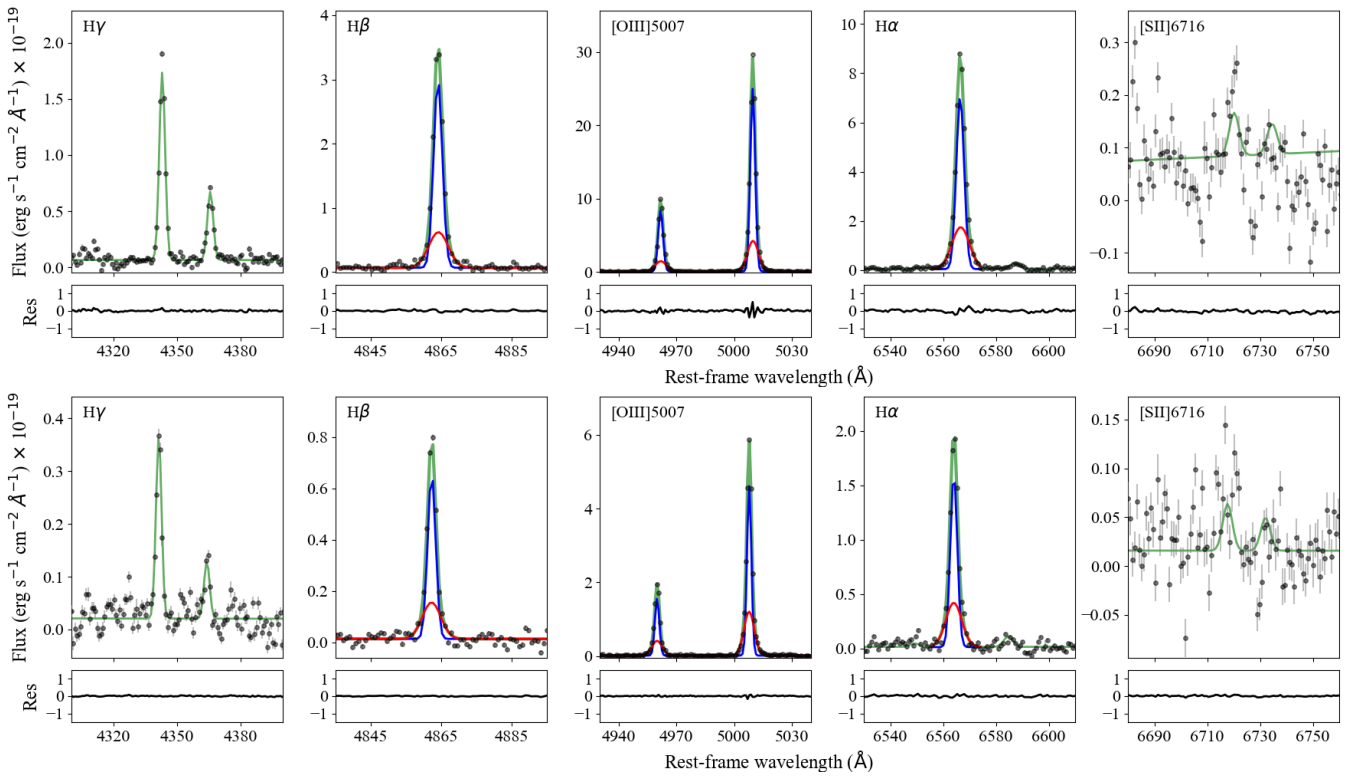


Fig. D.9: Spectral modeling of the main emission lines present in the integrated spectra of the ionized outflows identified in CR7\_a (top) and CR7\_b (bottom). A description of the panels is provided in Fig. D.1.

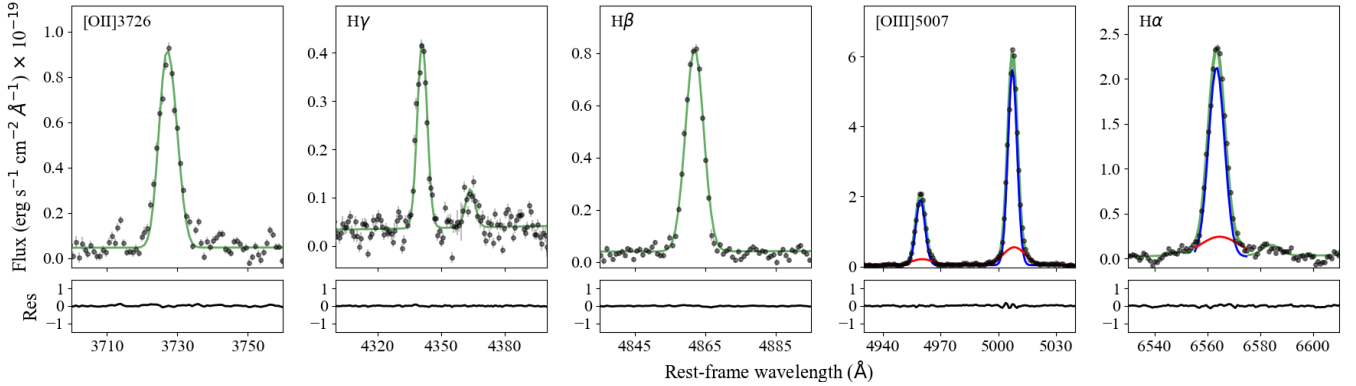


Fig. D.10: Spectral modeling of the main emission lines present in the integrated spectrum of the ionized outflow identified in the nuclear region of COS3018. A description of the panels is provided in Fig. D.1.

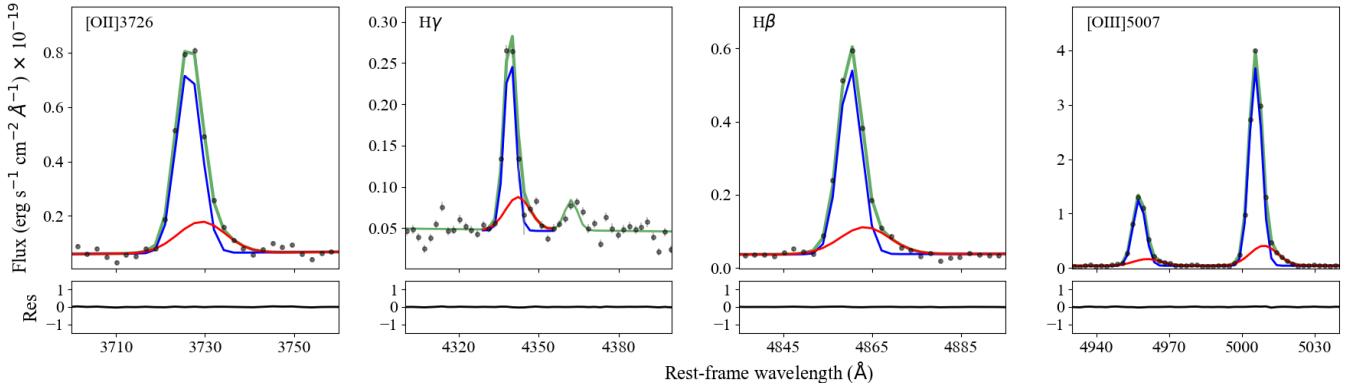


Fig. D.11: Spectral modeling of the main emission lines present in the integrated spectrum of the ionized outflow candidate identified in the nuclear region of B14. A description of the panels is provided in Fig. D.1.

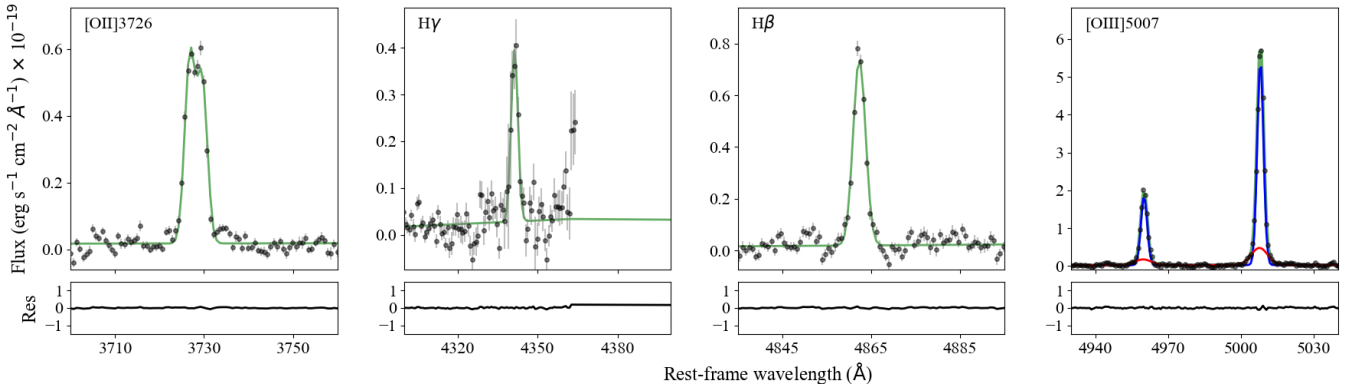


Fig. D.12: Spectral modeling of the main emission lines present in the integrated spectrum of the ionized outflow identified in MACSJ0416-Y1. A description of the panels is provided in Fig. D.1.

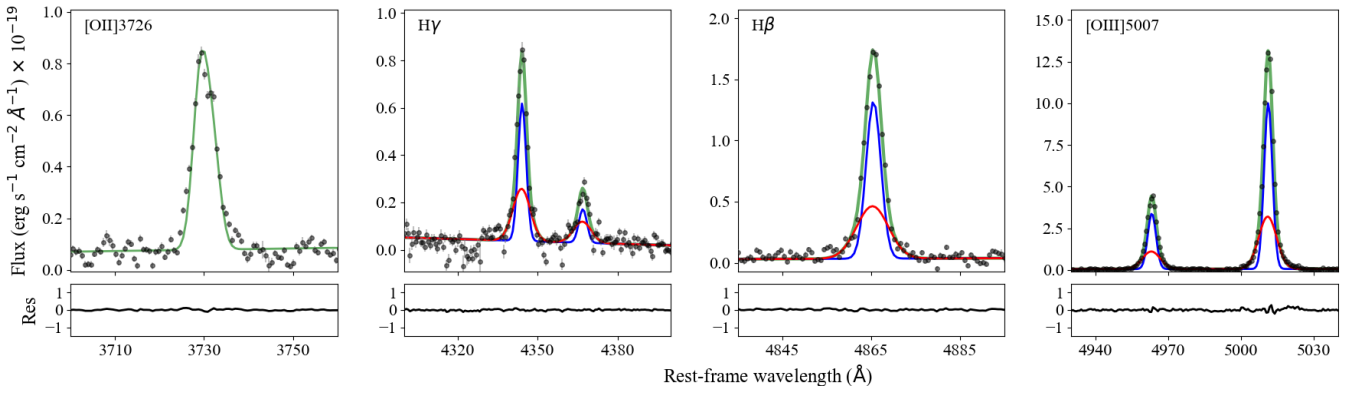


Fig. D.13: Spectral modeling of the main emission lines present in the integrated spectrum of the ionized outflow identified in EGSY8P7. A description of the panels is provided in Fig. D.1.